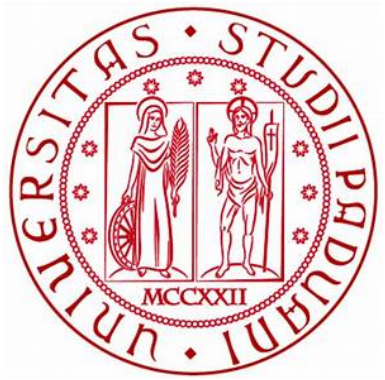

UNIVERSITÀ DEGLI STUDI DI PADOVA

Dipartimento di Fisica e Astronomia "Galileo Galilei"

Master Degree in Physics

Final Dissertation

The density limit in fusion plasmas: the role of edge instabilities

Thesis supervisor

Dr. Matteo Zuin

Thesis co-supervisor

Dr. Gianluca Spizzo

Thesis co-supervisor

Dr. Marco Veranda

Candidate

Nicholas Vivenzi

Academic Year 2018/2019

Abstract

This Thesis deals with the study of density limit in magnetically confined fusion plasmas. The density limit causes the termination of the plasma discharge when a threshold value for the electron density is overcome, the so-called Greenwald density (n_G), and thus represents an important operative limit for fusion devices.

The problem is studied following a multiple point of view approach involving the numerical solution of a single-fluid model for the plasma, the study of plasma transport theory and the analysis of data coming from the reversed-field pinch experiment RFX-mod in Padua, Italy.

Analysis of the results from numerical simulations of the reversed-field pinch configuration allows confirming the role of a dimensionless parameter of the model (the Hartmann number H, related to plasma resistivity and viscosity) in describing the transition observed in the dynamics of the plasma and in ruling the behaviour of edge-magnetic field.

Analysis of the plasma transport theory allows writing the Hartmann number in terms of plasma measurable quantities.

Analysis of a wide set of data coming from the RFX-mod experiment allows linking the trend in edge-magnetic field observed at the onset of the density limit to the (perpendicular) Hartmann number: this supports abandoning the phenomenological n_G parameter in favor of H. Furthermore, H describes with a good level of correlation the behaviour of the measured plasma density, temperature and current.

The work in this Thesis provides an important confirmation to the use of the single-fluid model in modeling reversed-field pinch plasmas and opens the way towards exploring the possibility that H could be the order parameter also in the tokamak density limit.

Contents

Ringraziamenti

Arrivato alla fine fine di questo percorso di studi desidero ringraziare le persone che mi hanno sostenuto in tutte le difficoltà fino al raggiungimento di questo importante obiettivo.

Prima di tutto, desidero ringraziare la mia famiglia per avermi dato sempre sostegno ed aiuto incondizionati, soprattutto nei momenti più difficili, permettendomi di fare liberamente le mie scelte e superare molti ostacoli, anche i più difficili.

Non avrei potuto concludere questa tesi senza l'aiuto ricevuto durante gli ultimi mesi di lavoro presso il Consorzio RFX, dove ho trovato un gruppo di persone fantastiche, molto preparate e sempre disponibili nei miei confronti. Sono molto felice di poter collaborare con loro anche nel prossimo futuro.

Ringrazio, in particolare, il mio relatore Matteo Zuin, per la disponibilità e la cordialità che mi ha dimostrato durante tutto questo percorso. Un grazie speciale va ai miei tutor Gianluca Spizzo e Marco Veranda per tutto ciò che mi hanno insegnato, corretto e per avermi seguito con pazienza in questo lavoro, rispondendo sempre a tutte le mie domande, aiutandomi costantemente a migliorare.

Inoltre, vorrei esprimere gratitudine a Susanna Cappello, responsabile del gruppo di teoria del Consorzio RFX per i preziosi consigli, grazie ai quali ho potuto sviluppare al meglio questo lavoro, e ai ricercatori David Terranova, Paolo Scarin e Matteo Agostini per il loro valido aiuto nell'analisi e discussione dei risultati.

E, infine, un pensiero a mio zio Giacomo, che sono sicuro avrebbe voluto condividere con me questo momento di gioia, ma purtroppo è mancato pochi mesi fa e ciò mi rattrista particolarmente.

Padova,
9 Settembre 2019

Nicholas Vivenzi

Introduction

This thesis summarizes the activity of about six months I spent in Consorzio RFX, inside the Padova CNR research area. The research activity of the Consorzio RFX is aimed at the study of nuclear fusion as a future energy source able to sustain the growing energy demand, CO_2 free and safer than the actual exploitation of nuclear energy (based on nuclear fission).
Considered the importance of achieving such a goal, this field of research is coordinated at an international level. In Europe, a road map based on plasma magnetic confinement is expected to bring the exploitation of nuclear fusion on a commercial level within the end of this century (shown in Figure 1). The major international project on which fusion scientists are working in these years is ITER (International Thermonuclear Experimental Reactor) that is under construction in Cadarache, France. This experiment is the result of a long series of studies that historically began just after World War II, at the "Second United Nations International Conference on the Peaceful uses of Atomic Energy", better known as the "Atoms for Peace" conference (1-13 September 1958). ITER represents the last step before the construction of a real demonstrative reactor (DEMO), foreseen to start its activity around 2050.

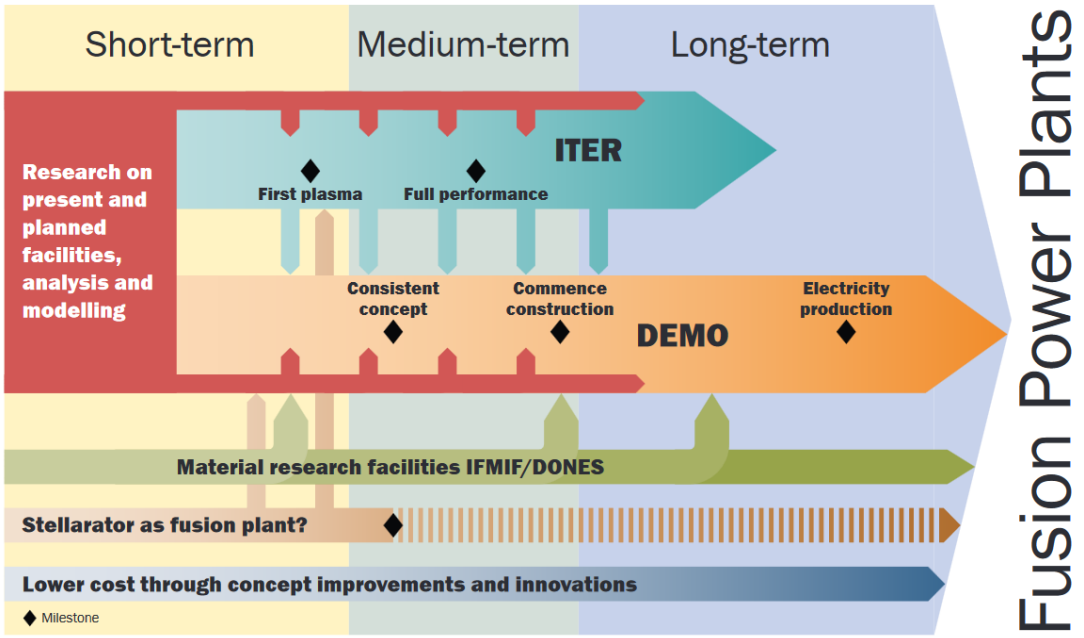

Figure 1: European research program in fusion science, aimed at the commercial use of fusion.

Consorzio RFX is one of the laboratories that collaborate in this ambitious project, and it hosts two experiments: NBTF (Neutral Beam Test Facility) to study the ITER neutral beam injector and RFX-mod (Reversed Field eXperiment) that is an independent fusion experiment that studies the RFP (reversed field pinch) magnetic configuration.
One of the main difficulties that has to be overcome, is related to plasma instability. In fact, the conditions at which ITER is expected to work, require to develop control techniques (presently under

study) in order to guarantee a proper duty cycle of the device. The plasma instabilities have different properties and consequences depending on the type of magnetic configuration considered. The physical phenomena that determine them are not yet entirely understood and explained.
In this work, one of these instability phenomena (common to the three main magnetic configurations) is studied: the density limit. This limit causes the termination of the plasma discharge, when a threshold value for the electron density is overcome. So far, many efforts have been spent phenomenologically to predict this threshold value, still lacking a complete physical explanation, based on 'first principles'. The goal of this thesis is the development of a new approach based both on theoretical models, numerical simulations and experimental data analysis, aimed at a better understanding of the density limit, in the case of the RFP configuration. Particular attention has been paid to the role of edge radial magnetic field instabilities, observed as precursors of such a limit.
More precisely, the nonlinear MHD visco-resistive model is used in simulating RFP plasmas and from it, the most important parameter that arises is the dimensionless Hartmann number (depending on resistivity and viscosity), able to describe quite well the behaviour of magnetic energy and edge magnetic field. Thanks to the theoretical work of Braginskii transport coefficients and Hartmann number can be expressed (and evaluated) in terms of plasma parameters. The expressions obtained allow the description of the density limit and the main plasma parameters in terms of the Hartmann number, on the basis of RFX-mod experimental measurements on a large database of discharges. Using the latter, also the role of edge magnetic field instabilities is estimated, followed by a final comparison with numerical simulations.

The matter introduced in this thesis is organized into five chapters.
Chapter 1 introduces nuclear fusion reactions and the different plasma confining methods that are used to gain energy from it. Concentrating on magnetic confinement, the favorable conditions for a future reactor to work are found taking into account the need of a positive gain in energy and the presence of instabilities that limit the operational space. The focus, in this last part of the chapter, is particularly addressed to the case of the density limit, that is the starting point of all the thesis work.
Chapter 2 is a theoretical chapter devoted to the description of the theoretical MHD models that are used in the following chapters. The first topic is the derivation of the Braginskii equations (starting from the kinetic model), whose closure is found in the context of Chapmann-Enskog and Balescu procedure. The latter, consisting in an equilibrium perturbation theory, allows the introduction of transport in plasmas, that is modelled with the introduction of transport coefficients, expressed as function of plasma parameters.
After that, the single fluid visco-resistive model is presented, with the hypotheses needed in order to develop it. Then, dimensionless fluid numbers are derived. The main one, which emerges after a proper variable transformation, is the Hartmann number. To conclude, the dimensionless numbers, relevant in the adopted fluid model, are finally rewritten as function of the main plasma physical quantities.
In **chapter 3** the reversed field-pinch configuration is described in its features, following the historical development to which the conception of this configuration undergoes, from the initial studies of the '70s by J.B. Taylor, up to modern numerical simulations. The RFX-mod device, the largest to work in RFP configuration, is introduced at the end of the chapter with its main experimental features.
The numerical results obtained during the thesis work are exposed in **chapter 4**, after a brief presentation of the SpeCyl 3D non-linear MHD code together with the main results obtained in previous works by RFX group. The simulation database used is described and all the physical quantities observed are listed. The last sections present the results of the analysis developed for the study of the density limit issue, i.e. magnetic energy and edge radial magnetic field, which are shown to mainly depend on the Hartmann number.
Chapter 5 is the one devoted to the experimental data analysis. After introducing the previous works useful to study the density limit, the databases considered during the analysis are presented as for the procedure adopted to estimate the Hartmann number, from RFX-mod data. This result is exploited in the next section that introduces scaling laws based on the use of the Hartmann number to describe the density limit, but also other important plasma parameters. In this chapter also the mode analysis

is developed, highlighting the role of the $m = 0$ modes as precursors of the density limit. As final section, a comparison between numerical simulations and experimental data is presented in the case of the edge magnetic field analysis.

Chapter 1

Nuclear fusion as an energy source

In this chapter, the main features of nuclear fusion reactions used to hopefully provide a future energy source are exposed. At first, nuclear reactions useful for energy purposes will be introduced. Secondly, concentrating on fusion, a presentation of the most important plasma confining methods will follow and then a description of the operational condition at which a future reactor is expected to work. In particular, attention will be paid to the power balance of the fusion reactor (to determine the conditions in which a net positive gain in energy is present) and to the operational limits introduced in order to avoid plasma instabilities.
Among these phenomena, a first look to the case of the density limit is taken, from a phenomenological point of view.

1.1 Nuclear fission and fusion reactions

The atomic nucleus is composed by protons and neutrons hold together by the nuclear force in a very small region of space, of the order of $1 - 10$ fm (depending on the nucleus considered). This quantum binding state is characterized by a mass lower than the sum of the masses of its smaller constituents: the difference in mass Δm is directly related to the binding energy thanks to the famous Einstein formula $E = \Delta m c^2$.
For a nucleus with mass M atomic number Z and mass number A, the binding energy per nucleon B is given by the following formula (in natural units):

$$M(A, Z) = Z m_p + (A - Z)\, m_n - AB(A, Z). \tag{1.1}$$

Each nucleus is characterized by its own binding energy: the behaviour of the latter (deduced from the experimental measures of the masses) with respect to the mass number can be estimated in the context of the liquid drop model for nuclei and it is shown in figure (1.1).

In a nuclear reaction, a certain amount of energy can be released (as products kinetic energy) when the mass of the products is lower than the mass of the reactants, that corresponds to the case in which the products have a higher binding energy than the reactants.
Since the binding energy trend shows a maximum correspondent to $A = 56$ (iron peak), two very different types of reactions are available to get energy: fission and fusion.
The reactions of nuclear fission consist in the subdivision of a heavy nucleus into two or more lighter nuclei and fragments. Such a reaction can be spontaneous or induced by an external projectile (like proton, neutron and γ photon), as in the following reaction (from [22]):

$$^{235}_{92}\mathrm{U} + {}^{1}_{0}\mathrm{n} \longrightarrow {}^{140}_{58}\mathrm{Ce} + {}^{94}_{40}\mathrm{Zr} + 2\,{}^{1}_{0}\mathrm{n} + 6\,\mathrm{e}^{-} + 206\,\mathrm{MeV}. \tag{1.2}$$

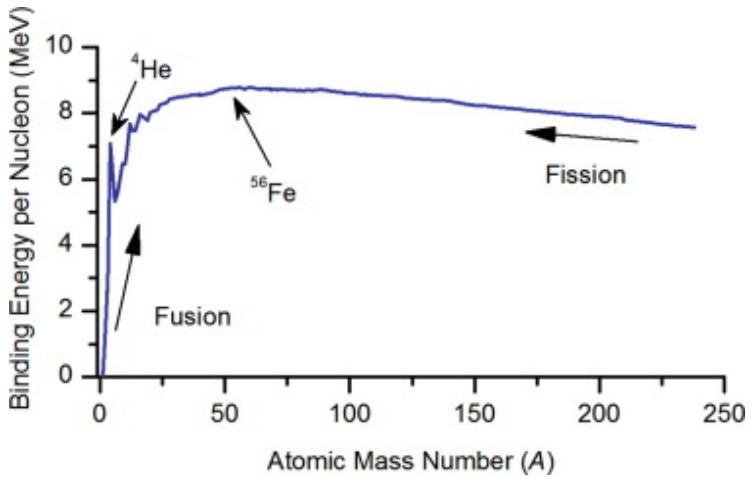

Figure 1.1: Trend of the binding energy per nucleon as function of the atomic mass number.

Nuclear fission has been regularly exploited as a controlled energy source in nuclear power plants since several decades, during which it has shown the potential to develop enormous amounts of energy. However, there are also disadvantages in the exploitation of nuclear fission: the production of long-lasting radioactive waste which requires special storage for a practically infinite time and the awful accidents that can occur when the chain reaction control fails (Černobyl' 1986) or the cooling system does not work properly (Fukushima 2011).
Nuclear fusion is the opposite process: two light nuclei merge together and give rise to a heavier nucleus. It is the type of reaction powering stars and sustaining their structure against the gravitational force that, otherwise, would cause them to collapse. Nuclear fusion is also responsible for the generation of the chemical elements with $Z \leq 26$.
The exploitation of nuclear fusion turned out to be much more difficult than in the case of fission and, despite the efforts made, it does not exist yet a prototype reactor similar to the "Fermi pile" able to produce electric power from fusion for commercial purposes: this is mainly due to the fact that nuclei are positively charged and their fusion requires the overcoming of the Coulomb potential barrier generated by the nuclei themselves. To build a machine able to exploit controlled nuclear fusion, the reactions mostly taken into account are the following:

$$^2\mathrm{D} + {}^2\mathrm{D} \longrightarrow {}^3\mathrm{T}(1.01\,\mathrm{MeV}) + \mathrm{p}(3.02\,\mathrm{MeV}) \tag{1.3}$$

$$^2\mathrm{D} + {}^2\mathrm{D} \longrightarrow {}^3\mathrm{He}(0.82\,\mathrm{MeV}) + \mathrm{n}(2.45\,\mathrm{MeV}) \tag{1.4}$$

$$^2\mathrm{D} + {}^3\mathrm{T} \longrightarrow {}^4\mathrm{He}(3.5\,\mathrm{MeV}) + \mathrm{n}(14.1\,\mathrm{MeV}) \tag{1.5}$$

$$^2\mathrm{D} + {}^3\mathrm{He} \longrightarrow {}^4\mathrm{He}(3.6\,\mathrm{MeV}) + \mathrm{p}(14.7\,\mathrm{MeV}) \tag{1.6}$$

where the energy released by the reactions can be found in [31]. As it can be seen, the energy obtained by means of a nuclear fusion reaction is of the order of $1 - 10$ MeV, one million times the typical value of $1 - 10$ eV that can be obtained by means of chemical combustion of fossil fuels, showing that, if carried out, fusion could be a promising energy source for the future.
To realize this project, the choice of the reaction is very important because it determines key aspects of the rest. Nowadays, the reaction candidate is (1.5) because it is the one that maximizes the cross section (that means the probability of realizing it) at the lowest value of the scattering energy, as it is evident from figure 1.2.

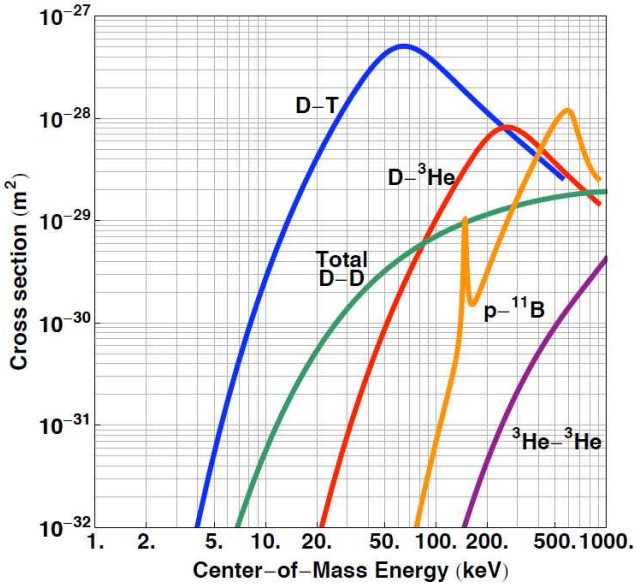

Figure 1.2: Fusion reactions cross section, as function of the center of mass energy.

However, there are also critical aspects related to it, because a radioactive isotope not present in nature like tritium is involved and indirectly ionizing radiation (neutron) is produced: for these reasons, also the other reactions are not completely discarded at least for second generation reactors. The disadvantages in exploiting nuclear fusion are in any case minor than in the case of nuclear fission because developing uncontrolled chain reactions is physically impossible and the activation induced in materials has a duration of about 100 years, with respect to 10^5-10^6 years of fission.

1.2 Plasma confining methods

The relatively high collision energies that are required to achieve non-negligible values of the cross sections in figure 1.2 imply working with matter in the state of plasma, that is a state of matter characterized by a considerable degree of ionization so that the charged particles that make it up are able to display a collective behaviour.
In this ionized gas, the encounter of a deuterium and tritium nuclei not always gives rise to a fusion reaction because the largely dominant outcome of the collision is Coulomb scattering, since its cross section is approximately two orders of magnitude greater (see figure 1.3).

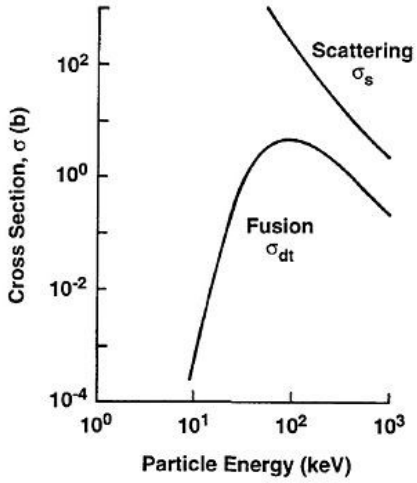

Figure 1.3: Comparison between Coulomb scattering and deuterium-tritium fusion cross sections.

To realize a sufficient number of fusion reactions, plasma needs to be confined in a finite region of space for a relatively long time: in this way the number of particle collisions is sufficiently high to allow fusion to take place and to guarantee a satisfactory gain in energy.
Different confining methods are known (as shown in figure 1.4): first of all, gravitational confinement (the natural way of confining plasma in stars) has to be mentioned, then the artificial methods of inertial and magnetic confinement. Inertial confinement basically consists in creating a deuterium-tritium solid target bombed with high power laser to generate the evaporation of the surface and the subsequent high pressure compression of the core that forces fusion to take place. The difficulties of this method are related to the high power management generated by the experiment.

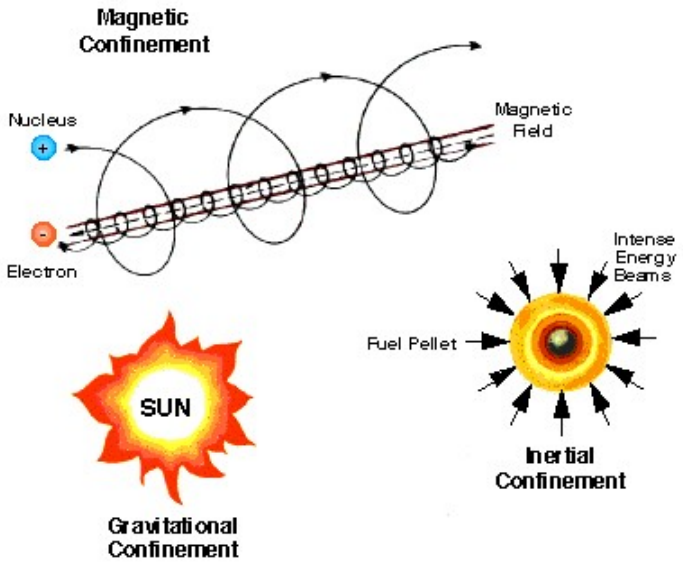

Figure 1.4: Three different confinement methods compared.

But the most promising confining method on which the European research project is centered (and on which this work is focused) is the magnetic one. The idea at the basis of magnetic confinement is quite easy: since no material surface able to support direct contact with high temperature plasma exists, a magnetic field distribution has to be generated in order to confine the plasma, exploiting its composition of charged particles.
In fact an electric $\mathbf{E}$ and magnetic field $\mathbf{B}$ affect the motion of a q charged particle with velocity $\mathbf{v}$ by means of a force $\mathbf{F}$, whose expression is given by the Lorentz formula:

$$\mathbf{F} = q\left(\mathbf{E} + \mathbf{v} \times \mathbf{B}\right). \tag{1.7}$$

A complete treatment of charged particles dynamics (including drifts) in presence of an electromagnetic field can be found in chapters 2 and 3 of Ref. [25]. The motion can be typically divided into two contributions: a uniform velocity gyro-motion with radius given by the Larmor radius r_L and angular frequency given by cyclotron frequency ω_c and a guide-center motion that follows magnetic field lines:

$$r_L = \frac{mv_\perp}{qB}, \qquad \omega_c = \frac{qB}{m}. \tag{1.8}$$

Using this basic idea, the early linear fusion devices were built exploiting a cylindrical symmetry magnetic field; the main defects of such a configuration was the lost of particles at the extremes that could be reduced but not cancelled by magnetic field intensification ("mirrors").
To overcome this difficulty, toroidal geometry was introduced. This type of geometry solves the problem of particle loss at the extremes, but introduces unavoidable deflections of particle trajectories with respect to the magnetic field line, known as "drifts". Drifts can be due to magnetic field gradients and curvature and can be almost completely cancelled (at least for thermal particles) with the introduction

of a poloidal component of the magnetic field.
Three different configurations (compared in figure 1.5) have been studied.

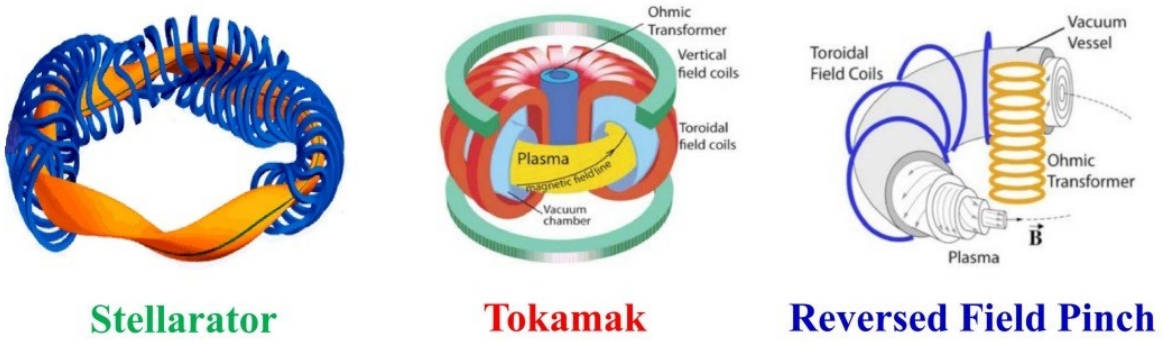

Figure 1.5: Comparison between the three main configurations for the magnetic confinement of fusion plasmas.

The main one is the tokamak, considered the most promising for the realization of the first fusion reactors. In this configuration, the toroidal component of the magnetic field is obtained thanks to toroidal magnetic field coils, while the poloidal one is guaranteed by the plasma current flowing in toroidal direction triggered by the central solenoid. Vertical field coils are instead used to control shape and positioning of the plasma inside the vacuum chamber. In the tokamak the poloidal field B_θ is smaller than the toroidal B_ϕ, $B_\theta/B_\phi << 1$.
Alternative configuration to the tokamak are the stellarator, characterized by the absence of plasma current and by special designed magnetic field coils able to generate both the components of the field, and the reversed-field pinch (RFP) characterized by high values of the plasma current, and reversed sign of the toroidal magnetic field in the external region. In the RFP the ordering of the magnetic field is $B_\theta \approx B_\phi$.
One of these experiments is located in Padova, at the C.N.R. research area and its name is RFX-mod (Reversed-Field eXperiment modified) and it is operated by Consorzio RFX. This machine can work in both tokamak and RFP configuration (this is a unique peculiarity) and restricting to the configuration RFP is the largest machine in the world.

1.3 Energy balance and expected operational conditions of a fusion reactor

A fusion reactor is a device able to generate a positive energy output by means of fusion reactions. Taking into account the main sources of gain and loss of energy, it is possible to predict approximately the operational conditions of future reactors. A precise analysis about this topic can be found in chapter 1 of Ref. [55]: only the main results are reported in this section.
The main factors that contribute to the change of the plasma energy density w are: the power heating input p_H which can be injected from outside, the α particles power heating p_α produced by fusion reactions, the power loss related to transport p_L and to radiation p_R. In one formula (all the powers involved are expressed per unit of volume):

$$\frac{dw}{dt} = p_H + p_\alpha - p_L - p_R. \tag{1.9}$$

With simplifying hypotheses of quasi-neutrality ($n_e \approx n_i \approx n$), equal ionic and electron temperature ($T_e \approx T_i \approx T$) and that the plasma can be treated as a monoatomic gas one gets:

$$w = 3nT, \tag{1.10}$$

where it is customary to express temperature as the associated energy (by means of the Boltzmann constant k_B).
While neutrons cannot be held in the plasma by the magnetic field, alpha particles in principle should remain trapped thanks to their electric charge and consequently contribute to plasma heating. In particular, their contribution is proportional to the energy brought by each single particle ($E_\alpha = 3.5\,\mathrm{MeV}$) and to the number of reactions realized per unit of time and volume (reaction rate). Here, an optimized case in which deuterium and tritium have the same density n is considered:

$$p_\alpha = \frac{1}{4} n^2 \langle \sigma v \rangle E_\alpha, \tag{1.11}$$

where the symbol $\langle \sigma v \rangle$ denotes that the average is computed over the velocity components of the phase space.
The difficulty in modeling transport phenomena in fusion plasmas is also reflected in the estimate of the relative losses. Typically, power is expressed through a phenomenological parameter, called energy confinement time τ_E, that can be obtained experimentally or by means of scaling formulas:

$$p_L = \frac{w}{\tau_E}. \tag{1.12}$$

Three different phenomena contribute instead to radiation losses: cyclotron radiation, line spectroscopic emission and bremsstrahlung. Cyclotron radiation is to be attributed to the helical trajectory followed by a charged particle in presence of a magnetic field: its contribution is not relevant because plasma is able to reabsorb radiation at those frequencies. Also the line spectroscopic emission can be neglected if one considers that its main sources are impurity atoms not completely ionized, whose concentration should be reduced at the minimum possible level. Finally, the only contribution to the radiation losses that can not be neglected or reduced is the one related to bremsstrahlung: this phenomenon consists in the radiation emission due to acceleration that the charged particles undergo in a magnetized plasma. The power density associated to bremsstrahlung is usually calculated thanks to the following formula:

$$p_b = \alpha_b n^2 T^{1/2} \mathrm{Wm}^{-3}, \tag{1.13}$$

where the constant $\alpha_b = 5.35 \times 10^{-37}\,\mathrm{Wm^3keV^{-1/2}}$.
The ideal condition to be achieved by a fusion reactor is called ignition: in such a situation, the system has a positive power balance exploiting the energy generated by α particles, without the addition of external heating. This condition can be equivalently expressed by the following inequality:

$$n\tau_E > \frac{12T}{\langle \sigma v \rangle E_\alpha - 4\alpha_b T^{1/2}}. \tag{1.14}$$

However, ignition remains a very difficult target to be achieved because it requires very high temperatures (around 25 keV) well beyond the predicted temperature of future reactors that is about 10-15 keV. In this range the reactivity $\langle \sigma v \rangle$ is well described by the scaling formula:

$$\langle \sigma v \rangle = 1.1 \times 10^{-24} T^2 \mathrm{m^3 s^{-1}} \tag{1.15}$$

that implies the achievement of the final condition:

$$nT\tau_E > 5 \times 10^{21}\,\mathrm{m^{-3}keVs}. \tag{1.16}$$

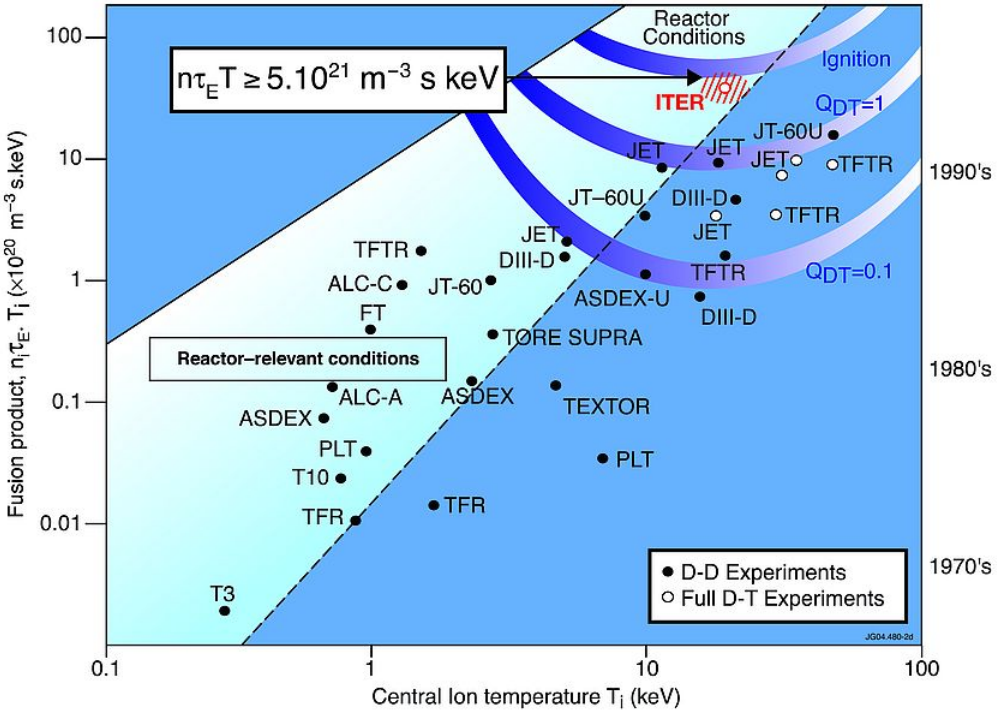

Figure 1.6: Achievements of the main fusion devices in terms of triple product.

This value can provide an idea of the target values for each quantity: $n \approx 10^{20}\,\mathrm{m}^3$, $T \approx 10 - 15\,\mathrm{keV}$ and $\tau_E \approx 3 - 5\,\mathrm{s}$. In figure 1.6 the best results achieved by tokamaks in terms of triple product ($nT\tau_E$) are exposed.

Since additional external heating is thought to be unavoidable for the next devices it is customary to define another parameter Q as the ratio between powers produced via thermonuclear reactions and provided to the plasma from outside. In this way, ignition would correspond to $Q = \infty$. A value of $Q = 1$ (break-even condition) indicates a balance of the powers related to the plasma, but to build a reactor able to exploit fusion for commercial purposes a value of Q around 50 is required.
The highest value of Q obtained in a fusion device is $Q = 0.65$, achieved by JET (Joint European Torus) experiment in 1997 (more details can be found in [30]). This record has not yet been reached by any other device because, since the 90s, no more performing experiments have been built. However, the next years will probably be a period of great advances in fusion research, thanks to the ITER project (International Thermonuclear Experimental Reactor), that will be the largest fusion device ever built, with operational parameters near the ones needed to reach the condition in equation (1.16) and a value of Q around 10, and other important devices like JT-60SA (upgrade of JT-60U, in Japan) and DTT, in Italy (Ref. [2]). ITER experiment is currently under construction at Cadarache, France, its first plasma is foreseen for 2025, with the most important campaign (in deuterium and tritium) between 2037-2042.

1.4 Fusion plasmas instabilities

One of the biggest problems affecting magnetic confinement machines is related to instabilities. In fact, when an equilibrium configuration is explored, the development of instabilities generally has deleterious effects, depending on the magnetic configuration considered and on the type of the instability developed: these effects can span from saturation of the instability up to disruptions (carefully described in Ref. [54]), dangerous events which lead to premature discharge termination: in this case the energy accumulated in the plasma is released in a very small time, and, consequently it is absorbed by the walls delimiting the plasma, causing damage to them in addition to the generation of high stresses on the external coils.

For these reasons, it is important to understand the physics of the phenomenon and, in particular the conditions under which it develops. Consequently a deep study of the stability of the configurations is necessary in order to discovery the origin of these drawbacks and to avoid their development: the study of instabilities is one of the main open research fields in fusion physics. A complete discussion about plasma instabilities is carried out in [55], in this section only the main points are reviewed.
From a qualitative point of view, the origin of the vast majority of the instabilities can be attributed to an initial perturbation with exactly the same periodicity of the magnetic field lines present on a determined magnetic surface. In this case, the stabilizing action of the magnetic tension (justified by the Alfvén theorem in hot conductive plasmas) is cancelled, allowing the instability to grow. Instabilities phenomenology strictly depends on the magnetic configuration considered and are divided into ideal and resistive (based on the role performed by electrical resistivity in its development) and into pressure driven and current driven (depending on which physical quantity provides free energy for the instability to develop).
The pressure driven instabilities can often be analyzed using the β parameter, defined as the ratio between kinetic and magnetic pressure:

$$\beta = \frac{p}{B^2/2\mu_0}. \tag{1.17}$$

This parameter quantifies the effectiveness of plasma confinement, given a determined magnetic field. Since $nT\tau_E \propto B^2\beta\tau_E$ it is desirable to increase the value of β as much as possible, however the maximum values achievable are strongly limited by the existence of a limit above which pressure driven instabilities development is found, called Troyon limit (presented in Ref. [60]):

$$\beta\,(\%) < g\frac{I(\mathrm{MA})}{a(\mathrm{m})B_\phi(\mathrm{T})}, \tag{1.18}$$

where a, B_ϕ, I are respectively minor radius, toroidal magnetic field and plasma current, while the constant g is called Troyon factor (its value is betweeen 2.8 and 3.5).
Among the current driven instabilities (that affect only tokamak and RFP configurations) those ideal are called kink modes, the resistive tearing mode.
Ideal kink modes are usually explored using the *energy principle* (introduced in Ref. [5]), by which instabilities are analyzed. It consists in the evaluation of the energy difference introduced by a spatial periodic perturbation (with poloidal and toroidal wave numbers m and n) $\boldsymbol{\xi} \propto \exp\left[i\left(m\theta + n\phi\right)\right]$:

$$\delta W = -\frac{1}{2}\int \boldsymbol{\xi}\cdot\mathbf{F}dV, \tag{1.19}$$

where $\mathbf{F}$ is a force per unit of volume evaluated taking into account first order perturbation terms:

$$\mathbf{F} = \mathbf{J}_1\times\mathbf{B}_0 + \mathbf{J}_0\times\mathbf{B}_1 - \nabla p_1, \tag{1.20}$$

if the gain in energy is positive, the perturbation is disadvantaged in its development, otherwise it's advantaged, because the system tends to minimize its energy δW is the opposite of its variation. Carrying out the calculations related to equation (1.19) an important operational limit related to the safety factor $q(r)$ is found. This factor is a parameter (dependent on the magnetic surface considered) defined as the toroidal angle $\Delta\phi$ necessary to complete an entire poloidal lap (2π), that expressed in terms of magnetic fields in cylindrical geometry turns out to be:

$$q(r) = \frac{\Delta\phi(r)}{2\pi} = \frac{rB_\phi(r)}{R_0B_\theta(r)}, \tag{1.21}$$

with $B_\theta(r)$ poloidal magnetic field and R_0 major radius of the torus. The limit given by the magnetohydrodynamic analysis is called Kruskal-Shafranov and corresponds to the requirement: $q(r) > 1$.

In particular the value $q = 1$ is reached for tokamak only on the magnetic axis ($r = 0$), thanks to a phenomenon called sawtooth oscillations that consists in an oscillation of the central temperature values connected precisely to a resistive instability, while for the RFP configuration $q(0) << 1$, typically $q(0) \sim a/r$.
Tearing modes are instabilities ruled by the presence of a non negligible resistivity. In particular, in fusion plasmas the formation of regions called *current sheets* characterized by a very strong convexity of the magnetic field (high $\nabla^2 B$) can occur and, in this case, the role of resistivity is no longer negligible, Alfvén theorem does not hold anymore and the topology of the magnetic field lines can vary during the so called reconnection events. Tearing mode instability cause the breaking up of the current sheet in different regions with separated magnetic topology called *magnetic islands* (1.7).

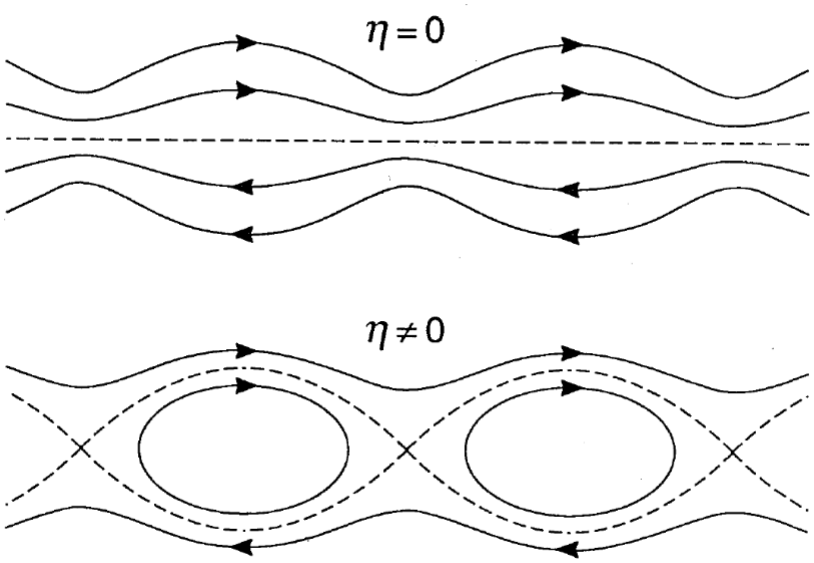

Figure 1.7: Magnetic field lines comparison in case of ideal kink and resistive tearing mode instability.

When a non zero resistivity is considered, the result of a stability analysis of the type (1.19) shows the presence of a singularity in the energy difference introduced by the perturbation when the following condition is satisfied:

$$q = -\frac{m}{n}. \tag{1.22}$$

It is worth noting that, according to the Fourier expansion used in the code SpeCyl and in this thesis (see appendix A.2), the wave number of a perturbation is $m\theta + n\phi$, and therefore the resonant condition holds a minus sign, $-m/n$. If the latter condition is satisfied by the perturbation there is a resonant magnetic surface where the stabilization effect of the magnetic field is absent and the perturbation can grow undisturbed. The most dangerous instability are those characterized by low integer wave numbers value: in particular, for the tokamak configuration, the conditions to avoid are $q(a) = 2$ (satisfied by the perturbations with $m = 1$, $n = -2$ and its harmonics), $q(a) = 3$, and more generally $q(a) = m/n$ with low m, n: in this case the working parameters are chosen in order to obtain $3 < q(a) < 4$.
Another very important type of instability introduces the density limit: practically it consists in a limit related to the number density above which instabilities are found. From a theoretical point of view a complete explanation of this limit is not yet available. However, a phenomenological law based on experimental data-sets was found by Greenwald [26]. It states that stability (with respect to the density limit) is obtained for averaged value of density $\bar{n}$, such that:

$$\bar{n}\left(10^{20}\,\mathrm{m}^{-3}\right) < \frac{I\,(\mathrm{MA})}{\pi a^2\left(\mathrm{m}^2\right)}, \tag{1.23}$$

in which the right hand side is called *Greenwald density* n_G. The physical origin of this limit is not very clear. There are theories which explain the density limit as a fundamental limit based on atomic processes [13]. One of the most accredited explanation suggests instead the density limit to be linked with the high concentration of not entirely ionized impurities in the plasma edge: the latter increase the irradiated power and consequently cause the cooling of the plasma external region and the increase of the resistivity (because it will be shown in the next chapter that $\eta \propto T^{-3/2}$). As a final result, the decrease of current causes a contraction of the plasma column that brings to the loss of stability.
Also for the density limit a strong relationship with resonant mode is believed, in particular for the mode $m = 2$, $n = -1$ in the tokamak configuration and $m = 0$ $n = -1$ in the RFP configuration.
The operational parameters with respect to the resistive instabilities are well summarized in the so called Greenwald plot (see figure 1.8): as it is shown the limits are usually relaxed if one increases the input power.

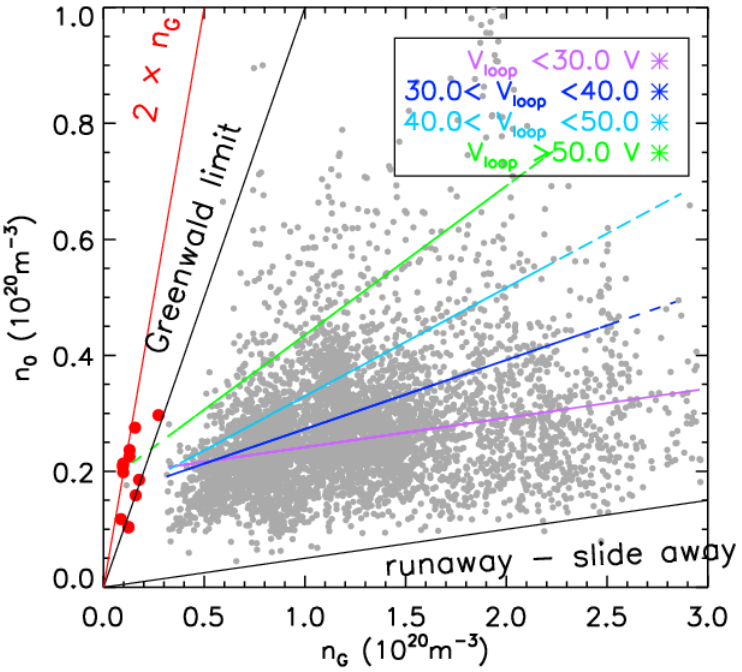

Figure 1.8: Operational space of RFX-mod in the Greenwald plane: straight lines are interpolation of points grouped according to values of loop voltage, which is proportional to the ohmic input power. Red points are discharges at low current and $n_0 \sim n_G$. Picture adapted from Ref. [46].

In this work an interpretation of the density limit (in the case of RFP magnetic configuration) will be provided, trying to connect it with dimensionless fluid-dynamical numbers defined in the context of MHD models and with the analysis of experimental data related to measures of the magnetic turbulence in then edge of RFX-mod plasmas.

Chapter 2

Magnetohydrodynamics models

The aim of this chapter is the introduction of magneto-fluid models for studying fusion plasmas. This approach has turned out to be very efficient and useful, despite the high number of hypotheses needed in order to develop it: here, the most important arguments of the derivation are shown, without getting into all the mathematical details that were performed in the '50 and '60 by brilliant physicists like Landau, Balescu, Chapman, Enskog and Braginskii. Particular attention will be paid to transport modeling and the expression of the relative coefficients as functions of the main plasma parameters.
In parallel, the visco-resistive MHD model will be introduced, with its additional and simplified hypotheses: in this context, the emergence of dimensionless fluid numbers is shown, and their driving role in plasma physics is highlighted. Finally, making use of the results obtained for transport modelling (in the MHD approach) an estimate of the transport coefficients and fluid numbers as function of plasma parameters will be found. The latter passage is fundamental in order to allow the evaluation of these quantities using experimental data coming from the RFX-mod experiment.

2.1 Plasma kinetic model

Each time one wants to achieve the comprehension of a complex system by means of a physical model it is necessary to choose the right level of description of the physical system, taking into account the specific phenomenon of interest, the physical quantities that can be experimentally measured and that should be predicted by the model and, finally, the possibility of formulating useful forecasts by means of analytical calculations or, more likely, numerical simulations requiring an acceptable computing power.
In the introductory part of [18] an exhaustive and brief description of the different dynamical theories used to describe fluids and plasmas are shown, pointing out that the basic requirements for this type of theories are: the mathematical tools and variables to describe a system state and a set of equations that can be used in order to predict the time evolution of the system given a determined initial state.
Since fusion plasmas are physical systems composed by a huge number of particles ($N \approx N_{av}$), in this work the construction of macroscopic models will be immediately started (following mainly the notation and the procedures exposed in [21]) without developing the microscopic approaches (at quantum or classical level) that require the solution of an extremly high number of differential equations (Schrödinger's or Newton's) and from which it is particularly difficult to draw interesting conclusions for our purposes.
For these reasons, the system in question is supposed to be such that it can contain a sufficiently high number of small volumes (to allow a macroscopic differential treatment) and that each small volume contains an enormous number of particles: this hypothesis holds for all the systems that can be studied at a thermodynamic level.
Let $\rho_s(\mathbf{x}_1, \mathbf{u}_1, \ldots, \mathbf{x}_N, \mathbf{u}_N, t)$ be the microscopic phase space density of N classical particles of the species s with positions $\mathbf{x}_1$, ..., $\mathbf{x}_N$ and velocities $\mathbf{u}_1$, ..., $\mathbf{u}_N$ in the Γ space. Than, using Liouville theorem:

$$\frac{d\rho_s}{dt}\left(\mathbf{x}_1, \mathbf{u}_1, \ldots, \mathbf{x}_N, \mathbf{u}_N, t\right) = 0, \tag{2.1}$$

where $\frac{d}{dt}$ denotes the total lagrangian derivative. Liouville theorem expresses the phase space conservation in Γ space. Equation (2.1) is easily rewritten as:

$$\frac{\partial \rho_s}{\partial t} + \sum_{i=1}^{N} \mathbf{u}_i \cdot \nabla_{\mathbf{x}_i} \rho_s + \sum_{i=1}^{N} \frac{\mathbf{F}_{i,s}}{m_s} \cdot \nabla_{\mathbf{u}_i} \rho_s = 0, \tag{2.2}$$

in which the symbols $\nabla_{\mathbf{x}_i}$ and $\nabla_{\mathbf{u}_i}$ denote the gradients calculated with respect to the spatial coordinates and to the velocities of the i-th particle and the variables m_s and $\mathbf{F}_{i,s}$ are respectively the mass and the force exerted on the i-th particle of the s species. Equation (2.2) is easily derived but needs a very difficult solution. In fact the ensemble density ρ_s contains in its argument a dependence on the trajectories of all the particles considered, whose determination is equivalent to the solution of the many-body problem.
In order to simplify this problem, the ensemble average of ρ_s can be calculated, giving origin to the single particle distribution function:

$$f_s\left(\mathbf{r}, \mathbf{u}, t\right) := \left\langle \rho_s\left(\mathbf{x}_1, \mathbf{u}_1, \ldots, \mathbf{x}_N, \mathbf{u}_N, t\right)\right\rangle_{ens}, \tag{2.3}$$

that has the physical meaning of number of particles with position between $\mathbf{r}$ and $\mathbf{r} + d\mathbf{r}$, velocity between $\mathbf{u}$ and $\mathbf{u} + d\mathbf{u}$ at the time t, per unit of phase space volume. To find an equation that rules the evolution of f_s, equation (2.2) can be averaged: the only non trivial term is the last adding because the expression of $\mathbf{F}_{i,s}$ is given by the Lorentz force (in the case of plasmas) where a velocity dependence is contained, so that a correlation between the two factors is generated and the product average can not be trivially factorized. In other words, a correlation term $C_s(f)$ has to be introduced:

$$\left\langle \sum_{i=1}^{N} \frac{\mathbf{F}_{i,s}}{m_s} \cdot \nabla_{\mathbf{u}_i} \rho_s \right\rangle_{ens} = \frac{\mathbf{F}_s}{m_s} \cdot \nabla_{\mathbf{u}} f_s - C_s(f), \tag{2.4}$$

where $\mathbf{F}_s$ represents an averaged force due to smooth electromagnetic fields generated by all the particles contribution. The final kinetic equation obtained is:

$$\frac{\partial f_s}{\partial t} + \mathbf{u} \cdot \nabla f_s + \frac{\mathbf{F}_s}{m_s} \cdot \nabla_{\mathbf{u}} f_s = C_s\left(f\right). \tag{2.5}$$

$C_s(f)$ is usually called collision operator because collisions are the main physical mechanism that generates non zero correlation terms and it is a very difficult term to be evaluated: this is why, where possible, such term is neglected (Vlasov limit). However, in literature, expressions for $C_s(f)$ exist: in the case of neutral gases the operator was calculated by Boltzmann (with the hypotheses of binary collisions) and it can be found, for example in [18], while for the case of plasmas an expression was found by Landau under strict hypotheses, including the existence of only two species (ions and electrons), conservation of particle number for each species (absence of fusion, recombination, charge exchange, ...) and the dependence only on the one particle distribution function (absence of higher order correlation). More details about the Landau collision integral can be found in [24] or in the original paper [32]. For the aim of this work it is sufficient to know that the collisional processes conserve number of particles, momentum and energy at each point, without entering in the details of collisions modelling.
The kinetic approach has two decisive disadvantages: from one side the distribution function f_s has a seven dimensional dependence that makes computer simulations more difficult to implement, on the other side it is not easily measurable experimentally. Despite this disadvantages, the kinetic approach

is widely used to simulate plasma turbulence and transport in the so-called gyrokinetic codes (see Ref. [15] for more details): these codes typically analyze small-scale structures on fast timescales, and the magnetic field is generally not evolved self-consistently in the code. Modern supercomputers allow for obtaining more and more efficient gyrokinetic simulations and presently much effort is devoted in this field of research.

2.2 Moments of the kinetic equation

An approach complementary to that used in gyrokinetic codes is to take the moments of the distribution function: this approach gives rise to the second, large family of codes used in plasma physics, namely the Magnetohydrodynamic (MHD) codes. The k-th moment of the ensemble averaged distribution function $f_s(\mathbf{r}, \mathbf{u}, t)$ is defined as follows:

$$\mathbf{M}_k(\mathbf{r}, t) := \int \mathbf{u} \cdot ... \cdot \mathbf{u} f_s(\mathbf{r}, \mathbf{u}, t)\, d^3\mathbf{u}, \tag{2.6}$$

repeating the $\mathbf{u}$ factors k times. Moments connect the distribution function to easily measurable physical quantities. In particular, number density $n_s(\mathbf{r}, t)$, flux density $n_s\mathbf{v}_s$, stress tensor $\mathbf{P}_s$ and energy flux density $\mathbf{Q}_s$ can be defined using the moments of the first orders:

$$n_s(\mathbf{r}, t) := \int f_s(\mathbf{r}, \mathbf{u}, t)\, d^3\mathbf{u}, \tag{2.7}$$

$$n_s\mathbf{v}_s(\mathbf{r}, t) := \int \mathbf{u} f_s(\mathbf{r}, \mathbf{u}, t)\, d^3\mathbf{u}, \tag{2.8}$$

$$\mathbf{P}_s(\mathbf{r}, t) := \int m_s \mathbf{u}\mathbf{u} f_s(\mathbf{r}, \mathbf{u}, t)\, d^3\mathbf{u}, \tag{2.9}$$

$$\mathbf{Q}_s(\mathbf{r}, t) := \int \frac{1}{2} m_s u^2 \mathbf{u} f_s(\mathbf{r}, \mathbf{u}, t)\, d^3\mathbf{u}. \tag{2.10}$$

In the definition (2.8), a new quantity called flow velocity $\mathbf{v}_s$ is introduced. Defining also the relative velocity $\mathbf{w}_s := \mathbf{u} - \mathbf{v}_s$ and, consequently, pressure tensor $\mathbf{p}_s$ and heat flux density $\mathbf{q}_s$ are introduced:

$$\mathbf{p}_s(\mathbf{r}, t) := \int m_s \mathbf{w}\mathbf{w} f_s(\mathbf{r}, \mathbf{u}, t)\, d^3\mathbf{u} \tag{2.11}$$

$$\mathbf{q}_s(\mathbf{r}, t) := \int \frac{1}{2} m_s w^2 \mathbf{w} f_s(\mathbf{r}, \mathbf{u}, t)\, d^3\mathbf{u} \tag{2.12}$$

Since pressure is a typical scalar quantity, a scalar quantity (scalar pressure p_s) can be associated to the tensor in (2.11) as $p_s := \frac{1}{3} Tr(\mathbf{p}_s)$ and, finally it is natural to define as kinetic temperature of equilibrium $T_s := \frac{p_s}{n_s}$. To compute the moments of the kinetic equation, also the moments of the collision operator have to be found.
To find the moments of the collision operator it is necessary to hypothesize its bilinearity with respect to the single particle distribution function:

$$C_s(f) = \sum_{s'} C_{ss'}(f_s, f_{s'}), \tag{2.13}$$

with $C_{ss'}(f_s, f_{s'})$ bilinear in both its arguments. In this way, it is possible to introduce the friction force exerted on the species s by the species s' ($\mathbf{F}_{ss'}$), the total force experienced by the species s ($\mathbf{F}_s$) and, similarly, the difference in kinetic energy of the species s due to s' ($W_{ss'}$) and the total change in energy of the species s (W_s).
The final steps to get fluid macroscopic equations of the considered system consist in the calculation of the first three orders moments of the equation (2.5), applying the procedure indicated in the definition (2.6). Avoiding repeating all the algebraic steps, only the main ideas to get the final result are exposed. First of all, flow in the velocity space of the Lorentz force $\mathbf{F}$ is incompressible:

$$\nabla_{\mathbf{u}} \cdot \mathbf{F} = q\nabla_{\mathbf{u}} \cdot (\mathbf{E} + \mathbf{u} \times \mathbf{B}) = q\left[(\nabla_{\mathbf{u}} \times \mathbf{u}) \cdot \mathbf{B} - \mathbf{u} \cdot (\nabla_{\mathbf{u}} \times \mathbf{B})\right] = 0, \tag{2.14}$$

so that the equation (2.5) can be rearranged and the moments calculus ($k = 0, 1, 2$) can be set up:

$$\int \frac{m_s}{k!}\mathbf{u} \cdot ... \cdot \mathbf{u}\left(\frac{\partial f_s}{\partial t} + \nabla \cdot (\mathbf{u}f_s) + \nabla_{\mathbf{u}} \cdot \left(\frac{\mathbf{F}_s}{m_s}f_s\right)\right) d^3\mathbf{u} = \int \frac{m_s}{k!}\mathbf{u} \cdot ... \cdot \mathbf{u}C_s(f)\, d^3\mathbf{u}. \tag{2.15}$$

Performing the integration, using the Gauss theorem (with the hypothesis that fields vanish as $r \to \infty$) and making use of the definition introduced in this section one finds the continuity equation ($k = 0$):

$$\frac{\partial n_s}{\partial t} + \nabla \cdot (n_s\mathbf{v}_s) = 0, \tag{2.16}$$

the momentum conservation equation ($k = 1$):

$$\frac{\partial (m_s n_s \mathbf{v}_s)}{\partial t} + \nabla \cdot \mathbf{P}_s - e_s n_s (\mathbf{E} + \mathbf{v}_s \times \mathbf{B}) = \mathbf{F}_s, \tag{2.17}$$

and, finally, the energy conservation equation ($k = 2$):

$$\frac{\partial}{\partial t}\left(\frac{3}{2}p_s + \frac{1}{2}m_s n_s v_s^2\right) + \nabla \cdot \mathbf{Q}_s - e_s n_s \mathbf{E} \cdot \mathbf{v}_s = W_s + \mathbf{v}_s \cdot \mathbf{F}_s. \tag{2.18}$$

The main concept expressed by these equations is the conservation of a physical quantity (at a macroscopic) level as consequence of the conservation at the microscopic interaction level: in particular, it is evident that the time variation of one of these conserved quantities inside a volume has to be balanced by its flow through the volume surface or by the interaction with other species (terms containing $\mathbf{F}_s, W_s$) and with the electromagnetic field (terms containing $\mathbf{E}$ and $\mathbf{B}$).

2.3 Braginskii equations and transport coefficients

Equations (2.16), (2.17) and (2.18) can be rewritten in a more manageable and useful form, performing some tensor algebra, introducing the convective derivative d/dt and the tensor operator $: \nabla$ that are defined in the following way:

$$\frac{d}{dt} := \frac{\partial}{\partial t} + \mathbf{v}_s \cdot \nabla, \qquad \mathbf{S} : \nabla\mathbf{T} = (S)_{ij}\frac{\partial T_j}{\partial x_i}, \tag{2.19}$$

where $\mathbf{S}$, $\mathbf{T}$ are rank two tensors and Einstein convention is used. The Braginskii equations thus turn out to be:

$$\frac{dn}{dt} + n\nabla \cdot \mathbf{v}_e = 0, \tag{2.20}$$

$$m_e n \frac{d\mathbf{v}_e}{dt} + \nabla p_e + \nabla \cdot \mathbf{\Pi}_e + en\left(\mathbf{E} + \mathbf{v}_e \times \mathbf{B}\right) = \mathbf{F}, \tag{2.21}$$

$$\frac{3}{2}\frac{dp_e}{dt} + \frac{5}{2}p_e \nabla \cdot \mathbf{v}_e + \mathbf{\Pi}_e : \nabla \mathbf{v}_e + \nabla \cdot \mathbf{q}_e = W_e, \tag{2.22}$$

for the electrons and similarly for ions:

$$\frac{dn}{dt} + n\nabla \cdot \mathbf{v}_i = 0, \tag{2.23}$$

$$m_i n \frac{d\mathbf{v}_i}{dt} + \nabla p_i + \nabla \cdot \mathbf{\Pi}_i - en\left(\mathbf{E} + \mathbf{v}_i \times \mathbf{B}\right) = -\mathbf{F}, \tag{2.24}$$

$$\frac{3}{2}\frac{dp_i}{dt} + \frac{5}{2}p_i \nabla \cdot \mathbf{v}_i + \mathbf{\Pi}_i : \nabla \mathbf{v}_i + \nabla \cdot \mathbf{q}_i = W_i, \tag{2.25}$$

in both cases the pressure tensor is written as a sum of a diagonal part that models the effect of the isotropic pressure, and an off-diagonal part related to viscous stresses:

$$\mathbf{p}_s = p_s \mathbb{1}_3 + \mathbf{\Pi}_s. \tag{2.26}$$

Moreover, the quasi-neutrality of the plasma is assumed: $n_e \approx Z n_i \approx n$. In other words, on the macroscopic scale to which the plasma is described, the charge unbalance is neglected and the presence of electric fields is consequently negligible. In fact, if an imbalance of charges develops, the corresponding electric field would move the plasma charges (which are free) in order to eliminate the imbalance itself, in a very rapid time. Equations (2.20)-(2.25) were introduced for the first time by Braginskii in 1965 [9].
Braginskii equations present a fundamental defect (also common in the case of neutral fluids): the incompleteness. The number of unknowns largely exceed the number of available equations, because passing from the kinetic approach to the magneto-fluid approach only three moments of the kinetic equations are calculated: closure could be restored calculating all of the moments in the kinetic equation. Such an approach is clearly impractical because the higher order moments have not an evident physical meaning and the solutions of all the equations involved it is equivalent to solve the many body problem.
Closure procedures were introduced by Chapmann-Enskog and Balescu respectively in [17] and [4] and they are based on expansion of the single particle distribution function $f\left(\mathbf{r}, \mathbf{u}, t\right)$ as sum of an equilibrium term (typically Maxwell-Boltzmann distribution) $f_0\left(\mathbf{r}, \mathbf{u}\right)$ and a small perturbation one:

$$f\left(\mathbf{r}, \mathbf{u}, t\right) \approx f_0\left(\mathbf{r}, \mathbf{u}\right) + \epsilon f_1\left(\mathbf{r}, \mathbf{u}, t\right), \tag{2.27}$$

$$f_0\left(\mathbf{r}, \mathbf{u}\right) = n(\mathbf{r})\left(\frac{m}{2\pi T\left(\mathbf{r}\right)}\right)^{3/2} \exp \frac{m\left(\mathbf{u} - \mathbf{v}\right)^2}{2T\left(\mathbf{r}\right)}, \tag{2.28}$$

with f_0 and f_1 of the same order and ϵ is a small parameter expansion. The f_1 perturbation term allows the modelling of transport, that otherwise would be set to zero in the case of equilibrium distribution functions. The choice of ϵ strongly depends on the fluid considered: in the case of magnetically confined fusion plasma the parameter can be chosen as the ratio between Larmor radius r_L and the macroscopic scale length of the device L, because in this case the following condition is satisfied:

$$\epsilon = \frac{r_L}{L} << 1. \tag{2.29}$$

In particular, in this limit confinement phenomena are dominating over collisional phenomena, being the Larmor gyro-radius smaller than the mean free path, or, equivalently defining the collisional time for ions and electrons τ_i, τ_e:

$$\omega_i \tau_i, \quad \omega_e \tau_e << 1. \tag{2.30}$$

Assuming the hypotheses of bi-linearity (2.13) of the collision operator, the closure procedure can be performed expanding f_1 with a polynomial expansion in the velocity space by means of Laguerre polynomials (as Chapmann-Enskog did) or Hermite polynomials (as Balescu did). It was shown by Balescu that the relative difference between its method and the Chapmann-Enskog one is below 1%. Such expansions are fairly prohibitive from the point of view of the calculations because they involve terms that are tensors of increasing dimension by the term considered. For this reason, in this work the mathematical steps are not repeated (anyhow they can be found in [17], [4]) but only the final result with the procedure that gives rise to it will be mentioned. Truncating the f_1 expansion at the second order, replacing it in the moments of the kinetic equation and solving the simplified form for the moments, one can get the laws that rule transport with its relative coefficients: in the next subsection the fundamental laws of transport are written and their physical meaning is exposed. Since one of the aim of this chapter is to derive, as final result, the visco-resistive model, the discussion is limited to the transport of electric charge and momentum, avoiding to enter in the details of heat transport in plasmas, that can be anyway found in [21].

2.3.1 Electric charge transport

The strong anisotropy introduced by the magnetic field makes sure that transport physics strictly depends on its direction with respect to the latter. From the closure procedures, an important transport coefficient arises: it is the electrical conductivity σ (the reciprocal of the resistivity η) that takes on different values depending on the direction of current with respect to the magnetic field:

$$\sigma_{\parallel} = 1.96 \frac{n e^2 \tau_e}{m_e}, \qquad \sigma_{\perp} = 0.51 \sigma_{\parallel} = \frac{n e^2 \tau_e}{m_e}. \tag{2.31}$$

The dependence in 2.31 is explained by the following consideration: since $\mathbf{F}$ is a friction force per unit of volume, it will be increased by the momentum lost by the electrons (the species that originate the current) in favour of ions:

$$\mathbf{F} \propto \frac{n m_e \left(\mathbf{v}_e - \mathbf{v}_i\right)}{\tau_e} = \frac{n^2 e^2 \left(\mathbf{v}_e - \mathbf{v}_i\right)}{n e^2 \tau_e / m_e} \propto \frac{n e \mathbf{j}}{\sigma}, \tag{2.32}$$

that justifies the dependencies in (2.31).

2.3.2 Momentum transport

The case of momentum transport with its relative coefficients (viscosity) is, in general, very difficult, since the quantity transported is now a vector (no longer a scalar as in the cases of electric charge and heat). In the simpler case of neutral fluids or, in general, in the case of short range interactions with a faster fall than the electromagnetic one, the phenomenon can be described using a rate of strain tensor W that is symmetric and traceless:

$$W_{i,j} = \frac{\partial v_i}{\partial r_j} + \frac{\partial v_j}{\partial r_i} - \frac{2}{3} \nabla \cdot \mathbf{v} \delta_{i,j}. \tag{2.33}$$

Instead, in a magnetized plasma where the main force on action is the Coulomb interaction, the best description is given by a tensor that can be split into five different components:

$$\mathbf{\Pi} = \sum_{n=0}^{4} \mathbf{\Pi}_n. \tag{2.34}$$

The first one is related to parallel transport of momentum components parallel to the magnetic field lines:

$$\mathbf{\Pi}_0 = -3\mu_0 \left(\mathbf{bb} - \frac{1}{3}\mathbb{1}\right)\left(\mathbf{bb} - \frac{1}{3}\mathbb{1}\right) : \nabla \mathbf{v}, \tag{2.35}$$

where the coefficient μ_0 is the proportional to the parallel viscosity and it is found to be:

$$\mu_0^e = 0.73 n \tau_e T_e, \qquad \mu_0^i = 0.96 n \tau_i T_i. \tag{2.36}$$

In the perpendicular direction the transport of perpendicular momentum components is ruled by the sum of two tensors:

$$\mathbf{\Pi}_1 = -\mu_1 \left[\mathbb{1}_\perp \cdot \mathbf{W} \cdot \mathbb{1}_\perp + \frac{1}{2}\mathbb{1}_\perp \left(\mathbf{b} \cdot \mathbf{W} \cdot \mathbf{b}\right)\right], \tag{2.37}$$

$$\mathbf{\Pi}_2 = -4\mu_1 \left[\mathbb{1}_\perp \cdot \mathbf{W} \cdot \mathbf{bb} + \mathbf{bb} \cdot \mathbf{W} \cdot \mathbb{1}_\perp\right], \tag{2.38}$$

where $\mathbb{1}_\perp$ is defined as $\mathbb{1}_\perp := \mathbb{1} - \mathbf{bb}$ and the perpendicular viscosity results to be reduced of a factor $(r_L/l)^2$ by the magnetic confinement:

$$\mu_1^e = 0.51 \frac{n T_e}{\omega_e^2 \tau_e}, \qquad \mu_1^i = \frac{3 n T_i}{10 \omega_i^2 \tau_i}. \tag{2.39}$$

The last contribution comes from the so called gyroviscosity and it describes the dissipation in a direction perpendicular to the momentum component transported; it is given by a sum of two components:

$$\mathbf{\Pi}_3 = \frac{\mu_3}{2}\left[\mathbf{b} \times \mathbf{W} \cdot \mathbf{bb} - \mathbb{1}_\perp \cdot \mathbf{W} \times \mathbf{b}\right], \tag{2.40}$$

$$\mathbf{\Pi}_4 = 2\mu_3 \left[\mathbf{b} \times \mathbf{W} \cdot \mathbf{bb} - \mathbf{bb} \cdot \mathbf{W} \times \mathbf{b}\right], \tag{2.41}$$

where the μ_3 coefficient (that is proportional to the gyroviscosity) is given by:

$$\mu_3^e = -\frac{n T_e}{2\left|\omega_e\right|}, \qquad \mu_3^i = \frac{n T_i}{2\omega_i}. \tag{2.42}$$

The origins of the giroviscosity (see figure 2.1) can be explained in terms of combined effects of the magnetic field and the presence of a component of the temperature gradient perpendicular to the magnetic field, due to which particles with a different kinetic energy have to face, generating a friction in the direction perpendicular to both $\mathbf{B}$ and ∇T_e.

In general, replacing the values of typical fusion plasma parameter one can find that the higher values for the viscosity coefficients are related to ion species, so that these particles are determinant in momentum transport mechanism, thanks to their greater mass that allows a longer collisional time and a smaller cyclotron frequency with respect to the electrons.

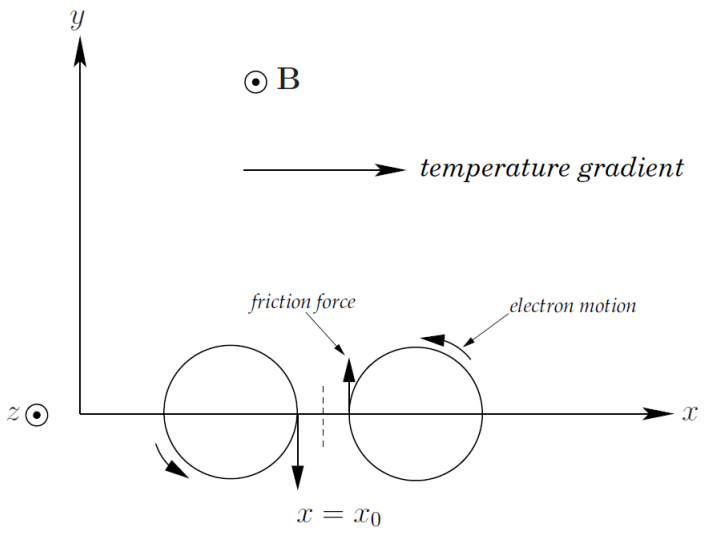

Figure 2.1: Origin of the gyroviscosity, due to the presence of a gradient in temperature perpendicular to the magnetic field.

The most important achievement of this paragraph is the modeling (in the context of Braginskii equations) of transport phenomena by means of coefficients (resistivity and viscosity) expressed in terms of plasma parameters (like density and pressure) in formulas (2.31), (2.36), (2.39) and (2.42).

2.4 Single fluid MHD equations

A further approximation in the case of magneto-fluid approach consists in the so called single fluid model. This model is valid only if the plasma is studied on a sufficiently large space-time scale so that no charge unbalance can be detected experimentally on that macroscopic scale. From a more quantitative point of view, it means that the space scale L and the time scale t must satisfy the following relations:

$$L >> \lambda_D, \qquad t >> \omega_p^{-1}, \tag{2.43}$$

where the Debye length λ_D and the plasma frequency ω_p are defined as follows:

$$\lambda_D := \sqrt{\frac{\epsilon_0 T_e}{ne^2}}, \qquad \omega_p := \sqrt{\frac{ne^2}{\epsilon_0 m_e}}. \tag{2.44}$$

These hypotheses are satisfied in the case of magnetized fusion plasmas and, for this reason, it is possible to define a single fluid mass density ρ, velocity $\mathbf{v}$, scalar pressure p, viscous stress tensor $\mathbf{\Pi}$ and the density current $\mathbf{j}$ (the latter has already been encountered in the previous paragraph):

$$\rho := (m_i + m_e)\, n, \qquad \mathbf{v} := \frac{m_i \mathbf{v}_i + m_e \mathbf{v}_e}{m_i + m_e}, \qquad p := p_i + p_e, \qquad \mathbf{\Pi} := \mathbf{\Pi}_i + \mathbf{\Pi}_e. \tag{2.45}$$

The single fluid equations are easily found in terms of linear combinations of the equations (2.20) - (2.25) with any further simplification hypotheses. They are simply found using simple algebra passages but, in any case, the explicit derivation is carried out in [25] and [18].
Continuity equation is obtained by means of the combination $m_e\,(2.20) + m_i\,(2.23)$ which returns:

$$\frac{\partial \rho}{\partial t} + \nabla \cdot (\rho \mathbf{v}) = 0. \tag{2.46}$$

The single fluid motion equation is instead obtained by means of the sum of the two equations for the two species ((2.21) + (2.24)):

$$\rho\left(\frac{\partial \mathbf{v}}{\partial t} + (\mathbf{v}\cdot\nabla)\,\mathbf{v}\right) = \mathbf{j}\times\mathbf{B} - \nabla p - \nabla\cdot\mathbf{\Pi}. \tag{2.47}$$

Typically a simplified version of the viscous stress tensor is assumed in order to avoid the very complicated structure in (2.34); in this way $\mathbf{\Pi} = -\mu\mathbf{W}$, where μ is a single fluid viscosity originated by the contributions of $\mu_0^{e,i}$, $\mu_1^{e,i}$ and $\mu_3^{e,i}$ (namely parallel, perpendicular and gyroviscosity) and it is assumed to be constant. Using the Einstein notation:

$$(\nabla\cdot\mathbf{\Pi})_j = -\mu\,(\nabla\cdot\mathbf{W})_j = -\mu\left(\frac{\partial^2 v_j}{\partial x_i^2} + \frac{1}{3}\frac{\partial^2 v_i}{\partial x_i \partial x_j}\right), \tag{2.48}$$

and, making the additional simplifying hypothesis $\nabla\cdot\mathbf{v} = 0$, the final form of the momentum conservation equation:

$$\rho\left(\frac{\partial \mathbf{v}}{\partial t} + (\mathbf{v}\cdot\nabla)\,\mathbf{v}\right) = \mathbf{j}\times\mathbf{B} - \nabla p + \mu\nabla^2\mathbf{v}. \tag{2.49}$$

Thanks to the combination $m_e(2.24) - m_i(2.21)$ one finds a generalization of the Ohm's law. However, since the exact calculations give rise to a very complex equation, approximations are made in order to keep only the relevant physical terms and to simplify the equation as much as possible. Neglecting terms related to viscosity, the electron mass, assuming a constant current density $\mathbf{j}$ in time and a simplified form of the friction force $\mathbf{F}$, the equation one can get after some steps of algebra is:

$$\mathbf{E} + \mathbf{v}\times\mathbf{B} - \frac{\mathbf{j}}{\sigma} = \frac{1}{en}\left(\mathbf{j}\times\mathbf{B} - \nabla p_e\right), \tag{2.50}$$

that is commonly known as *generalized Ohm's law*. More complete forms of this equation can be found in [18] and [21], where less strict assumptions are made. Anyhow, for the vast majority of physical applications it is common to perform a further simplification by neglecting the right hand side of (2.50), and obtaining:

$$\mathbf{j} = \sigma\left(\mathbf{E} + \mathbf{v}\times\mathbf{B}\right). \tag{2.51}$$

For the scope of this work the development of a single fluid energy equation is not necessary. Anyway, to guarantee the closure of the model, Maxwell's equations are added, remembering that no charge imbalance is contemplated in the model resulting, for example, in the absence of the displacement current term in Faraday's law:

$$\nabla\cdot\mathbf{E} = 0, \qquad \nabla\cdot\mathbf{B} = 0, \qquad \nabla\times\mathbf{E} = -\frac{\partial\mathbf{B}}{\partial t}, \qquad \nabla\times\mathbf{B} = \mu_0\mathbf{j}. \tag{2.52}$$

2.5 Visco-resistive MHD model

Once obtained the single fluid equations, the visco-resistive MHD model is obtained by simply rewriting them with some additional assumptions. In fact, if pressure can be neglected (valid in case of a low β plasma), the mass density ρ is constant in time and uniform in space and the only transport coefficients that determine plasma dynamics are the viscosity μ and the resistivity η, then the model of the plasma fluid consists in the following equations:

$$\rho\left(\frac{\partial \mathbf{v}}{\partial t}+(\mathbf{v}\cdot\nabla)\,\mathbf{v}\right)=\mathbf{j}\times\mathbf{B}+\mu\nabla^2\mathbf{v}, \tag{2.53}$$

$$\frac{\partial \mathbf{B}}{\partial t}=\nabla\times(\mathbf{v}\times\mathbf{B})-\nabla\times(\eta\mathbf{j}), \tag{2.54}$$

$$\nabla\cdot\mathbf{B}=0, \tag{2.55}$$

$$\nabla\times\mathbf{B}=\mu_0\mathbf{j}. \tag{2.56}$$

Before proceeding with further calculations, the physical quantities appearing in the visco-resisitive model are normalized with respect to their typical scale values. This procedure does not really add anything related to the physics of the system but it can help you in understanding which are the mechanisms and the relative terms in the equation that drive the development of plasma dynamics. The normalizations adopted are:

$$\rho=\rho_0\tilde{\rho},\qquad v=v_A\tilde{v},\qquad t=\tau_A\tilde{t},\qquad r=a\tilde{r},\qquad B=B_{0z}(0)\tilde{B}, \tag{2.57}$$

where $\rho_0=m_i n$, v_A and τ_A are the Alfvén velocity and time respectively, that represent the velocity of propagation of hydromagnetic waves and time needed for these waves to travel along an important macroscopic distance. a is the minor radius of the toroidal device and $B_{0z}(0)$ is the on-axis toroidal magnetic field. Thanks to the linearization of MHD equations hydromagnetic waves can be treated, finding that:

$$v_A=\frac{B}{\sqrt{\mu_0\rho_0}},\qquad \tau_A=\frac{a\sqrt{\mu_0\rho_0}}{B}. \tag{2.58}$$

To complete this scheme of normalization, the definition $\gamma=m_i/m_p$ is added. The normalizations in (2.57) also affect the derivatives and the other quantities appearing in the model:

$$\nabla=\frac{\tilde{\nabla}}{a},\qquad \frac{\partial}{\partial t}=\frac{\partial}{\tau_A\partial\tilde{t}},\qquad j=\frac{B_{0z}(0)}{\mu_0 a}\tilde{j}. \tag{2.59}$$

Replacing the normalization scheme (2.57) - (2.59) into the equations of the visco-resistive model (2.53)-(2.56), after basic algebra steps and the removal of the ˜ symbol the visco-resistive model equations become:

$$\frac{\partial \mathbf{v}}{\partial t}+(\mathbf{v}\cdot\nabla)\,\mathbf{v}=\mathbf{j}\times\mathbf{B}+\frac{\mu\tau_A}{a^2\rho_0}\nabla^2\mathbf{v}, \tag{2.60}$$

$$\frac{\partial \mathbf{B}}{\partial t}=\nabla\times(\mathbf{v}\times\mathbf{B})-\nabla\times\left(\frac{\eta\tau_A}{\mu_0 a^2}\mathbf{j}\right), \tag{2.61}$$

$$\nabla\cdot\mathbf{B}=0, \tag{2.62}$$

$$\nabla\times\mathbf{B}=\mathbf{j}, \tag{2.63}$$

in which also the normalization $\rho=1$ is considered since mass density is assumed to be constant. Once equations are written in the form (2.60) - (2.63) , it is quite evident that there are two groupings

of coefficients that contain the unnormalized physical parameters and it is expected that the most important information about the behaviour of the system could be found in them.
In particular, defining resistive and viscous time τ_r and τ_μ as the time scales during which resistive and viscous phenomena take place:

$$\tau_r = \frac{a^2\mu_0}{\eta}, \qquad \tau_\mu = \frac{a^2 n_i \gamma m_p}{\mu}, \tag{2.64}$$

it is possible to introduce two dimensionless fluid numbers that are the viscous Lundquist number M and the Lundquist number S, defined in terms of resistive, viscous and Alfvén times:

$$M := \frac{\tau_\mu}{\tau_A} = \frac{a^2\rho_0}{\mu\tau_A} \qquad S := \frac{\tau_r}{\tau_A} = \frac{a^2\mu_0}{\eta\tau_A}, \tag{2.65}$$

that, once replaced in equations (2.60) - (2.61), return:

$$\frac{\partial \mathbf{v}}{\partial t} + (\mathbf{v}\cdot\nabla)\,\mathbf{v} = \mathbf{j}\times\mathbf{B} + M^{-1}\nabla^2\mathbf{v}, \tag{2.66}$$

$$\frac{\partial \mathbf{B}}{\partial t} = \nabla\times(\mathbf{v}\times\mathbf{B}) - \nabla\times\left(S^{-1}\mathbf{j}\right), \tag{2.67}$$

that, with equations (2.62) and (2.63), constitute the final form of the visco-resistive model.
The implementation of the visco-resitive model has been done in Padova, and the code bears the name SpeCyl [10]. In this thesis a large use of outputs from the code SpeCyl is made.

2.6 Scaling approach to the visco-resistive model

As it is shown in [12], it is more convenient to rewrite them as function of the Prandtl P and Hartmann H numbers, defined as:

$$P := \frac{\tau_r}{\tau_\mu} = \frac{S}{M} = \frac{\mu_0\mu}{\rho_0\eta}, \qquad H := \frac{\sqrt{\tau_r\tau_\mu}}{\tau_A} = \sqrt{SM} = \frac{aB}{\sqrt{\eta\mu}}. \tag{2.68}$$

This final target can be achieved by means of an additional rescaling in time that consequently affects also time derivatives and velocities:

$$t \to \bar{t} = \sqrt{\frac{M}{S}}t, \qquad v \to \bar{v} = \sqrt{\frac{S}{M}}v, \qquad \frac{\partial}{\partial t} \to \frac{\partial}{\partial \bar{t}} = \sqrt{\frac{S}{M}}\frac{\partial}{\partial t}. \tag{2.69}$$

The result of the rescaling is a set of differential equations for the normalized variables:

$$P^{-1}\left(\frac{\partial \mathbf{v}}{\partial t} + (\mathbf{v}\cdot\nabla)\,\mathbf{v}\right) = \mathbf{j}\times\mathbf{B} + H^{-1}\nabla^2\mathbf{v}, \tag{2.70}$$

$$\frac{\partial \mathbf{B}}{\partial t} = \nabla\times(\mathbf{v}\times\mathbf{B}) - \nabla\times\left(H^{-1}\mathbf{j}\right), \tag{2.71}$$

$$\nabla\cdot\mathbf{B} = 0, \qquad \nabla\times\mathbf{B} = \mathbf{j}. \tag{2.72}$$

The great advantage gained introducing the fluid numbers is that by means of them it is possible to describe using the same rescaled equations plasma conditions in which, although the fluid numbers are equal, may differ a lot in terms of plasma physical parameters. In other words the proper values of pressure, density, temperature, magnetic field and so on do not determine directly the evolution of the system, but they affect the latter only by means of dimensionless combinations that are precisely the fluid numbers introduced. This means that if the model is a good description of the real system one can expect to find the Hartmann number to rule most of the phenomena, since the inertial term is often less important near the equilibrium.

2.7 Transport coefficients estimates

The aim of this section is the determination of expressions that allow the evaluation of the transport coefficients introduced in section 2.3 in real experimental conditions in RFX-mod. As a first step, it is necessary to find and expression for the collisional times, since they are involved in many of the coefficients of interest. This achievement is not easy because in an ionized plasma, where a long range (Coulomb) interaction is present, the definition of a collision event is not trivial at all, contrary to what happens in the case of fluids. According to the preferred definition, a collision is a particles encounter that produces a considerable trajectory deflection of at least one of the particles: this implies the momentum exchanged during the collision to be of the same order of the initial momentum of the particles. Thanks to this consideration it is possible to obtain the most important physical dependencies of the collisional time.
In fact, considering a particle with charge e, mass m and thermal velocity v, the distance of closest approach r_0 is easily found, evaluating the momentum exchanged Δp:

$$\Delta p \approx F\Delta t \approx \frac{e^2}{4\pi\epsilon_0 r_0^2}\frac{r_0}{v}, \qquad \Delta p \approx mv, \qquad \rightarrow \qquad r_0 \approx \frac{e^2}{4\pi\epsilon_0 m v^2}. \tag{2.73}$$

The number of collisions per units of time (collisional frequency ν_c) is given counting the number of encounters for a particle traversing a cylinder with radius r_0:

$$\nu_c \approx n\pi r_0^2 v \approx \frac{ne^4}{16\pi\epsilon_0^2 m^2 v^3} \propto \frac{ne^4}{m^{1/2}T^{3/2}}. \tag{2.74}$$

This simple reasoning for evaluating the trend of the collisional time, whose exact formulas can be found carrying out all of the specific calculations:

$$\tau_{ei} = \frac{12\pi^{3/2}\epsilon_0^2 m_e^{1/2} T_e^{3/2}}{2^{1/2} n_i Z^2 e^4 \ln\Lambda}, \qquad \tau_{ii} = \frac{12\pi^{3/2}\epsilon_0^2 m_i^{1/2} T_i^{3/2}}{2^{1/2} n_i Z^4 e^4 \ln\Lambda}, \tag{2.75}$$

where $\ln\Lambda$ represents the Coulomb logarithm, defined as $\ln\Lambda := \ln(r_{max}/r_{min})$, being r_{max} and r_{min} the Debye length and the distance of closest approach during particle collisions at the average velocity. Thanks to this result transport coefficients are easily evaluated replacing formulas (1.8), (2.75) into the results obtained in section 2.3. The great advantage of this approach is the gain of a set of transport coefficients that model a different transport type, depending on the direction considered with respect to the magnetic field.
Using equation (2.31), parallel and perpendicular resistivity are determined:

$$\eta_\parallel = 0.51\frac{m_e}{n_e e^2 \tau_{ei}} = \frac{0.06}{\pi^{3/2}}\frac{m_e^{1/2} e^2}{\epsilon_0^2}\frac{Z\ln\Lambda}{T_e^{3/2}}, \qquad \eta_\perp = \frac{m_e}{n_e e^2 \tau_{ei}} = \frac{0.118}{\pi^{3/2}}\frac{m_e^{1/2} e^2}{\epsilon_0^2}\frac{Z\ln\Lambda}{T_e^{3/2}}. \tag{2.76}$$

About viscosity it is necessary to define, apart from $\mu_\parallel$, the perpendicular $\mu_\perp$ and gyro-viscosity $\mu_\times$, in terms of μ_0, μ_1 and μ_3. This redefinitions are particularly useful because in the construction of the MHD models the assumption $\mathbf{\Pi} \propto \mu \mathbf{W}$ was made.

$$\mu_\parallel^i = 3\mu_0 = 34.6\pi^{3/2}\frac{\epsilon_0^2 m_p^{1/2}}{e^4}\frac{\gamma^{1/2}T_i^{5/2}}{Z^4\ln\Lambda}, \tag{2.77}$$

$$\mu_\perp^i := \mu_1 + 4\mu_1 = \frac{3}{2}\frac{n_i T_i}{\omega_i^2\tau_{ii}} = \frac{1}{8\pi^{3/2}}\frac{m_p^{3/2}e^2}{\epsilon_0^2}\frac{\gamma^{3/2}n_e^2\ln\Lambda}{T_i^{1/2}B^2}, \tag{2.78}$$

$$\mu_\times^i := \frac{1}{2}\mu_3 + 2\mu_3 = \frac{5}{4}\frac{n_i T_i}{\omega_i} = 1.25\frac{m_p}{e}\frac{\gamma n_i T_i}{ZB}. \tag{2.79}$$

In this section only the ion viscosity is considered because it gives the great majority of the contribution to the total viscosity. In fact, it can be seen that each component of the viscosity has a positive scaling with the mass of the species involved and this justifies the dominance of the ions, since the ratio between the two masses (m_e/m_i) is at least of the order 10^{-3}, that makes the approximation in which electrons contribution is neglected reasonable.

2.8 Fluid numbers estimates

In this section, the fluid-dynamical numbers introduced in equations (2.65) and (2.68) are calculated as a function of the plasma parameters that can be experimentally measured. The procedure simply consists in the replacement of the result obtained in the previous section in the definition of the fluid-dynamical numbers. At the end an expression for each fluid number different on the bases of the direction considered with respect to the magnetic field will be obtained.
The results obtained for the viscous Lundquist number are:

$$M_\parallel := \frac{a^2\rho_0}{\mu_\parallel^i\tau_A} = 5.3\times10^{-3}\frac{e^4}{\mu_0^{1/2}\epsilon_0^2}\frac{n_e^{1/2}Z^{7/2}aB\ln\Lambda}{T_i^{5/2}}, \tag{2.80}$$

$$M_\perp := \frac{a^2\rho_0}{\mu_\perp^i\tau_A} = 44.5\frac{\epsilon_0^2}{\mu_0^{1/2}m_p e^2}\frac{aB^3T_i^{1/2}}{\gamma n_e^{3/2}Z^{1/2}\ln\Lambda}, \tag{2.81}$$

$$M_\times := \frac{a^2\rho_0}{\mu_\times^i\tau_A} = 0.8\frac{e}{m_e^{1/2}m_p^{1/2}}\frac{Z^{3/2}aB^2}{\gamma^{1/2}n_e^{1/2}T_i}. \tag{2.82}$$

In the case of Lundquist number only the parallel and the perpendicular one are available (as a consequence of the absence of a cross resistivity):

$$S_\parallel := \frac{a^2\mu_0}{\eta_\parallel\tau_A} = 16.7\pi^{3/2}\frac{\mu_0^{1/2}\epsilon_0^2}{m_p^{1/2}m_e^{1/2}e^2}\frac{aBT_e^{3/2}}{Z^{1/2}\gamma^{1/2}\ln\Lambda n_e^{1/2}}, \tag{2.83}$$

$$S_\perp := \frac{a^2\mu_0}{\eta_\perp\tau_A} = \frac{a^2\mu_0}{1.96\eta_\parallel\tau_A} = 0.51S_\parallel. \tag{2.84}$$

Repeating a similar procedure for the Prandtl number:

$$P_{\parallel} := \frac{\mu_0 \mu_{\parallel}^i}{\rho_0 \eta_{\parallel}} = 576\pi^3 \frac{\epsilon_0^4 \mu_0}{m_p^{1/2} m_e^{1/2} e^6} \frac{T_i^{5/2} T_e^{3/2}}{\gamma^{1/2} Z^4 n_e \left(\ln \Lambda\right)^2}, \tag{2.85}$$

$$P_{\perp} := \frac{\mu_0 \mu_{\perp}^i}{\rho_0 \eta_{\perp}} = 4.08 \frac{\mu_0 m_p^{1/2}}{m_e^{1/2}} \frac{\gamma^{1/2} n_e T_e^{3/2}}{B^2 T_i^{1/2}}, \tag{2.86}$$

$$P_{\perp} := \frac{\mu_0 \mu_{\times}^i}{\rho_0 \eta_{\parallel}} = 20.8\pi^{3/2} \frac{\mu_0 \epsilon_0^2}{m_e^{1/2} e^3} \frac{T_i T_e^{3/2}}{Z^2 \ln \Lambda}. \tag{2.87}$$

And, finally, a similar approach is adopted for the Hartmann number:

$$H_{\parallel} := \frac{aB}{\sqrt{\eta_{\parallel} \mu_{\parallel}^i}} = 0.69 \frac{e}{m_e^{1/4} m_p^{1/4}} \frac{Z^{3/2} a B T_e^{3/4}}{\gamma^{1/4} T_i^{5/4}}, \tag{2.88}$$

$$H_{\perp} := \frac{aB}{\sqrt{\eta_{\perp} \mu_{\perp}^i}} = 45.8 \frac{\epsilon_0^2}{m_e^{1/4} m_p^{3/4} e^2} \frac{a B^2 T_e^{3/4} T_i^{1/4}}{\gamma^{3/4} Z^{1/2} n_e \ln \Lambda}, \tag{2.89}$$

$$H_{\times} := \frac{aB}{\sqrt{\eta_{\parallel} \mu_{\times}^i}} = 8.61 \frac{\epsilon_0}{m_e^{1/4} m_p^{1/2} e^{1/2}} \frac{a B^{3/2} T_e^{3/4}}{Z^{1/2} \gamma^{1/2} n_e^{1/2} T_i^{1/2} \left(\ln \Lambda\right)^{1/2}}. \tag{2.90}$$

The latter results are key formulas for the subsequent development of this work, because, on one side, they allow the evaluation in experimental conditions of the fluid-dynamical numbers that are expected (in particular the Hartmann number) to drive the physics of the RFP configuration plasmas, as it is suggested from the visco-resistive model. On the other side, these quantities are also distinct on the basis of the transport term they model (parallel, perpendicular or cross) and the success of one of them in describing some of plasma physics phenomena (the density limit in the case of this thesis) would suggest the validation of the visco-resistive model and the possibility of inserting those phenomena inside the MHD framework.
In tab. 5.1 the values of the Hartmann number (in particular $H_{\perp}$) are calculated in the case of typical values of RFX-mod operations, for three example shots: the range spanned by $H_{\perp}$ is between 10^5 and 10^8.

Chapter 3

The Reversed-Field Pinch configuration

This chapter is devoted to the presentation of the reversed-field pinch (RFP) configuration. As a first approach, the main aspects of such a configuration are exposed with particular attention on the difference with respect to the tokamak. Secondly, a theoretical approach towards a RFP plasma is developed, following the historical evolution of the RFP interpretation from the '70s up to nowadays: during this path Taylor theory is initially met, followed by more recent achievements in RFP comprehension, based on 3D MHD simulations.
Finally the chapter ends with an introduction to the main features of the RFX-mod device.

3.1 Main features of the RFP configuration

The reversed-field pinch magnetic configuration is experimentally induced in a toroidal plasma, generating a very intense plasma current in the toroidal direction. With respect to the tokamak, toroidal current in the RFP can be even ten times larger (with the same toroidal magnetic field B_ϕ). This difference has important consequences on the magnetic properties of the configuration, since the plasma current is introduced in toroidal devices to generate the rotational transform of the magnetic field.
In fact, in the tokamak, the toroidal magnetic field is typically one order of magnitude larger than the poloidal one. In the case of RFP the toroidal and poloidal components are of comparable amplitude. Indeed, in the outer region of the plasma, the poloidal field is dominant, because the toroidal component decreases as one approaches the plasma edge, and changes sign in the outermost region. This phenomenon, whose explanation is non-trivial, is illustrated in figure 3.1.

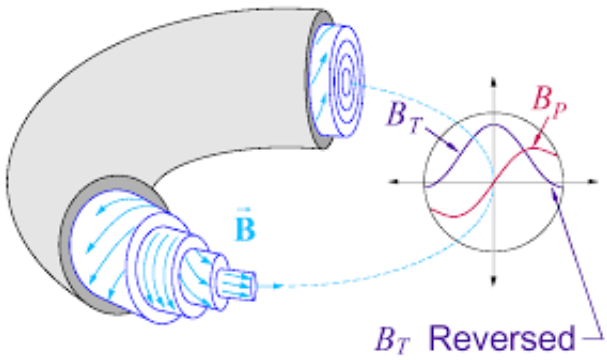

Figure 3.1: Toroidal and poloidal magnetic fields for RFP configuration.

The potential advantages obtained with the RFP configuration for a fusion reactor are: the possibility of avoiding or limiting superconducting coils because the majority of the magnetic field is generated by

the plasma current, and of simplifying the design of the device thanks to the relatively high resistivity (with respect to the tokamak configuration) that could allow the entirely ohmic heating of the plasma without the need of additional heating systems, like neutral beam injection and radio-frequency wave heating.
However, there are also important disadvantages in exploiting the RFP, that are related to confinement. This is pointed out by the fact that the energy confinement time τ_E is at least one order of magnitude lower in the RFP configuration with respect to the tokamak: the latter result can be attributed to the more disordered magnetic topology (characterized by the presence of tearing mode instabilities that generate magnetic islands) that enhance the transport from the central region to the edge, prohibiting optimal heating of the center of the plasma. The two configurations are compared in figure 3.2.

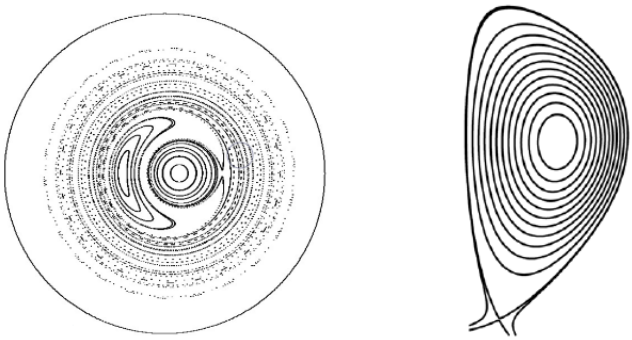

Figure 3.2: Poloidal projection of RFP and tokamak magnetic field lines: while in the RFP configuration magnetic islands and chaos arise, the tokamak displays an ordered magnetic topology.

Despite this, both theoretical and experimental studies show the possibility (which will be discussed further in this chapter) of reaching, under determined conditions, a high level of self-organization, in which the plasma column spontaneously assumes a helical shape (figure 3.3), transport barriers are created and also an improved magnetic topology (similar to the tokamak one) is reached.

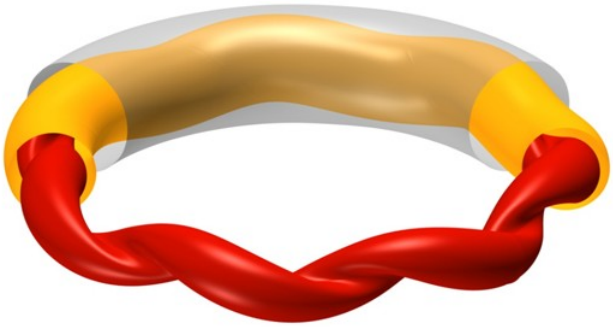

Figure 3.3: Plasma column self-organization in RFP configuration.

As a consequence of it RFP configuration represents an interesting confining method that could be successful, according to the current state of the research, at least for a second generation reactor. There are many experiments devoted to the study of the RFP configuration, generally of smaller size if compared with the largest tokamaks or stellarators. The main are RFX-mod (Reversed-Field eXperiment) located in Padova (Italy), the MST (Madison Symmetric Torus) located in Madison, Wisconsin (USA) [19], and the KTX (Keda Torus eXperiment) in Hefei, China [33].

3.2 Taylor's relaxation theory

The theoretical explanation of the reversed-field pinch has been developed over the last few decades. The first milestone in this field is undoubtedly the Taylor's theory of plasma relaxation that was

enounced for the first time in [51].
To develop it, two requirements (derived by Woltjer in [57]) are essential. These two statements regard a physical quantity related to the magnetic topology, called *magnetic helicity* $\mathcal{H}$ which is defined as:

$$\mathcal{H} := \int \mathbf{A} \cdot \mathbf{B} dV, \tag{3.1}$$

where the integral is calculated over the volume of the magneto-fluid system considered and $\mathbf{A}$ is the vector potential defined by the relation: $\mathbf{B} = \nabla \times \mathbf{A}$. Although the vector potential depends on the choice of the gauge, it can be shown that helicity is gauge invariant, that means it is a good physical quantity. The two Woltjer's theorems are now enunciated:
First Woltjer's theorem. *If a magneto-fluid has zero resistivity ($\eta = 0$), than helicity $\mathcal{H}$ is conserved in time:*

$$\frac{d\mathcal{H}}{dt} = 0. \tag{3.2}$$

Second Woltjer's theorem. *In a system in which the magnetic helicity $\mathcal{H}$ is kept constant, the minimization of the magnetic energy $W = \int B^2/2\mu_0 dV$ is obtained for a force-free field defined by the condition:*

$$\nabla \times \boldsymbol{B} = \mu \boldsymbol{B}, \tag{3.3}$$

with μ constant.

The interested reader can find the proof of the two theorems in the appendix A.1, where the approach of [18] is followed or in the original Woltjer's article [57].
Taylor considered a magneto-fluid with a small departure from perfect conductivity (the effect of the resistivity η is not negligible) in toroidal symmetry. When this system is characterized by a high Θ parameter, a.k.a. "pinch" parameter, defined as the normalized edge poloidal field B_θ:

$$\Theta := \frac{B_\theta(r = a)}{\langle B_\phi \rangle} = \frac{\mu_0 I_p}{2\pi a \langle B_\phi \rangle}. \tag{3.4}$$

Since in Eq. (3.4) I_p represents the plasma current, the initial condition (out of equilibrium) relaxes towards a "quiescent" state that is largely stable.
To analyze the phenomenon from a more quantitative point of view, Taylor made the hypothesis that, although the resistivity is non negligible, the total helicity is conserved, which seems in contradiction with first Woltjer's theorem. Actually, the presence of resistivity implies that each magnetic field line is not frozen inside the fluid flux tube and so the helicity is not anymore constant along each line of force. However, if the departure from the perfect conduction is slight, the global helicity (evaluated on the whole fluid volume) is expected to remain practically constant, because the dissipation, while changing the magnetic topology, does not significantly alter the value of the field. For this reason the effect of the topological change consists merely in a redistribution of the helicity contributions among all magnetic field lines.
Since helicity is conserved, the second Woltjer's theorem can be applied and so one can state that the system will minimize its magnetic energy in the condition of force-free field. This final state results to be a 'quiescent' state because if the minimization of the magnetic energy implies that no magnetic force can act on the magneto-fluid.
To describe this final state of equilibrium (reached after the relaxation) the equation (3.3) is solved in cylindrical geometry with periodic boundary conditions. Using the coordinates r, θ and z all the physical quantities result constant with respect to θ and z because of the symmetry, and the remaining non trivial equation components are:

$$-\frac{dB_z}{dr} = \mu B_\theta, \qquad \frac{1}{r}\frac{d}{dr}(rB_\theta) = \mu B_z. \tag{3.5}$$

If one replaces the first equation in (3.5) in the second one, it is readily obtained:

$$\frac{1}{r}\frac{d}{dr}\left(r\frac{dB_z}{dr}\right) + \mu^2 B_z = 0. \tag{3.6}$$

Multiplying by r^2 one can get:

$$r\frac{d}{dr}\left(r\frac{dB_z}{dr}\right) + \mu^2 r^2 B_z = 0, \tag{3.7}$$

which is a Bessel equation in terms of $z = \mu r$ and $\nu = 0$ and therefore:

$$B_z = B_0 J_0(\mu r), \tag{3.8}$$

with B_0 magnetic field on axis. Since $J_1 = -\frac{dJ_0}{dr}$, from (3.5) one can readily obtain:

$$B_\theta = B_0 J_1(\mu r). \tag{3.9}$$

Equations (3.5) are solved by the lowest order Bessel functions ($J_0(\mu r)$, $J_1(\mu r)$) that are combinations of sine and cosine with modulated amplitude (figure 3.4).

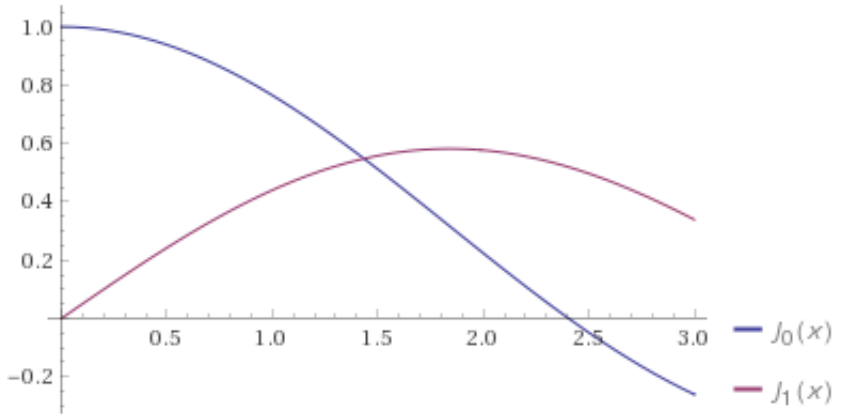

Figure 3.4: Equilibrium current and fields in the Bessel Function Model (BFM).

The resulting model is called Bessel Function Model (BFM) and it is still routinely used, in a slightly modified version, for calculating the equilibrium fields, in the RFX-mod device, [38].
Bessel functions are largely able to reproduce the behaviour of the magnetic field and, in particular, the reversal of the toroidal magnetic field in the external region. The first experimental measurements seemed to confirm the BFM predictions, especially those coming from the experiment ZETA, one of the first to work in the RFP configuration, [40]. An experimental comparison can be made with measurements of the magnetic field profile and introducing the parameter F, defined as:

$$F := \frac{B_\phi(r = a)}{\langle B_\phi \rangle}, \tag{3.10}$$

that represents the edge toroidal magnetic field normalized to its average. The condition that data should satisfy (in order to confirm Taylor's relaxation theory) is the following:

$$\frac{F}{\Theta} = \frac{B_\phi(a)}{B_\theta(a)} = \frac{J_0(\mu a)}{J_1(\mu a)}. \tag{3.11}$$

The plot of F as a function of Θ is shown in figure 3.5 with the comparison with experimental data. It is worth noting that, in the BFM, reversal of the toroidal field happens when the pinch parameters $\Theta > 1.2$.

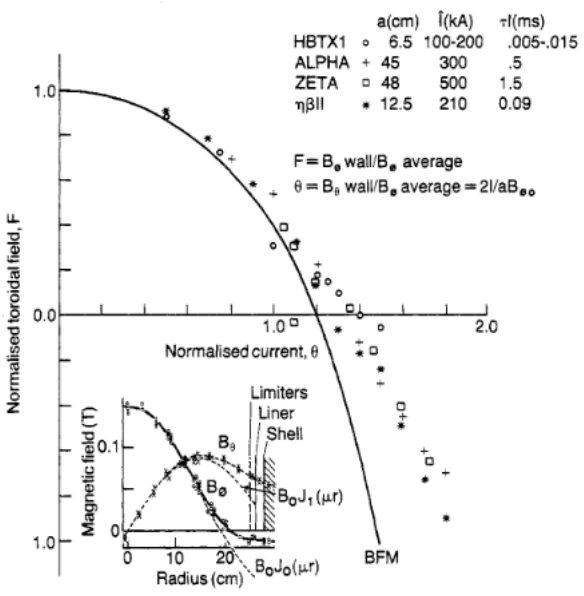

Figure 3.5: Comparison between Taylor's prediction and experimental data in the (Θ, F) plane. Figure adapted from Ref. [6].

In this picture, although Taylor's theory predicts quite well the trend shown by the data, there is still something missing, since quantitative agreement is not perfect especially at large Θ values (bottom right corner of Fig. 3.5). Allowing for a variation of μ along the radius (the so called "μ & p" model, [38]), helps in fitting data better, although for a more accurate description of the relaxation mechanism it is necessary to use a more modern MHD approach through numerical simulations.

3.3 Magnetic order and high level self-organization

Understanding of the RFP configuration has greatly improved since 1990s thanks to numerical simulations and to the growing experimental activity in this field.
In particular, thanks to the high computational power it is possible to predict many features of the reversed-field pinch by numerically simulating MHD models in particular conditions and with the right hypotheses to study the case. A detailed summary regarding the evolution of RFP configuration during the years is found in [11], that is broadly followed in the contents of this section.

3.3.1 Wire model

The wire model consists in a really simplified representation ('toy model') of the reversed-field pinch. The initial configuration considered (figure 3.6 (a)) has a cylindrical symmetry and is composed by an external ideal shell that guarantees, thanks to a uniform azimuthal current I_{shell}, the presence of an axial magnetic flux $\Phi(\mathbf{B})$ and by an axial wire, in which the current I is flowing. It is easily shown that this system is a magnetic flux conservator because, for the Faraday law:

$$-\frac{d\Phi(\mathbf{B})}{dt} = \mathcal{E} = R\Delta I = 0, \tag{3.12}$$

where $\mathcal{E}$ is the induced electromotive force on the shell and R is the resistance of the ideal shell, that clearly amounts to zero implying the rate of change of the magnetic flux to be zero.
Imaging for simplicity the development of a kink helical perturbation on the wire (figure 3.6 (b)): this perturbation can bring the wire current to flow parallel with respect to the shell one or anti-parallel with respect to it. Since parallel currents attract, this type of perturbation is enhanced, while the other is reduced. Considering, at this point, a perturbation of the 'parallel' type this will be increased and will generate an additional magnetic field $\mathbf{B}'$ that is parallel to the original one. To compensate the increase of magnetic field flux it is necessary to have a decrease or even a sign inversion of the magnetic field in the edge region not interested by the wire perturbation (figure 3.6 (c)).

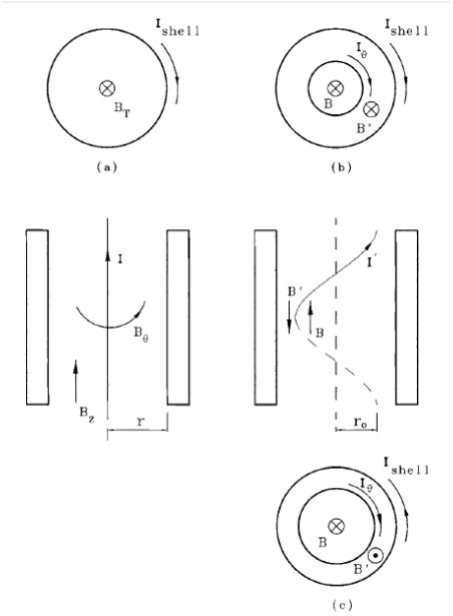

Figure 3.6: Graphic representation of the wire model, picture taken from 3.6.

3.3.2 Magneto-fluid model

The upgrade of the previous model towards a magnetohydrodynamic level can be done only by means of numerical simulations of the differential equations involved. Limited to the reversed-field pinch configuration the visco-resistive model solution is of particular interest.
Solving 3D nonlinear MHD equations with an initial perturbation gives rise to qualitatively different solutions, on the basis of the composition of the spectrum of active plasma instabilities (more details about the Fourier spectrum will be given in the next chapter, especially devoted to numerical solutions of the MHD model). In fact, there are cases in which there is no clear dominant mode in the Fourier spectrum. They are defined as turbulent or multiple helicity (MH) regime. In others, instead, the plasma can reach, after a phase transition, an entirely different state, characterized by the total dominance of one Fourier mode over all the others. This regime is defined as laminar or single helicity (SH). Also an intermediate situation exists featured by the presence of a dominant mode end other modes whose contribution is smaller but not negligible with respect to the dominant one: this regime is defined as quasi single helicity (QSH).
The different phases are not only predicted by solving the equations, but they have consequences that are verified during the experiment in the geometry of the plasma self-organization (see figure 3.7) and in the magnetic topology (see figure 3.8).

An evident difference in the magnetic field configurations is present among the different regimes: in particular the transition towards the laminar regime is featured with a strong reduction of the magnetic

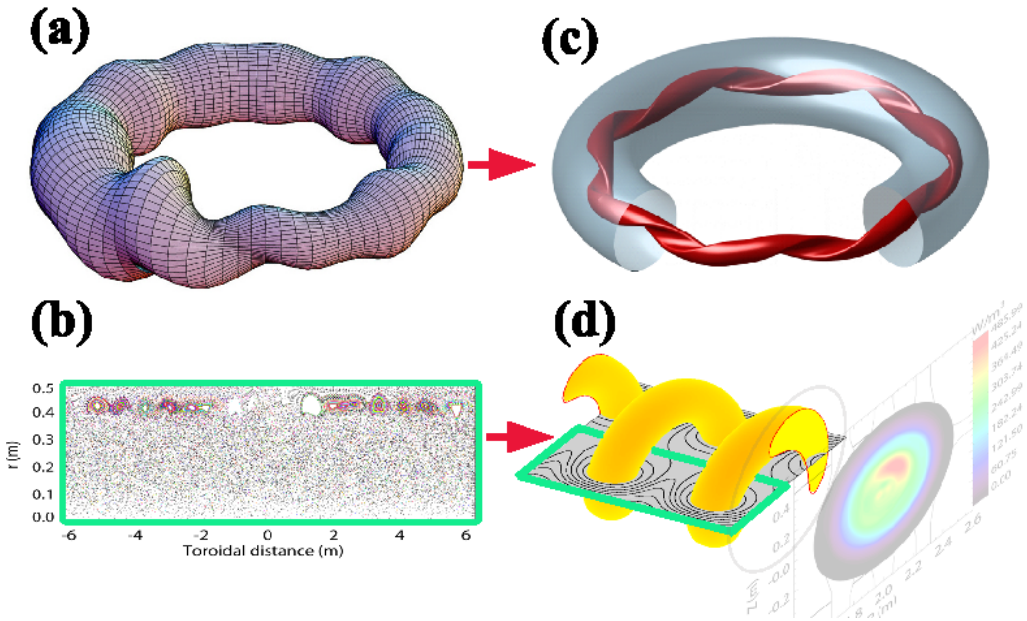

Figure 3.7: Bifurcation dominating RFP plasmas: (a) - (b) is the MH state, while (c) - (d) is the QSH helical state. (a) and (c) are reconstructions of the plasma shape, while (b) and (d) show the inner magnetic topology, taken from [45].

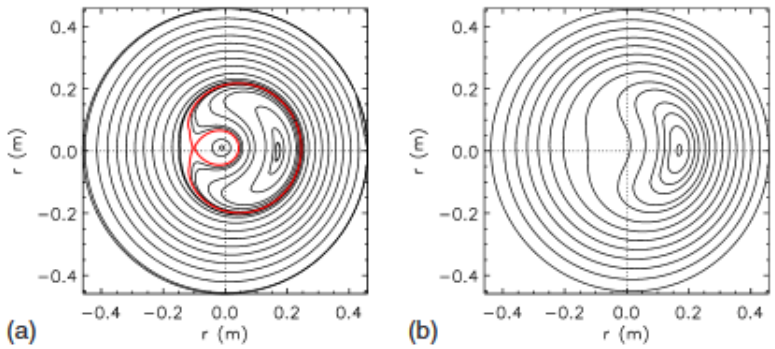

Figure 3.8: Magnetic topology reconstructed comparison in RFX-mod: QSH (a) and SH (b) regimes.

chaos (see frames (b) and (d) in Fig. 3.7), that consists in the disappearance of the magnetic islands and in the formation of an ordered geometry that entails benefits also for transport, allowing the formation of a hot plasma helical core, [35].
Thanks to the achievement of the QSH regime, RFP configuration can display interesting properties about confinement that could in principle be used for a future fusion reactor. The main difficulty for this purpose is achievement and the maintenance of the single helicity that can be obtained in plasmas with an Hartmann number above a determined threshold or stimulating it with particular external perturbations called seed magnetic perturbations (these problems are addressed in the next chapter). Anyhow, the existence of a spontaneous QSH regime shows that RFP can be described as a self-organized helical state that displays magnetic order.

3.4 The RFX-mod device

As anticipated in the first chapter, in Padova there is a magnetic confinement fusion experiment that can work as aflexible device both in tokamak and RFP configurations (more details can be found in Ref. [39]). The name of this device is RFX-mod (see Ref. [44]) and, since this work is aimed at the study of phenomena in the case of reversed-field pinch, only the properties in the RFP configuration are analyzed. In particular the main features of the experiment are reported in Table 3.1.

Table 3.1: RFX-mod device properties in RFP configuration.

Major radius, R_0	2.0 m
Minor radius, a	0.459 m
Plasma current, I_p	≤ 2.0 MA
Toroidal field, B_ϕ	≤ 0.7 T
Flat top time, Δt	$\simeq 250$ ms

As already pointed out, the research in the case of RFP is not yet developed at the level of the largest tokamaks or stellarators, nevertheless RFX-mod is the largest RFP in operation and results obtained in RFX proved to be of great interest in the fusion community. The machine, that is now facing a shut down to allow the completion of its second upgrade RFX-mod2 (whose details are referred in Ref. [36]), is shown in its working phase in figure 3.9.

The toroidal device is composed by the toroidal vacuum vessel (aimed to contain the plasma), magnetic systems for producing plasma equilibrium and control, power supplies and diagnostics that surround the machine (figure 3.9).
The internal wall that directly faces the plasma is composed by 2016 trapezoidal graphite tiles, only 1.8 cm thick (to maximize the plasma volume): the composition is chosen in order to sustain high thermal loads and to get low Z impurities. The vacuum vessel that allows reaching low pressures is composed by 72 wedge shaped elements that are sustained by the external mechanical structure.
The magnetic system is composed by 3 windings: the toroidal field coils (TF, 48 coils) for producing B_ϕ, the poloidal field coils (M, 20 coils) for inducing the plasma current I_p and associated B_θ field, and the vertical field coils ("field shaping" F, 16 coils), carefully described in Ref. [48]. The main aim of the latter system is to control, thanks to the generation of magnetic field, the shape and position of the plasma.
But the flagship of the experiment RFX-mod is a system of 192 saddle coils dedicated to plasma active control (figure 3.10).

These coils are both in poloidal and toroidal direction (like a saddle) but are used to generate a radial magnetic field of the order of some mT that can compensate the one generated by helical perturbations. To optimize the control, each coil has an independent control and power supply.
The control system is one of the modification introduced in the upgrade of the 2000, described in Ref. [44]. Presently, an upgrade is in program aimed at removing the vacuum vessel, so that the

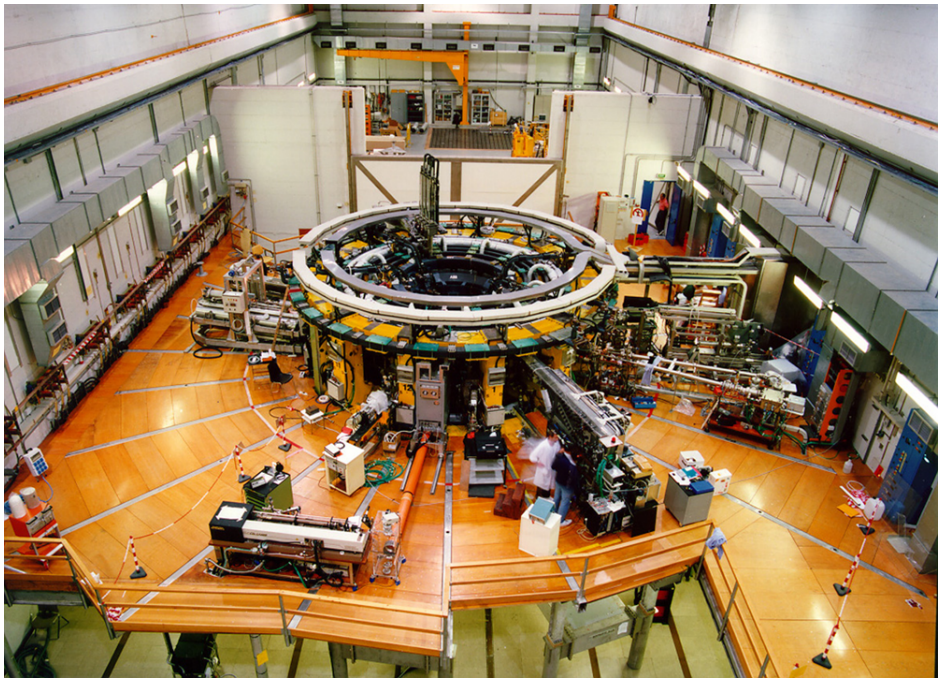

Figure 3.9: the RFX-mod device.

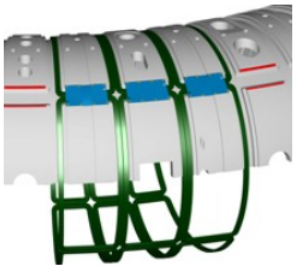

Figure 3.10: Representation of RFX-mod active control saddle coils.

plasma should be contained by the chamber that up to now had the role of mechanical structure. This would allow the increase of the minor plasma radius and the generation of a more ideal boundary condition for the plasma. Operations are expected to resume by the end of 2020, as foreseen in [36]. The diagnostic apparatus is described, limited to the measurements that are of interest for this work in chapter 5, the one devoted to the analysis of the data coming from RFX-mod.

Chapter 4

SpeCyl numerical simulations

This chapter is devoted to the presentation of the results obtained with SpeCyl numerical simulations. First of all, the code used is introduced, briefly describing the solving procedure of the visco-resistive model equations. Secondly, the most important results achieved in the past years using the SpeCyl code are summarized, showing a good agreement between simulations results and experimental measurements. Then, the simulations database considered and the results highlighted are shown, paying particular attention to the analysis of magnetic energy and edge magnetic field and to the role of the Hartmann number in determining the trend of the latter quantities.
Finally, after having selected the simulations with more realistic initial conditions among those available in the dataset, the scaling of the edge radial magnetic field with the Hartmann number is presented, which will be the result to be compared with experimental data in Chapter 5.

4.1 The Specyl code

The Specyl code is a numerical tool that performs 3D nonlinear magnetohydrodynamics simulations. The code was introduced for the first time in [10] to study magnetic reconnection phenomena in the RFP configuration, using properly a MHD approach.
The code carries out the solution of the equations of the visco-resistive model in the form containing the viscous Lundquist M and Lundquist S numbers shown in Section 2.5, that here are rewritten for the sake of completeness:

$$\frac{\partial \mathbf{v}}{\partial t} + (\mathbf{v} \cdot \nabla)\, \mathbf{v} = \mathbf{j} \times \mathbf{B} + M^{-1} \nabla^2 \mathbf{v}, \tag{4.1}$$

$$\frac{\partial \mathbf{B}}{\partial t} = \nabla \times (\mathbf{v} \times \mathbf{B}) - \nabla \times \left(S^{-1} \mathbf{j}\right). \tag{4.2}$$

$$\nabla \cdot \mathbf{B} = 0, \tag{4.3}$$

$$\nabla \times \mathbf{B} = \mathbf{j}. \tag{4.4}$$

Obviously to obtain the latter equations it is necessary to make some hypotheses that are, in addition to the usual of the one fluid MHD, the presence of a negligible pressure, constant mass density and viscosity and resistivity as effective transport coefficients. These hypotheses and the relative validity regime have already been discussed with the scaling that can bring to equations (4.1) - (4.4) in Section 2.5.
As it frequently happens in physics, the set of equations can be treated more easily in the Fourier

space: exploiting the cylindrical symmetry (of the $\theta \in [0, 2\pi]$ and $z \in [0, 2\pi R_0]$ coordinates) with periodic boundary conditions the main physical quantities can be rewritten as Fourier series. Naming m and n the poloidal and toroidal wave numbers, a generic function $f(r, \theta, z, t)$ of the space and time coordinates can be rewritten as:

$$f(r, \theta, z, t) = \sum_{m=-\infty}^{+\infty} \sum_{n=-\infty}^{+\infty} f_{m,n}(r, t)\, e^{i\left(m\theta + \frac{n}{R_0} z\right)}, \tag{4.5}$$

in which the toroidal angle ϕ is replaced by the expression z/R_0, with R_0 major radius of the rectified torus. To guarantee the function f to be real, a condition on its transform $f_{m,n}$ the following conditions has to be required:

$$f \in \mathbb{R} \quad \longrightarrow \quad f^*_{m,n} = f_{-m,-n}. \tag{4.6}$$

Although from the mathematical point of view all the modes take part to the generation of f, from the experimental one only the lowest order modes give a non negligible contribution.
The role of the Fourier modes is also fundamental in order to determined the regime to which the plasma is found. In the numerical simulation only a finite number of Fourier modes is taken into account. Those considered by the SpeCyl code, chosen after a convergence study described in [10], are shown in figure 4.1.

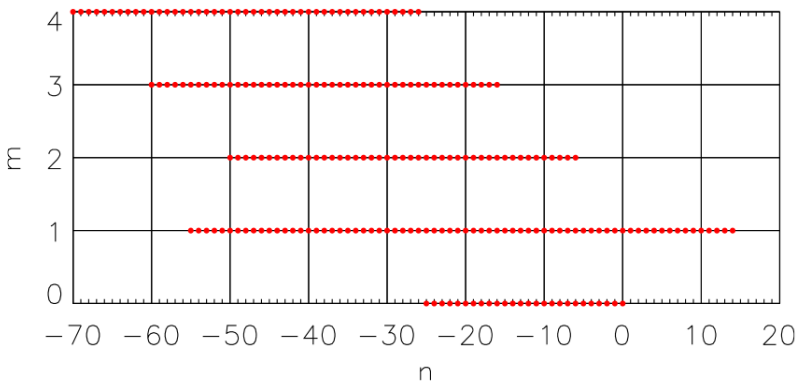

Figure 4.1: Fourier modes considered by the SpeCyl code (red dots), from [7].

Working in the Fourier space greatly simplifies the solution of differential equations because derivatives and integrals are transformed into linear algebra operations. Linear differential equations are transformed in algebraic equations that involve the same mode (the same m and n numbers) of different physical quantities in the Fourier space. Instead, non linearity is translated into convolution of different Fourier modes. An exemplification of the last statement can be found in the section A.2 of the Appendix.
From the point of view of transport the SpeCyl code takes into account only the coefficients of resistivity and viscosity (as it happens for the visco-resistive model). They are expressed in a normalized form as the inverse of the Lundquist number $\eta = S^{-1}$ and of the viscous Lundquist number $\nu = M^{-1}$. These coefficients depend, in principle, on time and space. The dependencies chosen in SpeCyl are simplified in order to allow the simulation to be made in a reasonable time and also because direct measurement of the viscosity profile are not available. The coefficients assumed are a constant and uniform viscosity and a constant resistivity in time. The only non trivial dependence is the radial one of the resistivity:

$$\nu(r) = \nu_0, \qquad \eta(r) = \eta_0 \left(1 + A \left(\frac{r}{a}\right)^B\right), \qquad A = 20, \qquad B = 10. \tag{4.7}$$

The profile of the resistivity is chosen considering the typical polynomial profiles of the temperature as function of the cylinder radius and the relations between resistivity and temperature. The choice of these dependencies is absolutely non trivial, and the verification of the validity of this assumption is one of the aim of this work.
The initial condition imposed to solve the differential equations can be of two types: ideal shell or magnetic perturbation. The ideal shell boundary conditions consist in the absence of radial magnetic field and of poloidal electric field at the boundary:

$$B^r_{m,n}(a) = 0, \qquad E^\theta_{m,n}(a) = 0, \qquad \forall m, n. \tag{4.8}$$

Additional conditions are the presence of a constant toroidal electric field ($E_z = E_0$) to induce the plasma current and the no slip condition for two velocity components: $v_\theta(a) = 0$, $v_z(a) = 0$. Instead, magnetic perturbations (MPs) are obtained imposing the presence of a Fourier mode for the radial magnetic field different from zero at the boundary. This type of simulations is particularly interesting for the RFP configuration because they can induce the transition to SH or QSH, as it will be explained in the next chapter.
Another code available for fusion plasmas numerical simulations is PIXIE3D. The code solves a more complicated set of differential equations because it takes into account the energy balance besides the visco-resistive model, solved with a finite volume element method.
In [7] a non-linear verification of the two codes is carried out with excellent results, in terms of agreement between SpeCyl and PIXIE3D simulation predictions. The latter result represents a key point in favour of the use of the two codes in numerical simulating fusion plasmas.

4.2 RFP and 3D MHD simulations

Since the 90s the SpeCyl code has been used to perform 3D non linear magnetohydrodynamics simulations that turned out to be of fundamental importance in understanding the RFP configuration, reproducing or predicting experimental results coming from RFX and RFX-mod devices. In this section, the main achievements in this research field are exposed, pointing out the aspects that can be useful for this work.
The role played by the Hartmann number emerged from the first results of numerical simulations. In [12], the equations (4.1) - (4.4) are rewritten introducing properly the Hartmann and the Prandtl numbers, as done in Chapter 2, obtaining the set of equations (2.70) - (2.72), from which it is evident that the Hartmann number becomes the main plasma parameter when the inertia terms are negligible. Then, results of MHD numerical simulations are presented with $H \approx 10^2 - 10^4$ (figure 4.2).

These simulations were made exploring a wide range of the initial parameters, compatibly with the computational power available in those years. In figure 4.2 the time averaged magnetic energy (in normalized units) associated with the $m = 0$ modes as function of the Hartmann number is plotted. Simulations properties considered are summarized in table 4.1.

Table 4.1: Types of simulations analyzed.

Symbol	Simulation settings
$\triangle$	$S = 3.3 \times 10^3$, $P \in \left[\frac{2}{3}, 10\right]$
$\blacktriangledown$	$S = 3.0 \times 10^4$, $P \in [1, 5000]$
$\circ$	Slightly perturbed SH initial condition

The results found in 4.2 are: the independence on the Prandtl number and the presence of a phase transition between $H = 2000$ and $H = 3000$ that is pointed out by the discontinuity in the the value of the $m = 0$ magnetic energy. At low Hartmann values the magnetic energy related to the $m = 0$ modes is reduced of some orders of magnitude. Other analyzes show that in these cases the energy

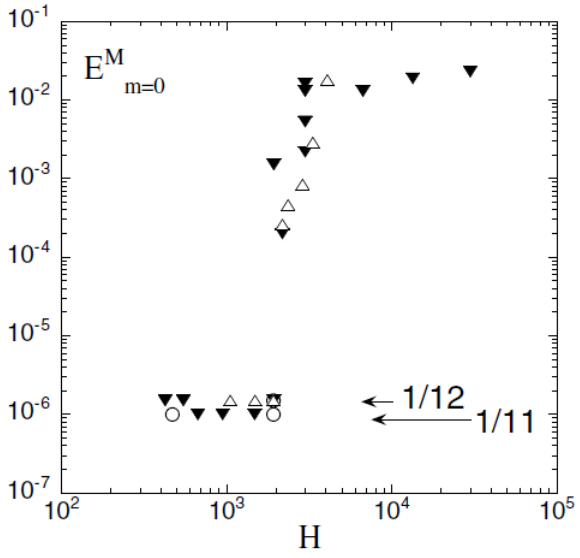

Figure 4.2: Magnetic energy of the $m = 0$ modes: a phase transition appears around $H = 2500$, from [12].

associated to the modes with $m/n = 1/11$ or $m/n = 1/12$ is incredibly increased.
The threshold $H \approx 2500$ "separates" the domain into two different regions in which the plasma is found into two different phases: SH below the Hartmann threshold value (in which the modes $m/n = 1/11$ and $m/n = 1/12$ dominate) and MH above the threshold value. The Hartmann number is thus a fundamental parameter to understand the transition from SH to MH.
In more recent times the modeling activity has been aimed at understanding the role of initial conditions. In particular, in [8], simulations with seed magnetic perturbations (MPs) are presented: a radial magnetic field of a determined mode (typically the usual dominant mode $m = 1$, $n = -7$) of a relative magnitude of 2% with respect to the edge magnetic field is introduced as initial perturbation. These values are also the typical one that are involved in the experiment, as it happens in RFX-mod device.
An important analogy between SpeCyl numerical simulations and the RFX-mod experiment is shown in [8]: a QSH phase can be stimulated by means of an adequate initial boundary condition of the radial magnetic field.

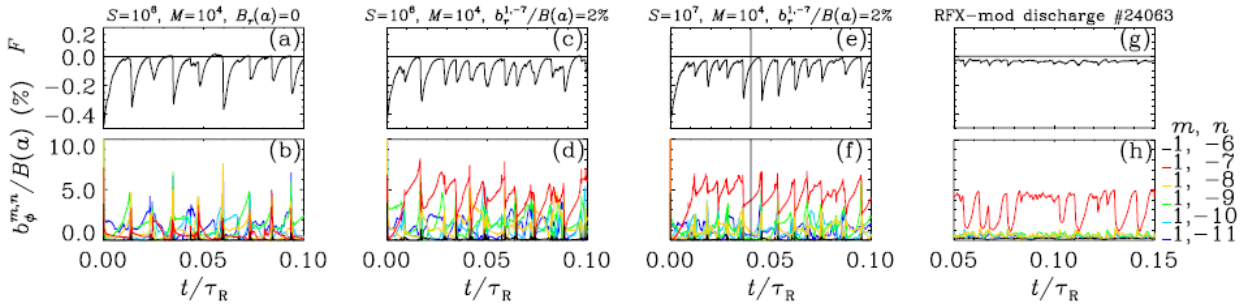

Figure 4.3: Comparison between three different simulations and an RFX-mod shot for the F factor and the toroidal magnetic field, from [8].

More precisely, in figure 4.3, quasi-periodic cycles in QSH phase are repeated: they are characterized by the dominance of a Fourier mode of the magnetic field followed by a sudden crash in which the system returns in MH phase. This behaviour is shown for simulations with $H \approx 10^5$, and for RFX-mod # 24063 shot with $I_p \simeq 1.5\,\mathrm{MA}$, $n_e \simeq 2.8 \times 10^{19}\,\mathrm{m}^{-3}$ and $T_e \simeq 750\,\mathrm{eV}$.
The agreement between SpeCyl numerical simulations and RFX-mod experiments finds a further confirmation in [53]. In this article visco-resistive MHD results predicted experimental measurements, in the case of seed magnetic perturbation application, possible thanks to the active-feedback control

system with which RFX-mod device is equipped. The result is shown in Figure 4.4, in which one can see that stimulating a certain mode by means of a magnetic perturbation it is possible to produce a helical state in which the considered mode is the dominant one: this behaviour is directly observed in the experiment and it is reproduced by numerical simulations.

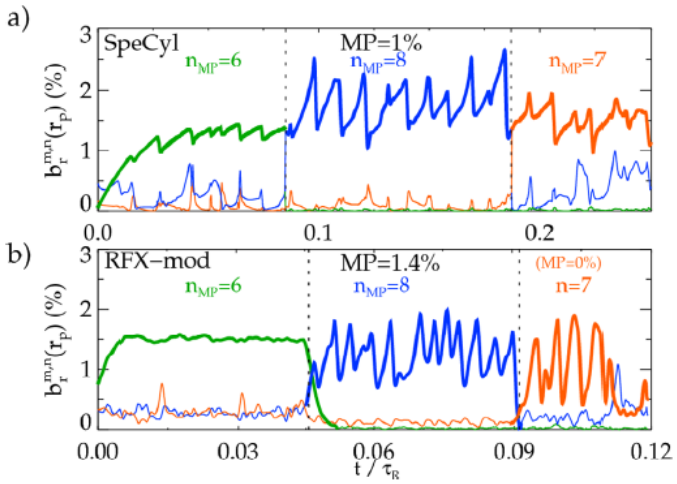

Figure 4.4: Comparison between a Specyl simulation (a) and an RFX-mod shot (b) with the same seed magnetic perturbation for the radial magnetic field, from [53].

The success obtained by the SpeCyl code in modelling the RFP physics justifies the use of the code and its future developments and it reveals the visco-resistive model to be the best theoretical framework available up to now for the purposes of this work.

4.3 Simulations database analysis

In this work, a database composed by 94 numerical simulations made for previous studies (like those cited in the previous section) are considered. The initial inputs for the central viscosity ν_0 and the central resistivity η_0 are chosen in order to cover a range for the Hartmann number as wide as possible that spans an interval of about four orders of magnitude between 10^2 and 10^6.
The region with higher Hartmann numbers (approximately between 5×10^5 and 10^8) is the one of major interest from the experimental point of view but it is very difficult to explore by means of numerical simulations because of computational reasons. In fact, according to equations (2.70) and (2.71), where terms proportional to H^{-1} appear, the introduction of a high Hartmann number implies the coexistence (inside the same differential equation) of terms of order 0 and at least one term of order H^{-1} that causes a great increase in the computational time needed, due to the difference in the magnitude of the two terms.
The geometry used by the SpeCyl code is cylindrical with periodic boundary conditions, fixing the aspect ratio, i.e. $R_0/a = 4$, the value of RFX-mod device.
In the database, different types of simulations are contained with respect to the initial magnetic perturbations (MPs) that in the experiment are induced by means of the active control saddle coils: there are some of them without the initial magnetic perturbations (**MP off**) and others endowed with the initial magnetic perturbation, that is obtained imposing a non zero radial magnetic field at the radial position $r = a$ for a determined Fourier mode at the initial time (**MP on**). The modes stimulated in this second case are those that typically dominate the spectrum in the SH or QSH phases in RFX-mod device: $m = 1$, $n = -5, -6, -7, -8, -9, -10, -11, -12$. In particular the most frequent stimulated mode is the one with $m = 1$, $n = -7$, because it was experimentally shown that the latter plays a fundamental role in RFX-mod QSH phase, although the mechanism by which this particular mode dominates is not entirely understood. The intensity of the perturbation is usually expressed in terms of the perturbation normalized to the edge magnetic field ($B(a)$): the values considered in the

simulations are 1.3%, 2%, 4%, 6% . The most reliable values (applied in the experiments) are between 2% and 4%. All the simulations in this database are characterized by ideal (zero resistivity) boundary conditions .
The output of the simulations are three component of the magnetic field (radial, poloidal and toroidal) and the magnetic energy, obtained integrating, over the plasma volume, B^2. Each component of the magnetic field is found as a four dimensional array that has as entries a time coordinate, a radial coordinate, a coordinate to indicate the Fourier mode, and one to specify if the modulus or the phase is taken into account. The magnetic energy is expressed as a two dimensional array with a radial coordinate and a coordinate that indicates the Fourier mode.
Since a great majority of the discharges simulations are characterized by periodic intervals of single mode dominance (QSH) separated by sudden crashes of magnetic chaos (MH), it is reasonable to calculate time averages only in the QSH phase time. To reach this goal, the spectral index N_s is defined as:

$$N_s = \left[\sum_{n=-N_1}^{-1} \left(\frac{B_{1,n}^2}{\sum_{j=-N_1}^{-1} B_{1,j}^2} \right)^2 \right]^{-1}, \tag{4.9}$$

where N_1 is the maximum n (in modulus) among the $m = 1$ modes taken into account by the code, and $B_{1,n}$ is a generic harmonic of the magnetic field. The spectral index N_s was introduced for the first time in Ref. [27]. A value of $N_s = 1$ implies the plasma to be in a pure SH. A threshold N_{th} for N_s below which the system is considered to be in QSH is usually chosen and, consequently, the time average is computed only for the instants during which the spectral index is below the threshold chosen. The choice of this threshold value clearly results to be arbitrary and, from now on, the time average below the threshold value will be indicated by the symbol $\langle\rangle_{t|N_s(t)<N_{th}}$.

To analyze the simulations database an IDL routine for the analysis was written to calculate a series of useful physical quantities for the analysis:

- Prandtl number P and Hartmann number H, defined in terms of central ν_0 and central resistivity η_0

$$P = \frac{\nu_0}{\eta_0}, \qquad H = \frac{1}{\sqrt{\eta_0 \nu_0}}. \tag{4.10}$$

- The spectral index as function of time $N_s(t)$.
- Edge magnetic field related to the dominant and the secondaries modes, both for the cases $m = 0$ and $m = 1$ and for each of the three components radial B^r, poloidal B^θ and toroidal B^z:

$$\left\langle B_{0,dom}^r (r = 0.95a) \right\rangle_{t|N_s(t)<N_{th}}, \qquad \left\langle B_{0,dom}^{\theta,z} (r = a) \right\rangle_{t|N_s(t)<N_{th}}, \tag{4.11}$$

$$\left\langle B_{0,sec}^r (r = 0.95a) \right\rangle_{t|N_s(t)<N_{th}}, \qquad \left\langle B_{0,sec}^{\theta,z} (r = a) \right\rangle_{t|N_s(t)<N_{th}}, \tag{4.12}$$

$$\left\langle B_{1,dom}^r (r = 0.95a) \right\rangle_{t|N_s(t)<N_{th}}, \qquad \left\langle B_{1,dom}^{\theta,z} (r = a) \right\rangle_{t|N_s(t)<N_{th}}, \tag{4.13}$$

$$\left\langle B_{1,sec}^r (r = 0.95a) \right\rangle_{t|N_s(t)<N_{th}}, \qquad \left\langle B_{1,sec}^{\theta,z} (r = a) \right\rangle_{t|N_s(t)<N_{th}}. \tag{4.14}$$

  It is necessary to point out some details about calculations in formulas (4.11) - (4.14). The edge radial magnetic fields are evaluated at the radial position $r = 0.95a$ because, since zero resistivity boundary condition is assumed, the evaluation of the radial field at $r = a$ simply amounts to 0

and so its calculation is not of particular physical interest. To calculate the secondary modes contributions the following formula is applied (here written in the case of $m = 1$ modes):

$$B^i_{1,sec} = \sqrt{\sum_{\substack{j=-N_1,\\ j\neq n_{dom}}}^{-1} \left(B^i_{1,j}\right)^2}, \tag{4.15}$$

where i can be r, θ, z. The dominant mode is calculated at each time step and, in principle, it can be different from time to time.

- The time averaged magnetic energy related to the dominant and secondary modes both for the case $m = 0$ and $m = 1$:

$$\left\langle W^M_{0,dom}\right\rangle_{t|N_s(t)<N_{th}}, \qquad \left\langle W^M_{0,sec}\right\rangle_{t|N_s(t)<N_{th}}, \tag{4.16}$$

$$\left\langle W^M_{1,dom}\right\rangle_{t|N_s(t)<N_{th}}, \qquad \left\langle W^M_{1,sec}\right\rangle_{t|N_s(t)<N_{th}}. \tag{4.17}$$

  In this case the energy of the secondary modes is found, simply summing all the secondary modes:

$$W^M_{1,sec} = \sum_{\substack{j=-N_1,\\ j\neq n_{dom}}}^{-1} W^M_{1,j}, \tag{4.18}$$

  because, in the case of energy, all the contributions are positive.

- The Fourier mode $m = 0$, $n = -1$ edge magnetic field, that has an important correspondence with the ratio n/n_G, that describes the density limit:

$$\left\langle B^r_{0,1}\left(r = 0.95a\right)\right\rangle_{t|N_s(t)<N_{th}}, \qquad \left\langle B^{\theta,z}_{0,1}\left(r = a\right)\right\rangle_{t|N_s(t)<N_{th}}. \tag{4.19}$$

The calculation of all the previous quantities is repeated for all the simulations in the database and are all dimensionless (because they undergo to a normalization).

4.4 Simulations results: magnetic energy

In this section the results found about the magnetic energy are presented. The interest is addressed to find clear trends in the behaviour of the magnetic energy and the role that Hartmann number plays in determining them. In the results presented, it will be evident that the latter parameter is an order parameter that rules phase transitions of the magnetic energy. To analyze the differences between the simulations, they are divided on the basis of the initial perturbations (mode stimulated and relative intensity).

4.4.1 $m = 1$ modes

The first part of the analysis regards the $m = 1$ modes magnetic energy. In this case the simulations are divided into two different sets: the ones with no external magnetic perturbations (MP off) and those with the presence of the latter (MP on). For the second set an additional selection is made: only one stimulated mode is chosen, that is the $m = 1$, $n = -7$ mode. This is the mode with the higher number of simulations available and it is the most probable to be stimulated also in the

experimental conditions, then only the simulations with relative perturbation intensity in the range $2\%-4\%$ are considered (that is the more realistic initial condition). The results, in absence of magnetic perturbations, are shown in figure 4.5:

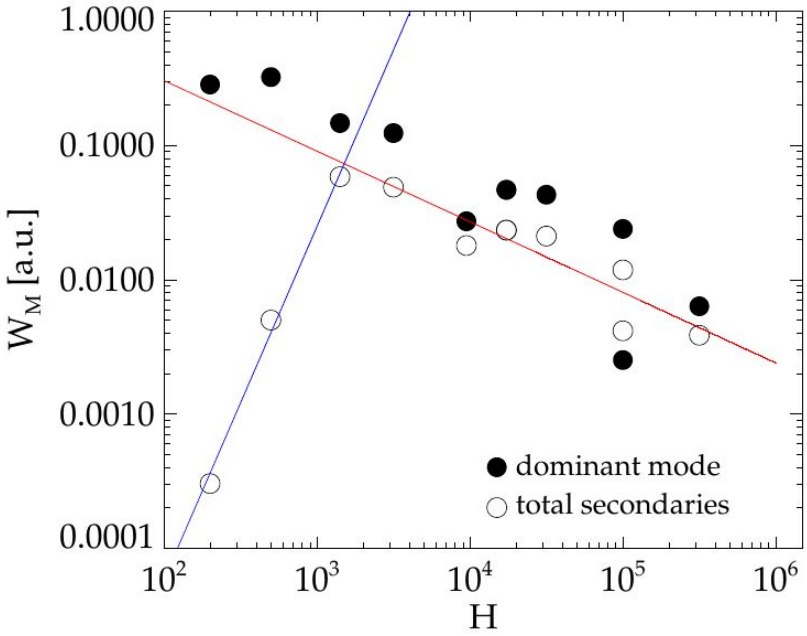

Figure 4.5: Magnetic energy of the $m = 1$ modes with no magnetic perturbation (MP off) as function of the Hartmann number.

As it can be seen, the dominant mode shows a trend (for the magnetic energy) with a slightly negative slope along all the interval of the Hartmann number considered. The situation related to the secondary modes is different: in particular a clear change in the behaviour of their magnetic energy (as function of H) can be seen around $H \approx 10^3$ - 2×10^3. Below the threshold the magnetic energy of the secondary modes is orders of magnitude smaller than the one related to the dominant mode and displays a positive slope. At the threshold value the energy related to the dominant and the secondary modes are comparable and for values of Hartmann beyond the threshold they approximately show the same behaviour. The precise slopes that can be found via a fitting procedure are:

$$W^M_{1,sec} \propto H^{2.7\pm0.2} \qquad H \leq 2 \times 10^3, \tag{4.20}$$

$$W^M_{1,sec} \propto H^{-0.5\pm0.1} \qquad H > 2 \times 10^3. \tag{4.21}$$

The Hartmann number turns out to be an order parameter that rules a phase transition between a regime of SH (below $H \approx 2 \times 10^3$), where to the dominant mode the great majority of the magnetic energy is associated, and a regime of MH (for $H > 2 \times 10^3$), where the dominant mode is just the one with the higher energy but doesn't assume a dominating part of the magnetic energy. This role of H has already been shown in Figure 4.2 in the case of $m = 0$ modes magnetic energy.
In Figure 4.6 the case with the presence of an $m = 1$, $n = -7$ mode initial perturbation for the radial component of the edge magnetic field is instead shown.

Also with the active stimulation, the critical value of $H \approx 2 \times 10^3$ is a separating threshold between different behaviours of the magnetic energy. While below the threshold no significant differences (between dominant and secondary modes) are found, above it, the dominant mode displays an approximately constant trend and the secondary modes display a negative slope for the magnetic energy, until the latter reaches values that are orders of magnitude smaller with respect to the dominant ones. The fitting procedure returns, in this region:

$$W^M_{1,sec} \propto H^{-0.63\pm0.05} \qquad H > 2 \times 10^3, \tag{4.22}$$

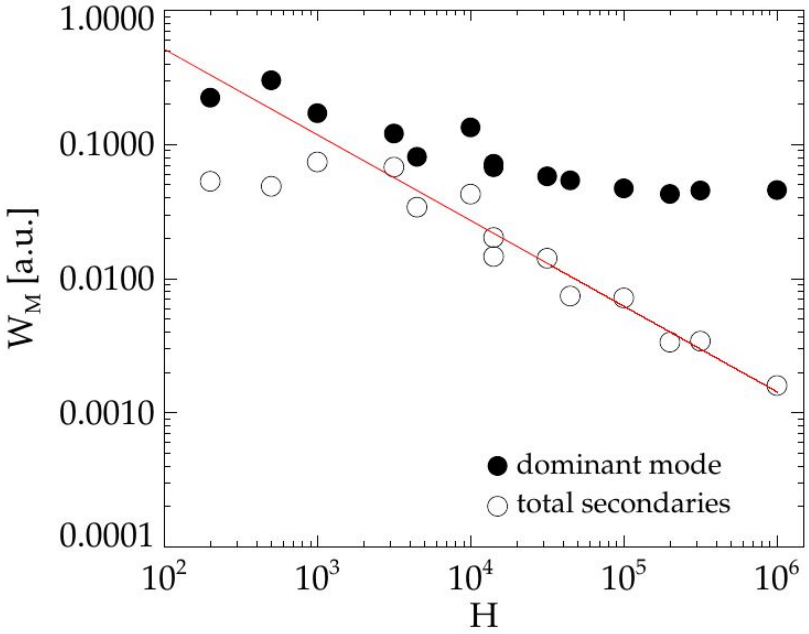

Figure 4.6: Magnetic energy of the $m = 1$ mode with magnetic perturbation (MP on) stimulating the $m = 1$ $n = -7$ mode as function of the Hartmann number.

the resulting negative slope of the secondary modes is fundamental to allow the rise of the QSH state, as seen in experiment [34] .

4.4.2 $m = 0$ modes

The most interesting properties of the magnetic energy related to the $m = 0$ modes, can be pointed out comparing their behaviour in presence and in absence of the external magnetic perturbation. In this case all the $m = 0$ modes are considered without distinguishing between the dominant one and the secondary modes. The result found with these prescriptions is shown in figure 4.7.

The figure confirms that, as for the plots about the $m = 1$ modes, the Hartmann number rules the trend of the magnetic energy. When the external magnetic perturbation is switched on, the magnetic energy trend is almost flat. If, instead, the perturbation is switched off, a change in the trend is evident around the usual critical value of $H \approx 2 \times 10^3$. In fact, below the threshold, the magnetic energy of the non stimulated simulations is smaller than in the case of those stimulated and it displays a positive slope till it reaches, in correspondence of the Hartmann critical value, the maximum value, beyond the latter no qualitative difference is found adding an external magnetic perturbation. Also for the $m = 0$ modes the fit is calculated in the case of active magnetic perturbation, obtaining:

$$W^M_{0,sec} \propto H^{2.7\pm0.6} \qquad H \leq 3 \times 10^3, \tag{4.23}$$

$$W^M_{0,sec} \propto H^{-0.57\pm0.08} \qquad H > 3 \times 10^3. \tag{4.24}$$

Concluding this section, one can remark that, in the context of the visco-resistive model numerical simulations, the Hartmann number reveals to be an order parameter governing transitions between SH and MH phases and generating different distribution of the magnetic energy among the most important Fourier modes. On the other side, it is evident that the magnetic energy behaviour is clearly influenced by the introduction of external magnetic perturbations, which becomes a powerful instrument to modify the development of a discharge, at a given value of the Hartmann number.

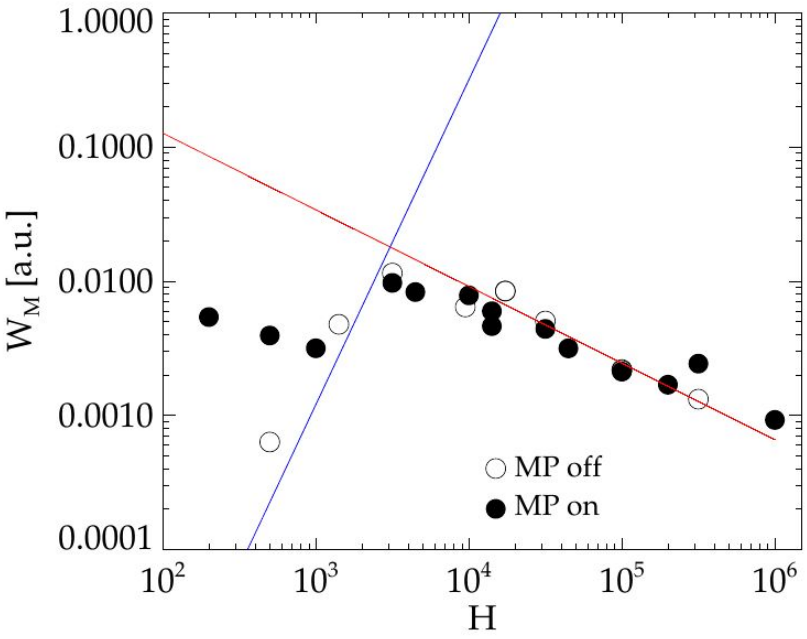

Figure 4.7: Magnetic energy of the $m = 0$ modes, comparing the presence of the external stimulation (MP on) and its absence (MP off).

4.5 Simulation results: edge magnetic field

In this section the simulations results regarding the edge magnetic fields are analyzed: in particular, the focus will be the Fourier mode $m = 0$, $n = -1$ that is predicted to be the best candidate in describing the density limit: more details about this statement will be given in the next Chapter. Anyhow, it will be shown that the results found for the $m = 0$, $n = -1$ mode are qualitatively similar to the ones obtained in the case of the $m = 0$ dominant mode.
The starting point of the analysis is found in figures 4.8, 4.9 and 4.10, where the three components of the edge magnetic field (normalized to the toroidal field on axis B_0) are plot as function of the Hartmann number for all the simulations of the database analyzed.

The results present a situation similar to the one found for the magnetic energy. As it can be seen in figures 4.8 - 4.10, all the components of the edge magnetic field undergo an important change of their behaviour, once reached a threshold value of the Hartmann number. Anyhow, the threshold value is greater that the once found for the previous case and it is of the order of magnitude $H \approx 10^4$. The trend is positive for the $m = 0$ $n = -1$ mode for Hartmann smaller than the critical value, the sign of the slope changes for an Hartmann value beyond the threshold. A result that is qualitatively similar but quantitative different (for the plasma magnetic energy and the edge magnetic field) appears reasonable, if one takes into account that the global magnetic energy is influenced by the values of the edge magnetic field but depends also on the field evaluated on the whole plasma volume.
The change in the slope of the $m = 0$ Fourier modes is not limited to the mode with $n = -1$ but it can be found also analyzing the the field $B^r_{0,dom}(r = 0.95a)$ (see figure 4.11).

Although interesting properties are found by analyzing the whole simulation database, to perform more precise predictions a selection should be done, in order to analyze only those ones that reproduce conditions as near as possible to the experiment, similarly to what done in the case of the magnetic energy.
The simulations are selected into two groups depending on the external magnetic perturbation:

- MP off: simulations in the absence of the external magnetic field,
- MP on: simulation with the mode $m = 1$, $n = -7$ stimulated, with a relative intensity in the

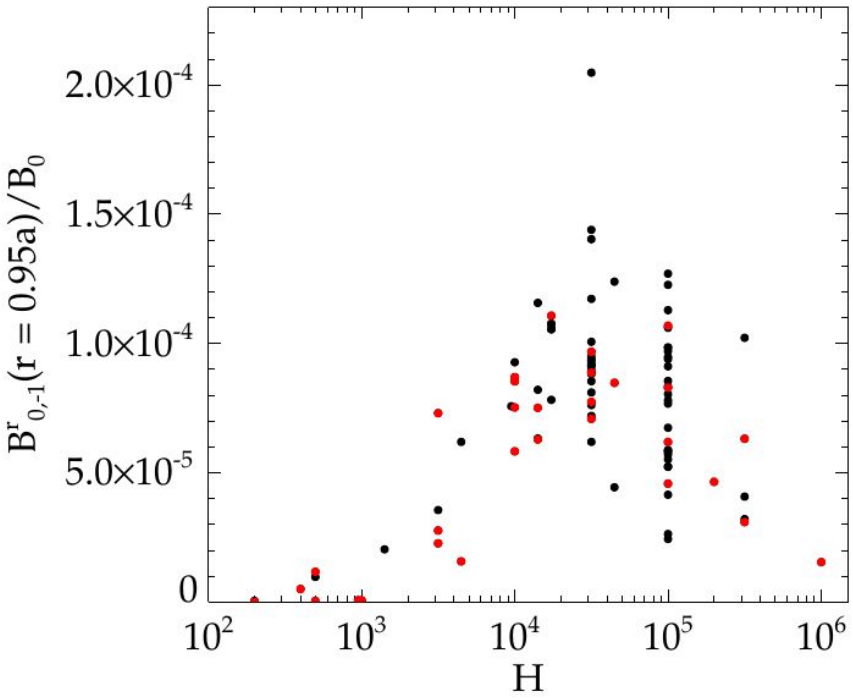

Figure 4.8: Edge radial magnetic field as function of the Hartmann number. The red dots represent simulations with $m = 1$, $n = -7$ stimulation in the range of intensity $2\% - 4\%$.

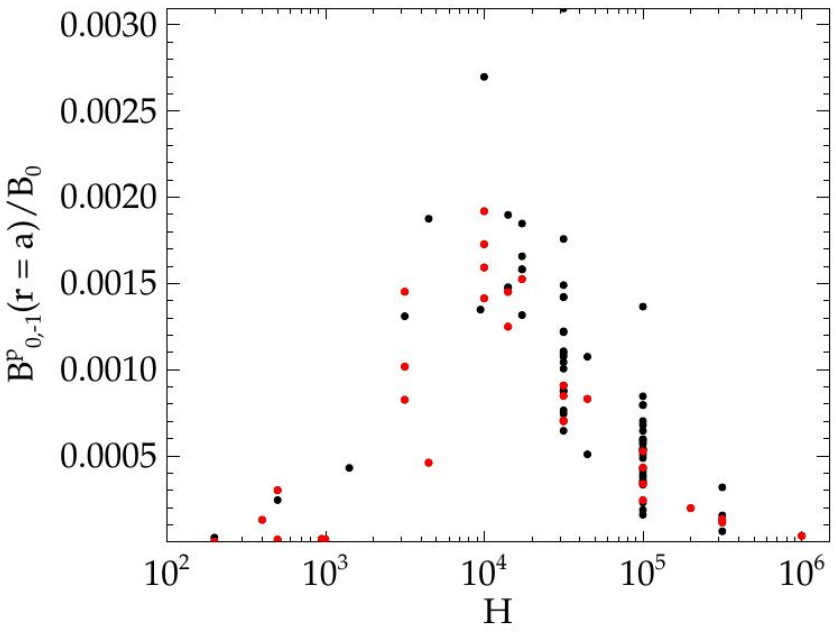

Figure 4.9: Edge poloidal magnetic field as function of the Hartmann number. The red dots represent simulations with $m = 1$, $n = -7$ stimulation in the range of intensity $2\% - 4\%$.

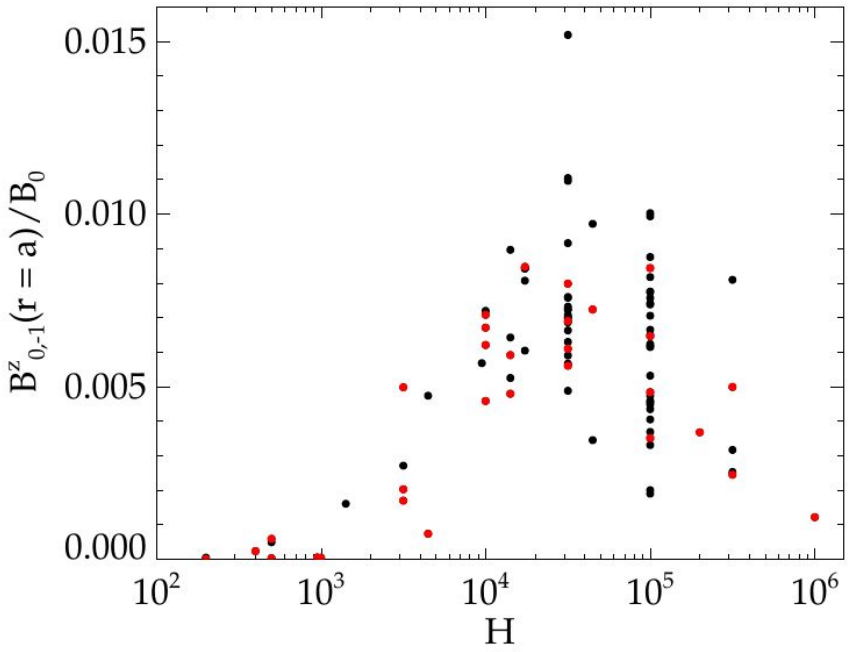

Figure 4.10: Edge toroidal magnetic field as function of the Hartmann number. The red dots represent simulations with $m = 1$, $n = -7$ stimulation in the range of intensity $2\% - 4\%$.

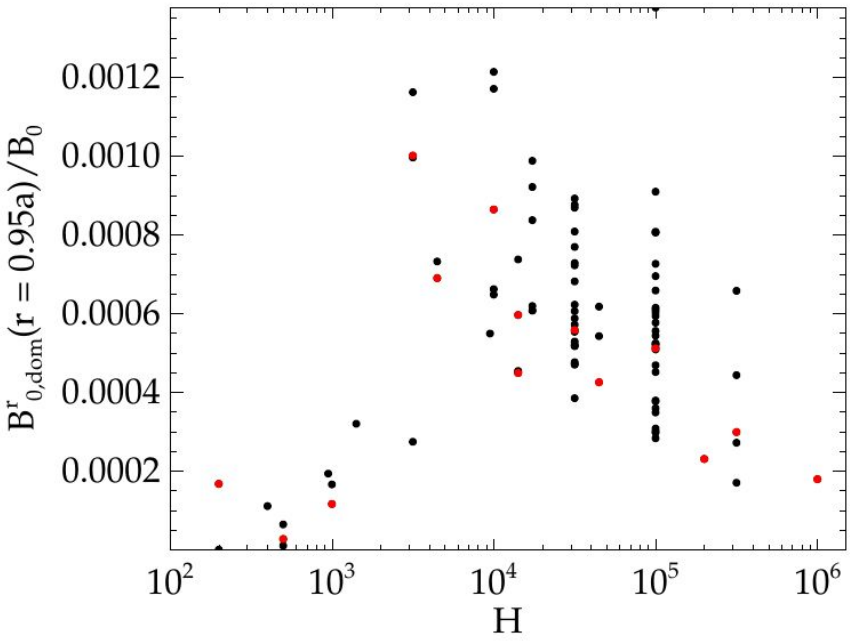

Figure 4.11: Edge magnetic field related to $m = 0$ dominant mode, as function of the Hartmann number. The red dots represent simulations with $m = 1$, $n = -7$ stimulation in the range of intensity $2\% - 4\%$.

range 2 - 4 %.

Once the selection is made, it is still evident the presence of a change in the slope of the edge radial magnetic field around a value of $H \approx 10^4$. In the region with a negative slope a fit procedure can be made, in preparation for the comparison with experimental data, where the Hartmann number H is beyond 10^5. The results are calculated for the edge radial magnetic field both for the case of the mode $m = 0$, $n = -1$ and of the dominant $m = 0$ mode (shown in figures 4.12 - 4.13).

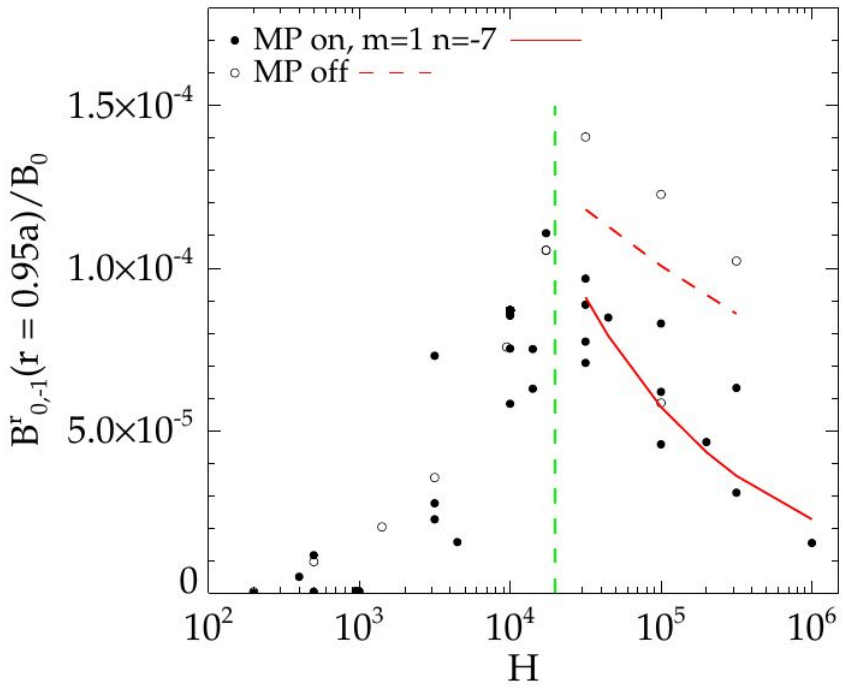

Figure 4.12: Edge radial magnetic field (related to the $m = 0$, $n = -1$ mode) as function of the Hartmann number. Fit procedure performed for Hartmann values beyond the green line.

The scaling laws found are the following:

- For the mode $m = 0$, $n = -1$:

$$B^r_{0,-1}(r = 0.95a) \propto H^{-0.14\pm0.27}, \quad \text{(MP off)} \tag{4.25}$$

$$B^r_{0,-1}(r = 0.95a) \propto H^{-0.40\pm0.07}, \quad \text{(MP on)} \tag{4.26}$$

- For the dominant $m = 0$ mode:

$$B^r_{0,dom}(r = 0.95a) \propto H^{-0.13\pm0.40}, \quad \text{(MP off)} \tag{4.27}$$

$$B^r_{0,dom}(r = 0.95a) \propto H^{-0.28\pm0.03}, \quad \text{(MP on).} \tag{4.28}$$

The fit results are the basis for the comparison with the experimental data which will be shown in Chapter 5, but looking at the high values of the errors only the case with active stimulation should be considered.

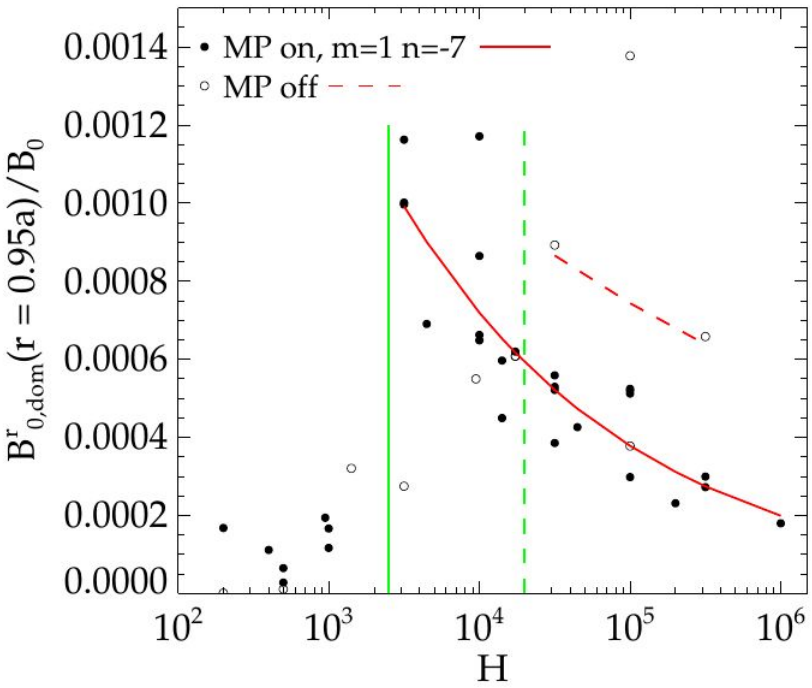

Figure 4.13: Edge radial magnetic field (related to the $m = 0$ dominant mode) as function of the Hartmann number. Fit procedure performed for Hartmann values beyond the green lines.

Chapter 5

RFX-mod shot analysis

In this chapter experimental data coming from the RFX-mod device are analyzed, with the goal of finding new scaling laws for the density limit, relating it to the Hartmann number and to edge magnetic field.
The data analyzed in this work were not collected purposely for the present Thesis, but they were used in several, previous studies on QSH, confinement scalings and the density limit: these studies are summarized in the first Section of this chapter. After that, a description of the databases is made, followed by the description of the procedure adopted to evaluate the Hartmann number for RFX-mod RFP plasmas. Then, the results obtained are introduced, referring to Hartmann scalings and the $m = 0$, $n = -1$ mode analysis. The procedure adopted for this final analysis is based on the Newcomb method, which is briefly introduced.
The final section is devoted to a first comparison between numerical simulations and experimental data.

5.1 Previous experimental studies

The experimental data used in this work, carefully introduced in the next section, were collected and analyzed for previous studies that constitute the basis on which this work is developed. In particular, three different paths of research, to which they belong, can be identified:

- **Scaling studies**, in which relations that link different measurable parameters are found using a fit procedure and evaluating the correlation among the variables involved.
- Study of the **edge plasma physics in QSH phase**, since it will be shown that edge radial magnetic field plays a key role in describing the ratio n/n_G.
- Study of the **density limit**, in which physical laws able to predict the behaviour of the ratio n/n_G are found.
- Study of the **confinement properties and transport barriers during the QSH**.

5.1.1 Scaling studies on RFX

The first scaling of interest for this work presented in 2000 [52], in which a wide database of shots was considered, including standard shots, QSH shots and shots with particular initial condition to improve the confinement, in the old RFX machine. The most important result derived was a scaling law that involved the Lundquist number S (evaluated by means of RFX diagnostics) and the measurements of the normalized toroidal magnetic field fluctuations ($b_\phi/B_\theta(a)$). The result was confirmed by a comparison with SpeCyl numerical simulations, that display a similar scaling. The latter are shown in figures 5.1 and 5.2.

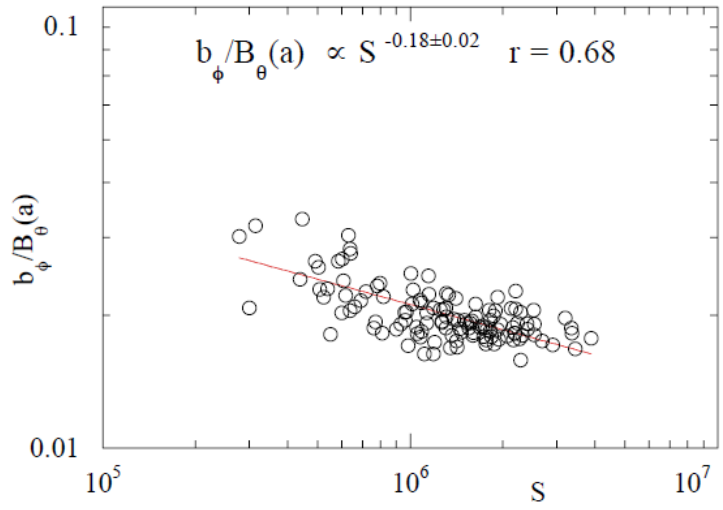

Figure 5.1: Normalized toroidal field fluctuations, as function of the Lundquist number S (RFX-mod experimental data), from [52]).

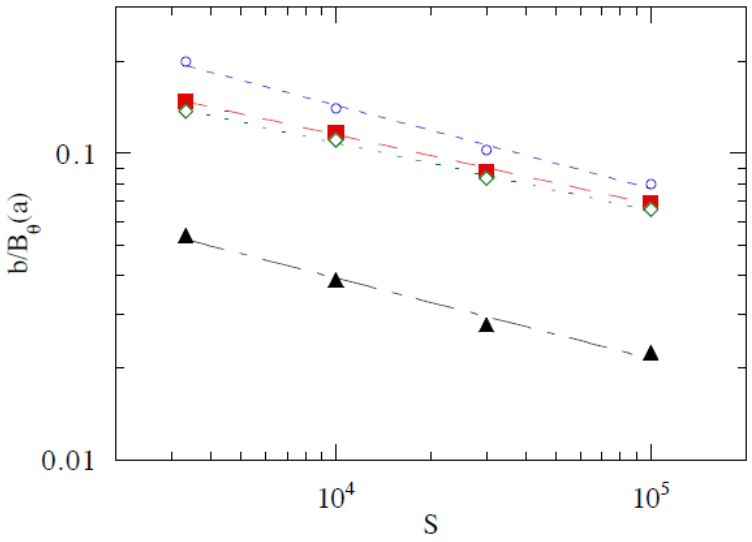

Figure 5.2: Normalized magnetic field fluctuations, as function of the Lundquist number S (SpeCyl numerical simulations), from [52]): different component of the magnetic fluctuations are analyzed: ○ for $b^r(a/2)$, ■ for $b^{tot}(a)$, ◇ for $b^z(a)$, ▲ for $b^\theta(a)$.

As it can be seen, although the ranges of S analyzed do not correspond, the agreement of the two scaling laws is quite good, as it is the correlation coefficient. The agreement, resulting from the fit procedure, regards also the absolute values of the magnetic perturbations and not only the scaling laws.
Other scaling laws for the magnetic perturbations were introduced in [52] involving the Prandtl number P or a multiple regression with plasma current I_p, electric temperature T_e, density n and the effective charge Z_{eff}. However in that work, the results did not significantly improve the previous one in terms of correlation value, partly because of a slight error in the evaluation of the experimental value of Prandtl. For this reason, at that time, the Lundquist number S turns out to be a good parameter that described the magnetic field perturbations, coherently with other works in the same years on MST [49]. The results presented in [52] are anyway only partly correct, since from Chapter 4 we know that visco-resistive simulations predict a better scaling with $H = \sqrt{SM}$.
Another scaling study of particular interest was presented in Ref. [28], which is a more recent paper where other useful scaling laws are presented. The wide database considered contains RFX-mod shots with $0.2\,\mathrm{MA} < I_p < 1.6\,\mathrm{MA}$, $-0.045 < q(a) < 0$ and $0.1 < n/n_G < 1$, in which, to improve statistics each point of the Thomson scattering measurement for the central electron temperature (regularly repeated every 25 ms) during the flat top phase of the discharge is considered.
Working on these data, different relations are discovered via a multi-parametric fit procedure of electron temperature T_e, poloidal beta β_p and energy confinement time τ_E as function of plasma current I_p, central density n, and edge radial field $B^r(a)$. Among these laws one of particular interest links electron temperature and plasma current, as it is shown in figure 5.3:

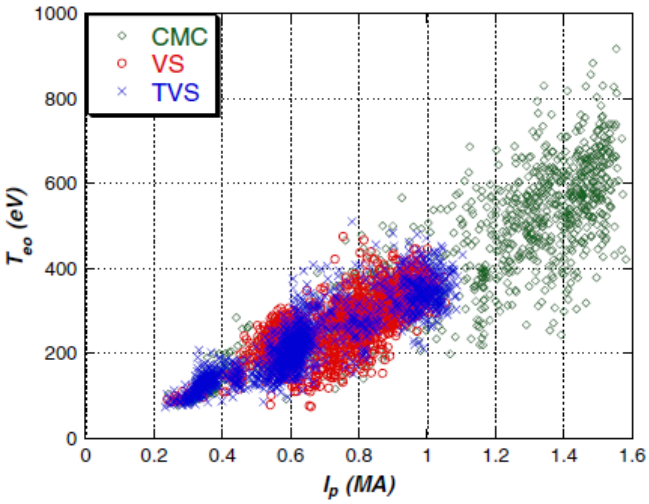

Figure 5.3: Plot of the the central electron temperature T_{e0} as function of plasma current I_p, for all the discharges considered in [28].

The relation exactly obtained is, for the sake of completeness:

$$T_e(r=0) \propto I_p^{1.09\pm0.01} \langle n_e \rangle^{-0.30\pm0.01} \left(b^{\phi}_{sec}(r=a) \right)^{-0.28\pm0.01} . \tag{5.1}$$

Considering the approximated relation $I_p \propto T_e$, a result is found which turns out to be interesting for the purposes of this work:

$$\frac{n}{n_G} = \frac{n\pi a^2}{I_p} \propto \frac{n}{T_e} \propto \frac{1}{H_\perp}, \tag{5.2}$$

that suggests to investigate scaling laws as a function of the perpendicular Hartmann number.

5.1.2 Study of the edge plasma physics in QSH

The QSH phase is of particular interest for the RFP confinement and this is the reason why it is studied in many different works. The more recent among these articles is [43], where the role of the $m = 1$ secondary modes is discussed with particular interest to plasma wall interactions (PWI).
In RFX-mod the usual dominant mode is the one with $m = 1$, $n = -7$, the secondary modes considered are the $m = 1$, $-23 \leq n \leq -8$ modes. A displacement $\Delta_{m,n}$ is defined in terms of perturbed radial magnetic fields $b^r_{m,n}$, $\Delta_{1,sec}$ is obtained summing the secondary modes considered.
The ratio $\Delta_{1,sec}/\Delta_{1,-7}$ is proved to be an estimator of the strength of plasma wall interactions: the radiating power is higher in the case of chaotic MH phase with respect to the well ordered SH phase. To prove this, a comparison with SpeCyl numerical simulations and a prediction for the future RFX-mod2 experiment are made, envisaging a lower plasma wall interaction for the future experiment.
Finally, one can state that this type of studies are useful to understand the role of the edge magnetic turbulence in the development of plasma discharges, also in the tokamak configurations.

5.1.3 Previous studies of the density limit

In recent years many articles have been published aimed at better understanding the density limit in the RFP configuration, using as a starting point the Greenwald limit that was initially formulated for the tokamak devices (see Section 1.4 and in particular Figure 1.8).
In Ref. [41] it is pointed out that the density limit in the case of RFP configuration does not cause a disruption, but instead critical phenomena that bring, anyhow, to the discharge termination. In fact, increasing the density limit up to $n/n_G \gtrsim 0.35$, the ordered plasma phases (QSH) are lost, while at values $n/n_G \approx 1$ localized edge particles accumulations are found, implying an increasing edge irradiated power, causing the overall temperature decrease and the consequent increase of the resistivity with deleterious effect on plasma current and loop voltage. The final stage is that, at extremely high resistivity and loop voltages, the energy stored in the poloidal field winding (M-coils) is wasted and the discharge terminates. The experimental fact that $V_{loop} \propto n/n_G$ is also shown in figure 1.8.
In Ref. [47] the role of the $m = 0$ modes in determining the density limit is observed: in particular, analyzing different RFX-mod shots for plasma current I_p and F parameter defined by equation (3.10), the contribution of the $m = 0$, $-6 \leq n \leq -1$ modes to the perturbation magnetic field is shown to considerably increase at $n/n_G \gtrsim 0.35$ (figure 5.4).

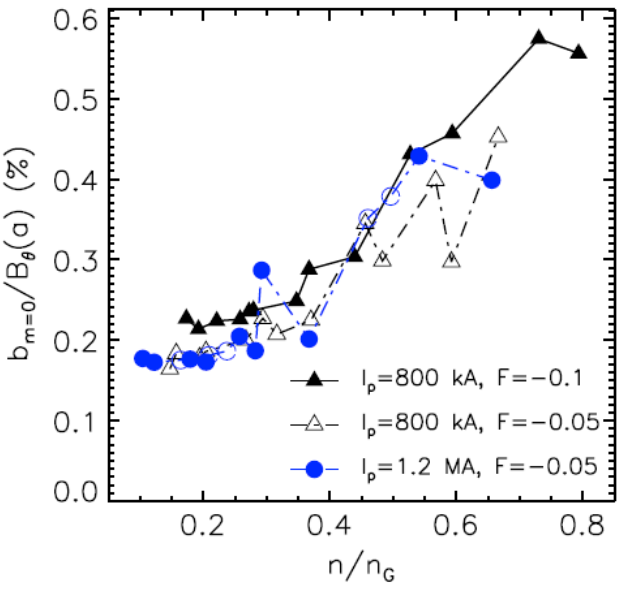

Figure 5.4: Plot of the $m = 0$, $-6 \leq n \leq -1$ modes normalized magnetic field perturbation as function of the ratio n/n_G: the entity of such modes grows approaching the density limit.

Among the $m = 0$ modes, the most dangerous one is shown to be the $m = 0$, $n = -1$ mode because it is responsible for the formation of a magnetic island (due to tearing modes intabilities). The island X-point corresponds to a stagnation point (found measuring the plasma toroidal flow) with a gas-puff imaging diagnostic, described in [1], that generates the accumulation of particles, by a modulation of the radial edge magnetic field. This very localized particle accumulation is at the basis of the density limit. The considerations are then confirmed by numerical studies of particles trajectory.
The role of the $m = 0$ modes for the density limit mechanism is confirmed also in [42], that is a study of the influence of the magnetic topology in the context of plasma wall interactions.
In a more recent study [46], the role of the $m = 0$, $n = -1$ mode is instead confirmed by a series of experiments where the amplitude of the mode was directly controlled with the system of 192 feedback coils, described in Section 3.4 and shown in Fig. 3.10. The main is shown in Figure 5.5: when the $m = 0$, $n = -1$ mode increases its amplitude, the associated edge island increases its size, up to a critical value when the field lines intercept the wall. At this point, PWI and density accumulation take place, triggering the density limit.

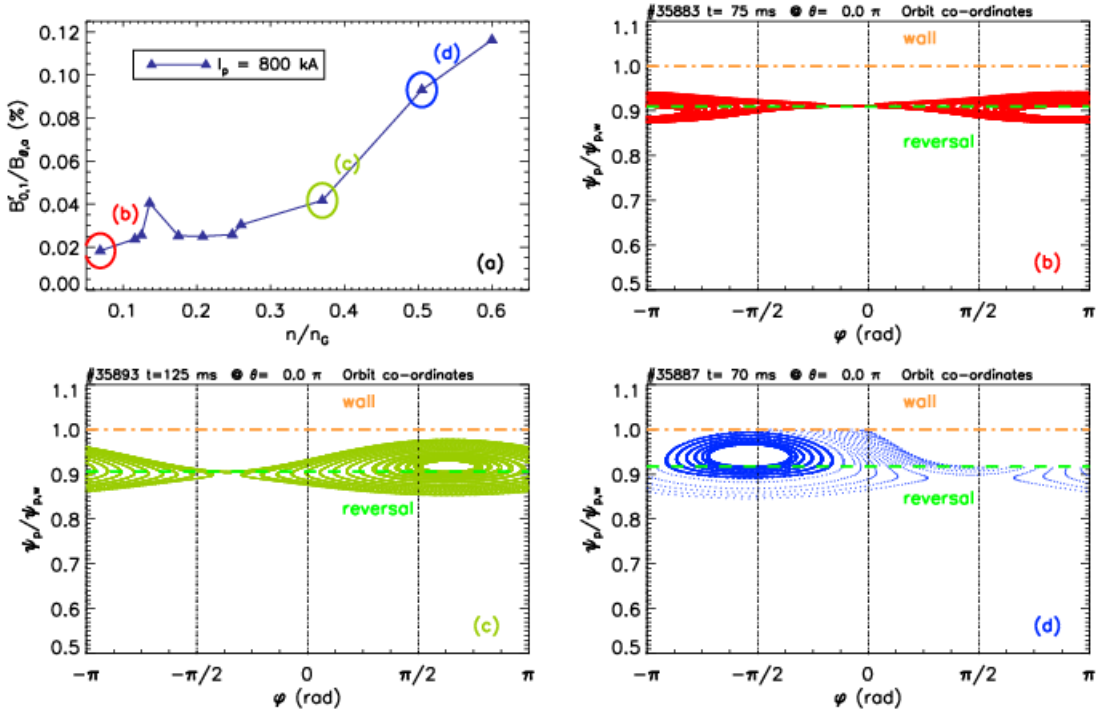

Figure 5.5: Plot of the $m = 0$, $n = -1$ mode normalized radial magnetic field as function of the ratio n/n_G: the entity of such mode grows approaching the density limit; (b) - (d) Magnetic topology of the $m = 0$, $n = -1$ island, for three discharges marked as circles in frame (a). The critical size of the island is reached when the flux surfaces intercept the first wall.

Also in the present work, the role of the $m = 0$ modes and, in particular the $m = 0$, $n = -1$, in understanding the density limit will be investigated on a wide database, described in the next section.

5.2 Hartmann number evaluation

In this section, the databases analyzed are described and the procedure followed to calculate the Hartmann number, starting from the experimental data, is presented.

5.2.1 Databases analyzed

The database of all the shots considered in this work is composed by five initial databases made up by RFX-mod shots (all in the RFP configuration) performed in different campaigns in between 2006 and 2016, before the shutdown phase. The discharges are chosen in order to scan a wide intervall in the density ratio n/n_G: $0.05 < n/n_G < 1$, that allows a study of the density limit on RFX-mod device.
After the initial choice of the shots, only the discharges with incomplete data (that do not allow the Hartmann evaluation) were discarded and no further selections of data were made.
The first database considered is composed by discharges # 35836 - #35851, #35883 - #35894 , #35902 - #35914 performed in year 2014. It was selected for a previous study regarding the density limit [46] and it is a scan in the plasma current into three intervals: 600 kA, 800 kA, 1 MA, with a careful control of the $m = 0$, $n = -1$ mode via the feedback system.
The second database is composed by shots in the intervals: #19911 - #19960 and #26303 - #26351. The first ones are old 2006 stimulated discharges for the first studies on the density limit, while the second were used in a subsequent campaign in 2009, also for density limit studies [47]. These shots are characterized by high electron density. The properties of the databases considered to study the density limit in terms of plasma current and F parameter are shown in figure 5.6.

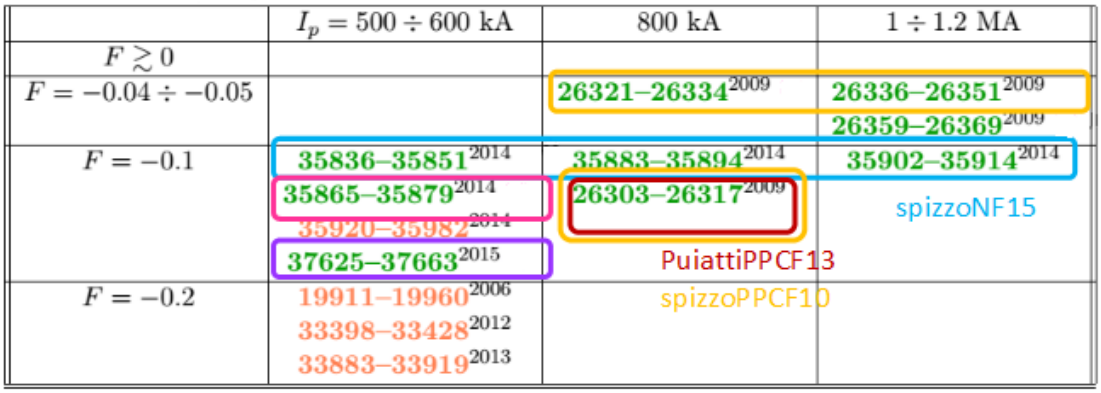

Figure 5.6: Representation of the shots databases used in the previous studies for the density limit, classified using plasma current and the F factor.

The third database was considered in [43] and it is composed by QSH low density shots, useful to explore transport barriers in the region with $n/n_G \sim 0.15$.
The fourth database contains various discharges in the interval # 26317 - # 36059 aimed at studying scaling laws on RFX-mod.
Finally, to increase the statistics, a fifth database was added, containing shots for the study related to the $m = 0$ modes that include the following shots: # 35920 - # 35936, # 35937, # 35942, # 35943 and # 35959 - # 35976 These shots were also performed in the 2014 campaign, but were not included in publication [46]. The final database is composed by 196 shots, allowing in this way a wide scan to study the density limit and also a scan on a very wide interval in the Hartmann number.

5.2.2 Hartmann number calculations

As it was previously shown, the Hartmann number H turns out to be a fundamental parameter to describe magnetic energy and edge magnetic field in numerical simulations and it is also the only dimensionless number that rules the equations of the visco-resistive model when the inertia terms are negligible. In addition relation (5.2) suggests the possibility of linking the ratio n/n_G with the value of $H_\perp$. For these reasons, the Hartmann number, in all its three possible definitions ($\|$, $\perp$, $\times$), is evaluated for all the database shots using formulas (2.88), (2.89) and (2.90).
To compute the Hartmann number, various plasma parameters need to be evaluated. The evaluation of the plasma parameters from the data directly collected by RFX-mod diagnostics is carried out by

means of an IDL routine, called `extcalc.pro`. The main results obtained using this program are the evaluation of: plasma current I_p, voltage toroidal loop V_{loop}, electronic density n_e and the ratio n/n_G, electron temperature T_e, and magnetic fields profiles. Given an initial threshold input for the plasma current, the routine calculates the extremes of the flat top current phase (central part of the plasma current signal, where the current is approximately constant in time). For each time instant, the density and the temperature profiles are averaged over the central region within a radius r that satisfies: $-0.15\,\text{cm} \leq r \leq 0.15\,\text{cm}$. Density profiles are measured via a 16-chord interferometer (described in Ref. [29]), while temperature profiles are measured in 84 positions with 7 mm spatial resolution by a Thomson scattering diagnostic which uses a custom built Nd:YLF (described in Ref. [3]). Time instants are based on the Thomson scattering measurements which are repeated at regular intervals of 25 ms. An example of the output of the routine `extcalc.pro` is shown in figure 5.7.

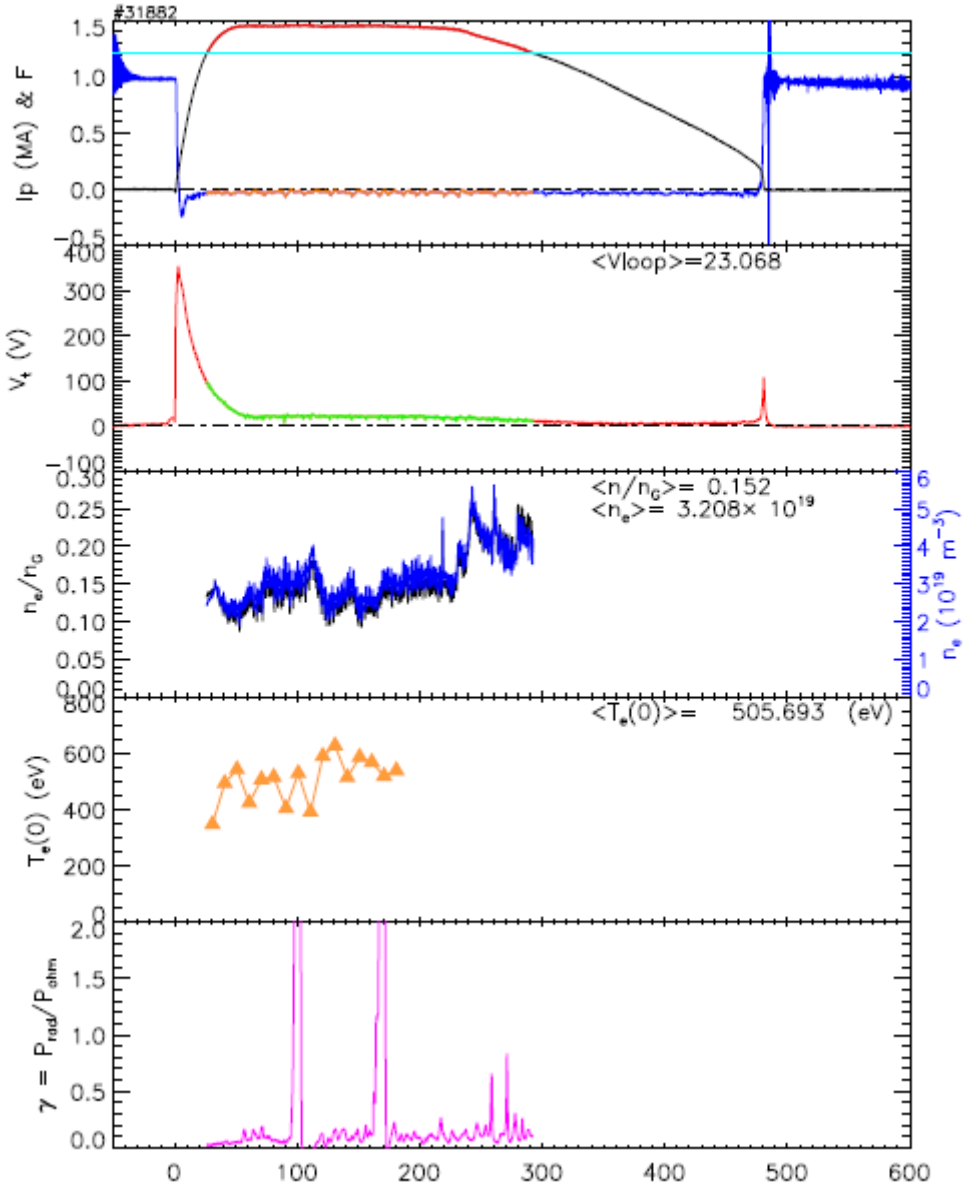

Figure 5.7: Graphical representation of the routine output, for shot # 31882. From top to bottom: the plasma current (with flat top phase), F parameter, toroidal loop voltage, density and Thomson scattering measurements of electron temperature, as a function of time [ms] and radiated power.

$H_\parallel$, $H_\perp$ and $H_\times$ are evaluated modifying the program `extcalc.pro`. The criteria used for estimating the parameters that appear in formulas (2.88)-(2.90) are here explained.

- The atomic number of the ions Z is replaced by the effective charge Z_{eff}, that takes into account

the composition of the plasma. RFX-mod discharges are made with hydrogen or deuterium, with impurities that are mainly constitute by carbon. The conventional value chosen is $Z_{eff} = 1.5$. This value has been chosen on the basis of previous studies on RFX, where Z_{eff} varied in the range $1.2 \leq Z_{eff} \leq 2$ as a function of the loop voltage in the range $30\,\mathrm{V} \leq V_{loop} \leq 50\,\mathrm{V}$, [14].

- The parameter $\gamma = m_i/m_p$ is easily obtained: $\gamma = 1$ (hydrogen), $\gamma = 2$ (deuterium). In this way, possible isotopic effects are fully taken into account in the present calculation.
- The minor radius a is already calculated by the routine, for the vast majority of the discharges $a = 0.459\,\mathrm{m}$.
- Regarding the magnetic field, the toroidal field on axis is chosen, $B = B_\phi(r = 0)$ because it is the reference value used in the codes, like SpeCyl. Since in many publications (see e.g. [52]) magnetic fluctuations are normalized to the edge poloidal field, $B_\theta(r = a)$, we recall here that in the BFM the ratio $B_0/B_\theta(a) = 1/J_1(2\theta) \approx 3$ for a typical value of the pinch parameter $\Theta \approx 1.5$.
- The electron temperature T_e is averaged on the central region (as it was explained) and each instant of the Thomson scattering diagnostic is considered. The evaluation of the Hartmann number will be repeated at each temperature data point. In this way, for each shot, many final values for $H_{\parallel,\perp,\times}$ are obtained. From the initial database of 196 shots, about 1700 Thomson scattering measurements, that implies about 1700 Hartmann number evaluations.
- Unfortunately no ion temperature T_i diagnostic is still available on the RFX-mod device. Studies of the ion temperature behaviour are carried out, for example, on the MST device [19] that is very similar to RFX-mod, because it works in the RFP configuration and it has comparable dimensions. MST is equipped with a spectroscopic system based on carbon impurities spectroscopic emission that allows for the evaluation of the ion temperature. The results are highlighted, for example, in [16], where it is shown that it is particularly difficult to model T_i in the RFP configuration. The ion temperature is of the same order of magnitude of the electron, but it is usually smaller, except for the instants in which the QSH phase is interrupted, in the so-called relaxation events: in these cases $T_i > T_e$. Since these time intervals are usually quite small, in this work the well accepted convention that $T_i = 0.5T_e$ is used without further considerations.
- The density is evaluated (considering the quasi neutrality hypothesis), in the central region, at the time of the Thomson scattering.
- The Coulomb logarithm $\ln\Lambda$ is treated as in [37]: We recall here that Coulomb logarithm is defined as $\ln\Lambda := \ln(r_{max}/r_{min})$, being r_{max} and r_{min} the Debye length and the distance of closest approach during particle collisions at the average velocity.

These criteria allow for the evaluation of the Hartmann number and the possibility of connecting it with plasma parameters and the phenomenological parameter n/n_G.

5.3 Scaling laws based on Hartmann number

Using the results obtained in Section (5.2) one expects to find a good scaling relation of the type $n/n_G = A \times H^B$, where A and B are coefficients to be determined by means of the fit procedure.
To verify the existence of such relations the ratio n/n_G is plotted as a function of $H_\parallel$, $H_\perp$ and $H_\times$. The results are shown in figures 5.8, 5.9 and 5.10.

As you can see, no evident relation is found using $H_\parallel$ because the data do not display any correlation ($r = 0.15$). The results are different when $H_\perp$ and $H_\times$ are considered, higher correlation values are obtained: $r = -0.75$ (for $H_\times$) and $r = -0.82$ (for $H_\perp$). The fit results are here reported:

$$\frac{n}{n_G} = (210 \pm 30)\, H_\times^{-0.386\pm0.008}, \tag{5.3}$$

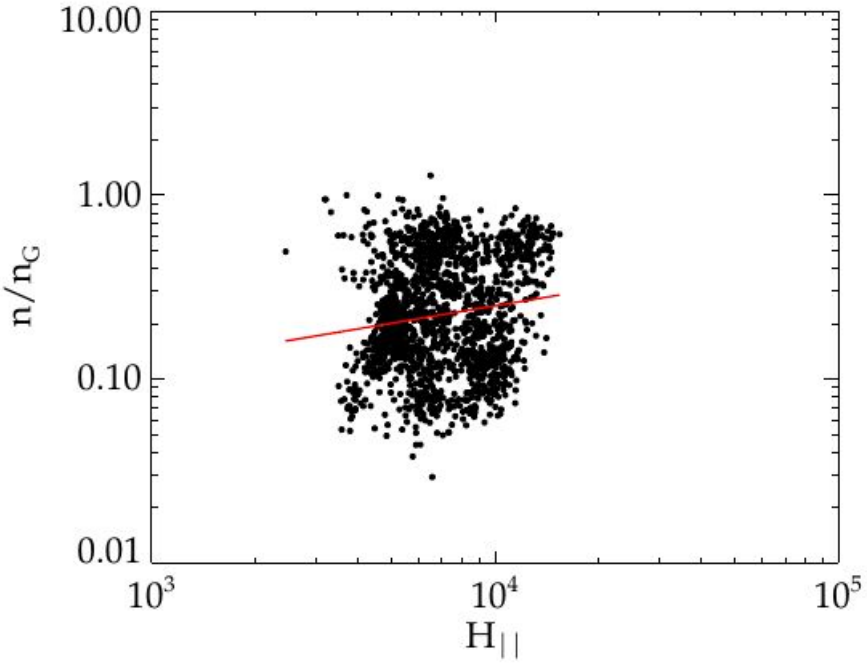

Figure 5.8: n/n_G as function of $H_{\|}$, RFX-mod data.

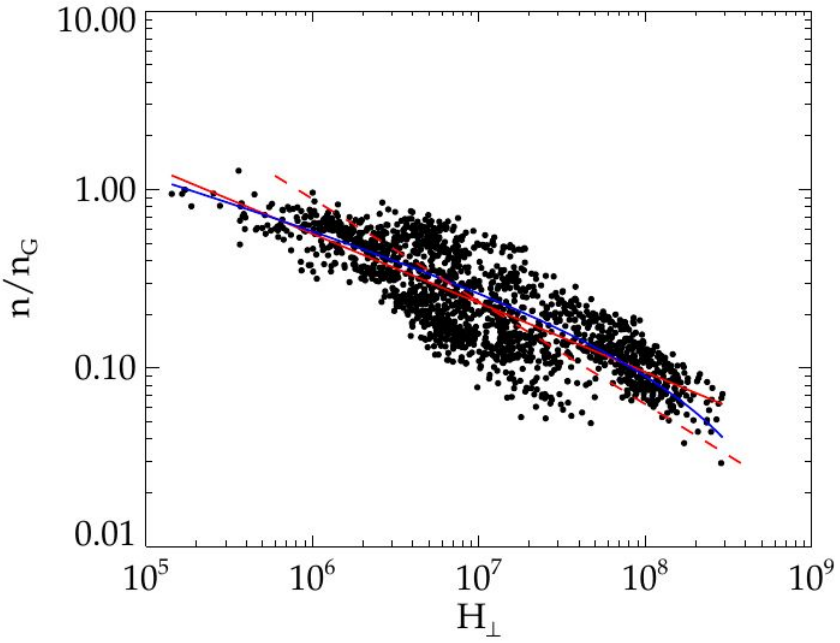

Figure 5.9: n/n_G as function of $H_{\perp}$, RFX-mod data. Data are fitted following three different procedures. Solid red line indicates the scaling law n/n_G as a function of $H_{\perp}$, dashed red line the one with the exchanged axes, the blue line the one with the additive constant.

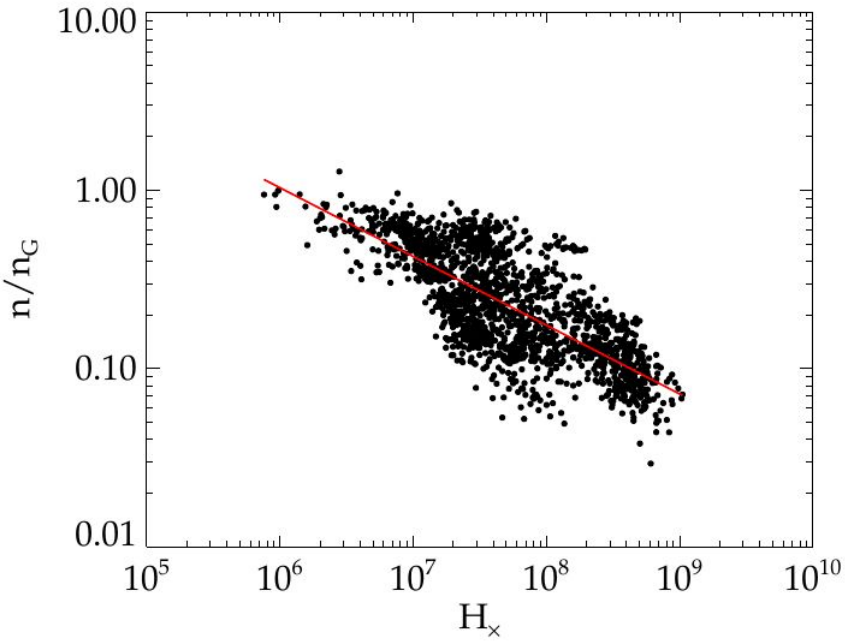

Figure 5.10: n/n_G as function of $H_\times$, RFX-mod data.

$$\frac{n}{n_G} = (120 \pm 10)\, H_\perp^{-0.387\pm0.007}. \tag{5.4}$$

On the basis of these fits, the parameter that maximizes the correlation is the perpendicular Hartmann $H_\perp$, and therefore it will be closer to describe the density limit phenomenology. Other fit procedures can be considered: since the uncertainty estimate of the single points is quite difficult to obtain, a fit with exchanged axis, or a fit with an additive constant can be calculated, to try a different scaling law dependence. The results are:

$$H_\perp = (80 \pm 4) \times 10^4 \times \left(\frac{n}{n_G}\right)^{-1.74\pm0.03}, \tag{5.5}$$

$$\frac{n}{n_G} = (31 \pm 28) \times H_\perp^{-0.28\pm0.08} - 0.10 \pm 0.14. \tag{5.6}$$

These additional fits add some details to the results obtained so far: in particular no additive constant is needed because it is zero within the errors.
As it is evident from the plot, a wide range in the Hartmann number $H_\perp$ is covered (more than three orders of magnitude), that is different with respect to one covered by the numerical simulations. To exemplify the different types of discharges considered in the database (and the relative Hartmann number), in table 5.1, $H_\perp$ is calculated for three typical discharges.

Table 5.1: $H_\perp$ calculation examples for three representative shots.

shot	$B_0[T]$	T_e [eV]	γ	n_e $[10^{19}m^{-3}]$	$\ln\Lambda$	$H_\perp$	n/n_G
# 19956	0.427	110	1	4.84	14.3	7.95×10^5	0.739
# 26303	0.784	314	1	2.31	16.3	1.42×10^7	0.202
# 30775	1.69	664	1	2.35	17.4	1.27×10^8	0.093

From figure 5.9 it seems clear that, although $H_\perp$ well describes the density limit, there are values of $H_\perp$ like 10^7 corresponding to quite different values of n/n_G. To highlight particular trends the

data-points are divided into three different subsets, based on the plasma current value: $I_p < 0.75\,\mathrm{MA}$, $0.75\,\mathrm{MA} \leq I_p < 1.25\,\mathrm{MA}$ and $I_p \geq 1.25MA$, shown in figure 5.11.

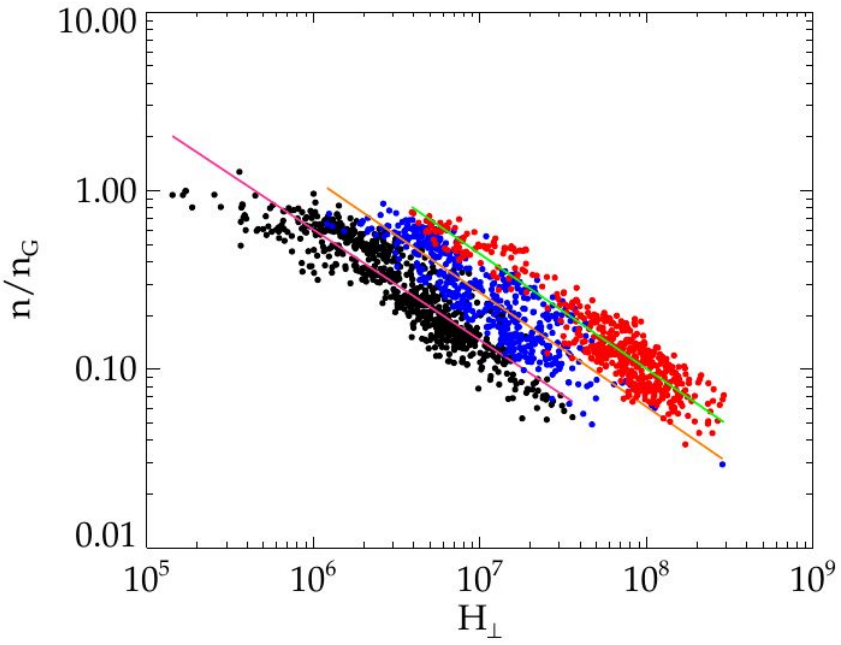

Figure 5.11: n/n_G as function of $H_\perp$. Different ranges of current are shown: low current (black points), medium current (blue points), high current (red points).

If the fits are restricted to the three subsets, the values in table 5.2 are found:

Table 5.2: Fit results of the plot n/n_G Vs $H_\perp$: data subdivided in three subsets on the basis of plasma current.

Plasma current	Fit relations	Correlation
$I_p < 0.75\,\mathrm{MA}$	$n/n_G = (3100 \pm 500) H_\perp^{-0.62\pm0.01}$	$r = -0.91$
$0.75\,\mathrm{MA} \leq I_p < 1.25\,\mathrm{MA}$	$n/n_G = (8000 \pm 2000) H_\perp^{-0.64\pm0.02}$	$r = -0.88$
$I_p \geq 1.25\,\mathrm{MA}$	$n/n_G = (14000 \pm 3000) H_\perp^{-0.64\pm0.02}$	$r = -0.94$

The final coefficients reported in table 5.2 point out that, once fixed a current interval, the ratio n/n_G is very well described by the dimensionless number $H_\perp$, because the correlation coefficients assume a relatively high value $r \simeq 0.9$ and the slopes of the lines (that represent a power law in log scale), are almost the same for the three current intervals. The interpretation of this result is still work in progress, but it is well known that in RFX-mod different currents correspond to different wall conditions and also different Z_{eff}, [14].
However, the most interesting aspect of this result is that the description of a phenomenological parameter (n/n_G) is obtained in terms of the Hartmann number, that is naturally introduced in the theoretical framework that was developed in Chapter 2 with quite restrictive hypotheses, that turns out to be rather good in reaching a satisfying description of the density limit in the RFP configuration. So far, the approach based on the Hartmann number has succeeded in describing: magnetic fields and magnetic energy (in SpeCyl numerical simulations) and the ratio n/n_G (using RFX-mod data). Since Hartmann is the key parameter of the visco-resistive model, that in past works achieved great results in describing the RFP physics, as further verification, in this work, scaling relations of plasma parameters like plasma current I_p, magnetic field on axis $B_\phi(r = 0)$, and the electron temperature in the central region T_e are shown.
In figures 5.12, 5.13 the results of the plots, limited to I_p and $B_\phi(r = 0)$ are shown.

The scaling relations obtained display a satisfying value of the correlation coefficient: $r = 0.83$ (for the plasma current) and $r = 0.85$ (for the magnetic field on axis). The numerical results are:

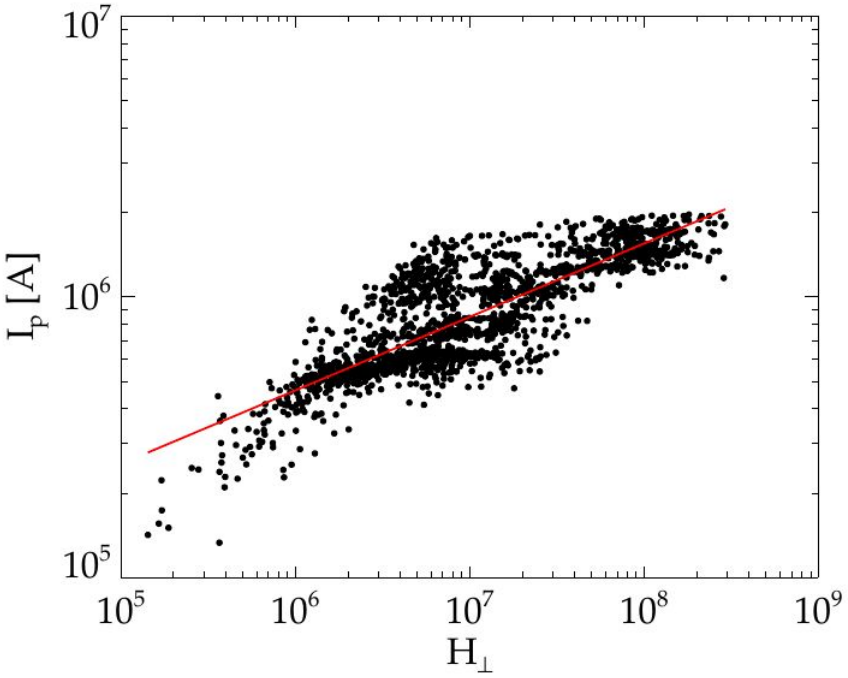

Figure 5.12: Plasma current I_p, as function of $H_\perp$.

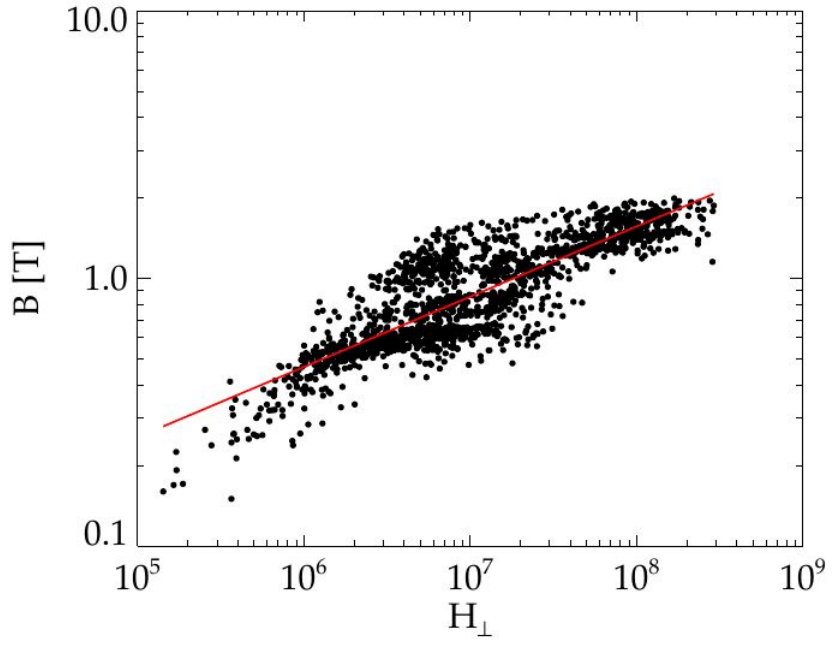

Figure 5.13: Toroidal magnetic field on axis, as function of $H_\perp$.

$$I_p\ [\mathrm{A}] = (12500 \pm 800)\, H_\perp^{0.262\pm0.004}, \tag{5.7}$$

$$B_\phi(r=0)\ [\mathrm{T}] = (0.0124 \pm 0.0008)\, H_\perp^{0.263\pm0.004}. \tag{5.8}$$

that confirm $H_\perp$ to be a good parameter in describing the electromagnetic properties of RFP plasmas, as it was highlighted by numerical simulations.
The scaling law of T_e as function of $H_\perp$ is even more interesting because it reaches a very high value for the correlation coefficient: $r = 0.96$. The high level of correlation is also clear from the plot (shown in figure 5.14) and from the low relative entity of the uncertainty in the relation obtained:

$$T_e\ [\mathrm{eV}] = (0.76 \pm 0.03)\, H_\perp^{0.371\pm0.003}. \tag{5.9}$$

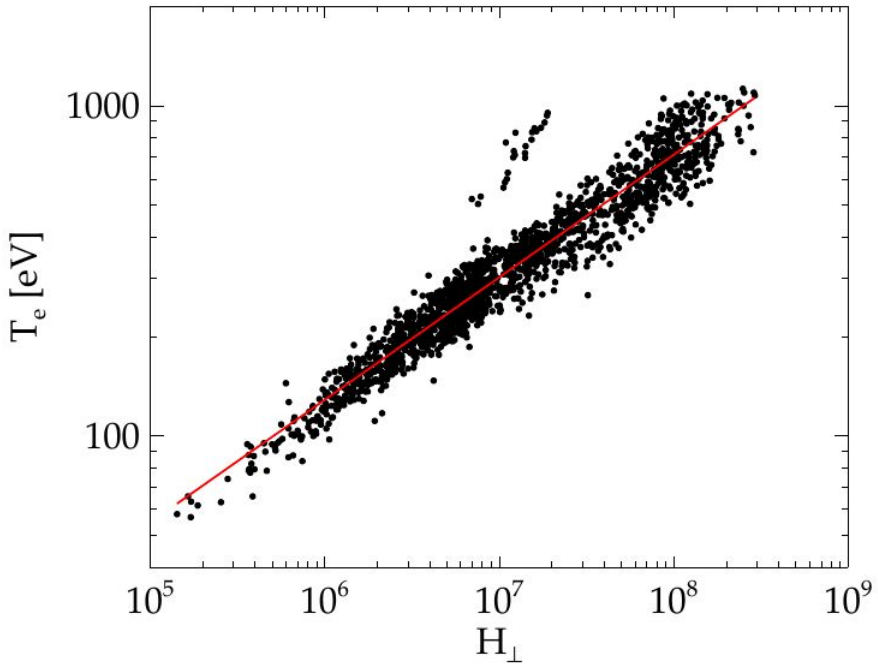

Figure 5.14: Electron temperature (averaged on the central plasma region) I_p, as function of $H_\perp$.

It is worth noting that the empirical scaling of T_e shown by Innocente et al. [28] reproduces the exponents that link Hartmann to the macroscopic plasma parameters in Eq. (2.89).
The satisfying results obtained by the use of $H_\perp$ in describing measurements of plasma parameters on RFX-mod device can be considered as a further confirmation of the role of transport physics in the direction perpendicular to the magnetic field and of the validity of the visco-resistive model, and consequently of its implementations (like SpeCyl), in modelling many aspects of RFP plasmas.

5.4 Mode calculations: the Newcomb method in toroidal geometry

The second part of the data analysis is aimed at investigating the role of the $m = 0$ modes (and particularly the $m = 0$, $n = -1$) in describing the density limit. Consequently, this section is devoted to briefly explain how the different modes contributions to the magnetic field are calculated in toroidal geometry, by means of the Newcomb's equations.
Details about such a method can be found in Ref. [59]. In this section only the main results are reviewed, without any demonstration, just to describe how the modes analyzed in the next sections

are calculated, starting from the experimental pick-up probe data.
The starting point is given by the ideal force-balance conditions, determined at the MHD equilibrium. Also the hypothesis of negligible pressure is made (low β plasma), obtaining:

$$\mathbf{j} \times \mathbf{B} = 0, \qquad \nabla \times \mathbf{B} = \mu_0 \mathbf{j}, \qquad \nabla \cdot \mathbf{B} = 0. \tag{5.10}$$

These equations are solved in toroidal geometry with its coordinates: radius r, poloidal angle θ and toroidal angle ϕ. The change of coordinates is ruled by the modulus of the determinant of the Jacobian matrix, that is defined as:

$$\frac{1}{\sqrt{g}} := \nabla r \times \nabla \theta \cdot \nabla \phi. \tag{5.11}$$

The magnetic field can be expressed by two flux functions, here introduced as F and ψ:

$$\mathbf{B} = \nabla F \times \nabla \theta - \nabla \psi \times \nabla \phi. \tag{5.12}$$

Consequently to this definition, the magnetic field components (toroidal, poloidal) and the radial perturbation are expressed in terms of flux functions:

$$B^\theta = \frac{1}{\sqrt{g}} \frac{\partial \psi}{\partial r}, \qquad B^\phi = \frac{1}{\sqrt{g}} \frac{\partial F}{\partial r}, \qquad b^r = \frac{1}{\sqrt{g}} \left(\frac{\partial F}{\partial \phi} + \frac{\partial \psi}{\partial \theta} \right). \tag{5.13}$$

The equation is solved using a perturbation approach: each physical quantity $X(r, \theta, \phi)$ is written as sum of an equilibrium term (dominant and axisymmetric) and a perturbed one (non axisymmetric) as in:

$$X(r, \theta, \phi) = X_0(r, \theta) + x(r, \theta, \phi). \tag{5.14}$$

In this way flux functions are rewritten as sum of the Fourier modes contributions, similarly to SpeCyl, but now in toroidal geometry. The mode with $m = 0$, $n = 0$ corresponds to the equilibrium term.

$$\psi(r, \theta, \phi) = \psi_0(r) + \sum_{m,n \neq 0} \psi_{m,n}(r) e^{i(m\theta + n\phi)}, \tag{5.15}$$

$$F(r, \theta, \phi) = F_0(r) + \sum_{m,n \neq 0} f_{m,n}(r) e^{i(m\theta + n\phi)}. \tag{5.16}$$

Replacing equations (5.15) and (5.16) one can get a set of differential equation with unknowns $\psi_{m,n}(r)$ and $f_{m,n}(r)$ that are Newcomb equations:

$$\begin{aligned} &- n \left(\frac{g_{\theta,\theta}}{\sqrt{g}} \right)_{0,0} \frac{d\psi_{m,n}}{dr} + mK(r) \frac{df_{m,n}}{dr} + \sigma \left(n f_{m,n} + m \psi_{m,n} \right) + \\ &\quad + in \left(\frac{g_{r,\theta}}{\sqrt{g}} \right)_{0,1} \times \left[-n f_{m+1,n} - (m+1) \psi_{m+1,n} + n f_{m-1,n} + (m-1) \psi_{m-1,n} \right] + \\ &\quad\quad - n \left(\frac{g_{\theta,\theta}}{\sqrt{g}} \right)_{1,0} \times \left[\frac{d\psi_{m-1,n}}{dr} + \frac{d\psi_{m+1,n}}{dr} \right] = 0, \end{aligned} \tag{5.17}$$

$$-\frac{d}{dr}\left(K(r)\frac{df_{m,n}}{dr}\right)+\left(\frac{g_{r,r}}{\sqrt{g}}\right)_{0,0}\left[mn\psi_{m,n}+n^2 f_{m,n}\right]-\sigma\frac{d\psi_{m,n}}{dr}-\frac{nf_{m,n}+m\psi_{m,n}}{m+nq}\frac{d\sigma}{dr}+$$
$$+n\left(\frac{g_{r,r}}{\sqrt{g}}\right)_{0,0}\times\left[(m-1)\,\psi_{m-1,n}+nf_{m-1,n}+(m+1)\,\psi_{m+1,n}+nf_{m+1,n}\right]+$$
$$-in\left(\frac{g_{r,\theta}}{\sqrt{g}}\right)_{1,0}\times\left[\frac{d\psi_{m+1,n}}{dr}-\frac{d\psi_{m-1,n}}{dr}\right]=0, \quad (5.18)$$

in which g represents the metric tensor in toroidal geometry, the factor $K(r) := \frac{R^2}{\sqrt{g}}$, and the function $\sigma(r) = \mu_0 \frac{j^r_{m,n}}{b^r_{m,n}}$. Solving the Newcomb equations allows for the evaluation of the magnetic field modes, because the solutions for $F_{m,n}$ and $\psi_{m,n}$ can be used to evaluate b^r in (5.13).
The computational procedure to find the eigenfunctions and the modes of the magnetic field is made using Fortran routines written for this aim: first of all, the toroidal equilibrium is calculated; then, the Newcomb equations are solved, using a basis of six functions $(Y_1, ..., Y_6)$, defined on three different domains of the radius (internal, medium and external): the solution for the flux function is given by a linear combination of the Y functions, that needs the determination of six coefficients $c_1, ..., c_6$. The modes considered in RFX-mod are the ones with $m = -1, 0, 1, 2$ and low $|n|$. The boundary conditions to solve Newcomb equations are found imposing zero resistivity at $r = b$ (that is the position of the external vessel) and fitting a number of experimental measurements of the magnetic field harmonics: n_ϕ for the toroidal component, n_θ for the poloidal one and n_r for the radial one, satisfying the condition: $N = n_\phi + n_\theta + n_r$, in which N is the number of independent functions to be determined.
The resulting code is called NCT (NewComb Toroidal) and it is described in Ref. [59]. The routine that makes use of NCT on a selected shot and time is written in IDL and it is called `m0ave.pro`. The advantage of NCT with respect to SpeCyl is that it is toroidal, it is directly linked to experimental measurements, allows for a realistic boundary condition (better than that of SpeCyl described by Eq. (4.7)) and it is rather fast. The drawbacks is that the Newcomb approach is intrinsically linear and ideal MHD, with a perturbative approach at the first order (see Eq. (5.14)), while SpeCyl is fully non-linear.

5.5 Scaling of the $m = 0$, $n = -1$ mode with Hartmann number

In this section the analysis of the role of the $m = 0$, $n = -1$ mode in describing the density limit is investigated. To reach this goal the routine `m0ave.pro` was modified during this work to calculate the $m = 0$, $n = -1$ mode and the eigenfunction $B^r_{0,-1}(r)$.
Since in works like [47] and [46] a clear role of the quantity $B^r_{0,-1}(r = a)$ is highlighted, after estimating the edge radial magnetic field of the mode $m = 0$, $n = -1$ for all the shots belonging to the initial database, and for each Thomson scattering measurement instant, the eigenfunctions are evaluated at $r = a$ (at the the plasma boundary), obtaining about 1700 measurements.
To confirm the results determined in previous works, the plot 5.5 is repeated, but this time the number of points available is clearly higher, because a much wider database is analyzed (see figure 5.15).

As additional result, one can claim the $m = 0$, $n = -1$ mode to be linked to the value of the perpendicular Hartmann number $H_\perp$, since it is turned out to be a good parameter in describing the ratio n/n_G from the plots in figures 5.9 and 5.11. For this reason $B^r_{0,-1}(a)/B^\theta(a)$ is plotted as function of $H_\perp$ (5.16):

The general trend found in this case is a decrease of the $m = 0$, $n = -1$ mode contribution in increasing $H_\perp$. In particular, one can notice that the radial field is particularly important for $H_\perp < 10^7$, the region in which the density limit is approached, suggesting the importance of the role played by the mode considered for the plasma stability.

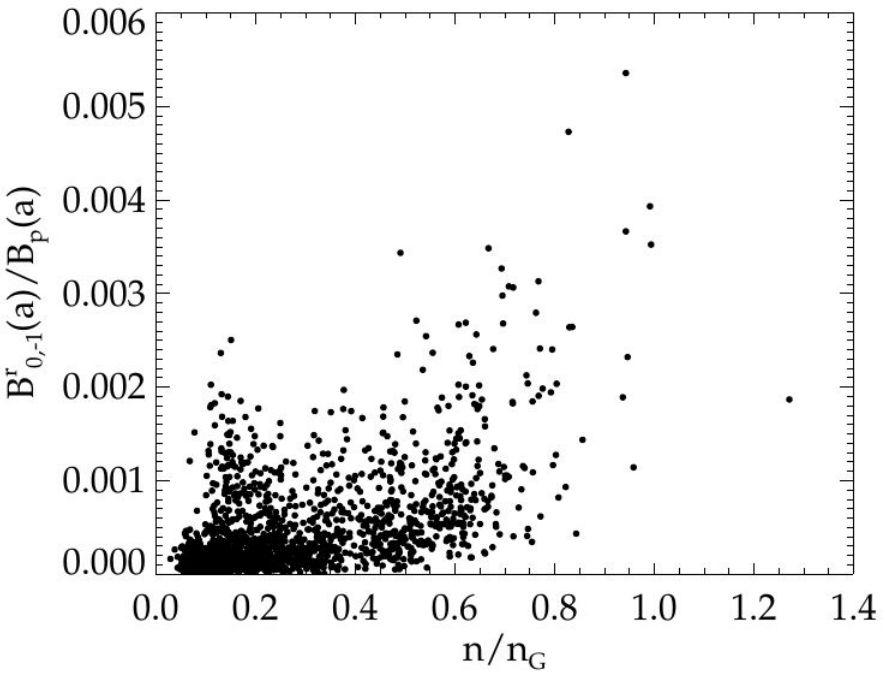

Figure 5.15: Normalized edge radial magnetic field for the $m = 0$, $n = -1$ mode, as function of n/n_G, RFX-mod data.

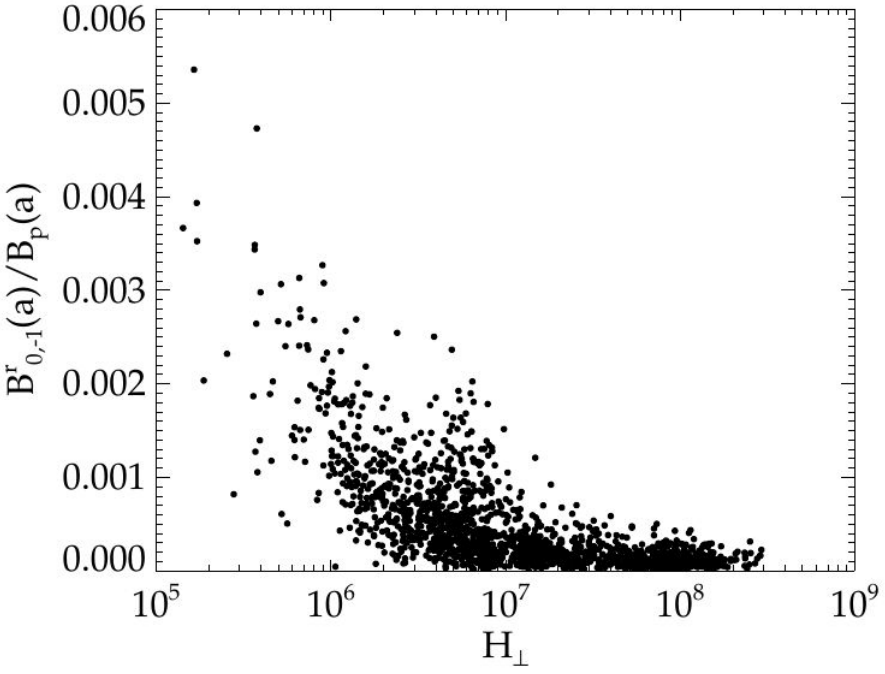

Figure 5.16: Normalized edge radial magnetic field for the $m = 0$, $n = -1$ mode, as function of $H_\perp$, RFX-mod data.

5.6 Comparison between simulations and experimental data: edge radial field

So far, the role of the edge magnetic field in triggering the density limit was investigated from the point of view of numerical simulations and analyzing the experimental data. In both cases the dimensionless Hartmann number (H or $H_\perp$) turned out to be a good parameter in determining the trends, providing the validity of the visco-resistive MHD in modelling tearing mode dynamics in the RFP.
In this final section a comparison between numerical simulations and experimental measurements is made, highlighting the aspects in common and the differences among them.
First of all, it is easily noted that the two ranges of the domain in H and $H_\perp$ are different, due to the fact that simulations with high H are really time consuming. Secondly, the ideal zero resistivity hypothesis of the SpeCyl code implies $B^r(r=a)=0$. Although in this work the value $B^r_{0,-1}(r=0.95a)$ is taken into account, one cannot expect good quantitative agreement observing the amplitude of one single mode, although the two slopes are compatible. This is the reason why the dominant (among the $m=0$) modes is considered in comparison with the experimental measurements of the $m=0$, $n=-1$ mode, that is known to be the most important, in this second case. The comparison can be carried out observing figures 5.17 and 5.18: in both cases the field is normalized to the magnetic field on axis.

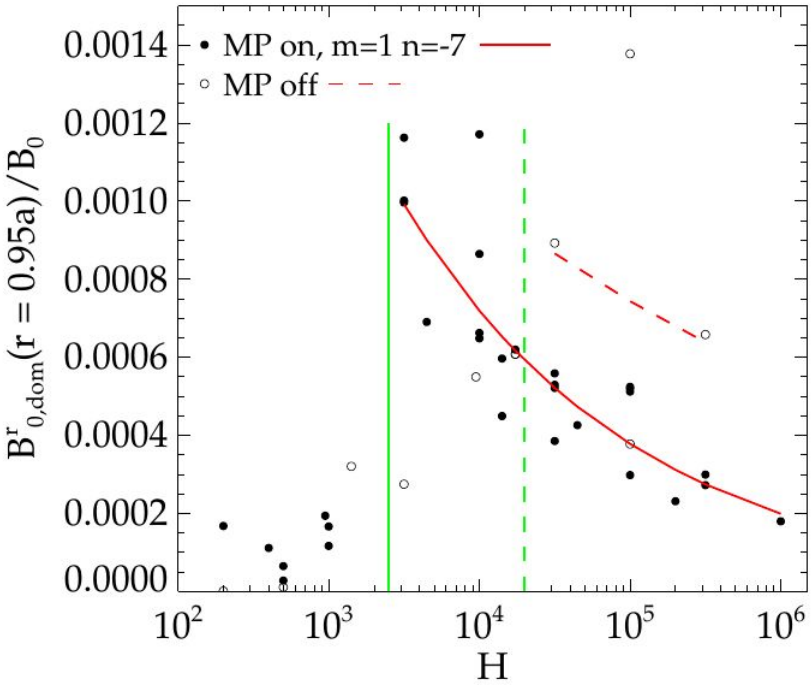

Figure 5.17: Edge radial magnetic field $m=0$ $n=-1$ mode (numerical simulations).

Numerical simulations are relevant (for the comparison) only beyond the threshold for H, where the field displays a negative trend. To make a quantitative comparison the two slopes with which the magnetic field decreases are obtained via fit procedure and compared:

$$B^r_{SIM}(r=0.95a) \propto H^{-0.28\pm0.03}, \qquad B^r_{EXP}(r=a) \propto H_\perp^{-0.53\pm0.01} \tag{5.19}$$

about numerical simulations, only those with a stimulation of 2 - 4 % of the mode $m=1$, $n=-7$ are taken into account because they constitute a populated and realistic sample.
Comparing the result, that is qualitatively similar (negative slope), the two trends do not result compatible making difficult a quantitative comparison. Many aspects contribute to this difference and, among them, the following have to be noticed:

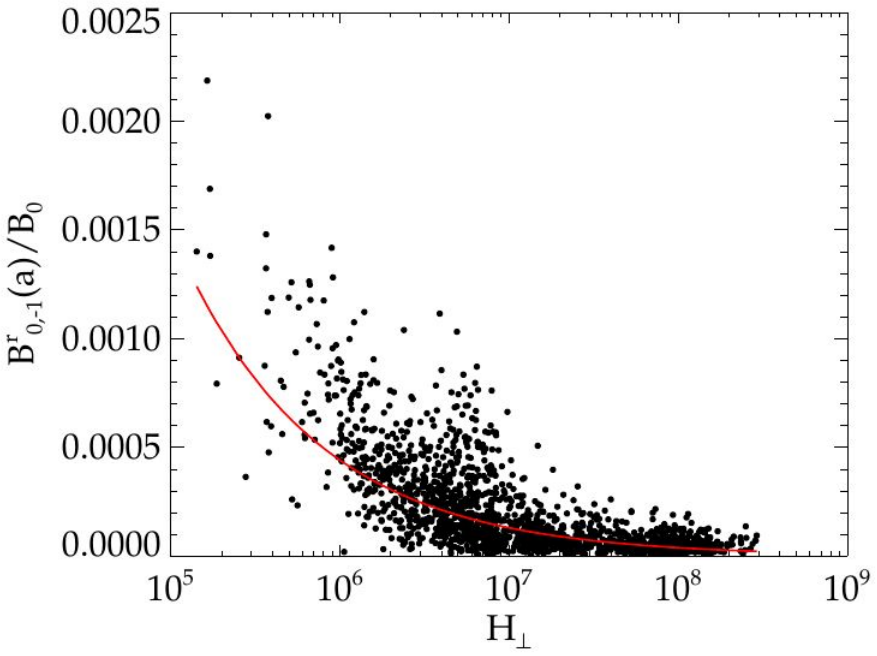

Figure 5.18: Edge radial magnetic field for the dominant $m = 0$, mode, experimental data.

- the zero resistivity boundary condition imposed in the simulations is not satisfied in the experimental conditions,
- in the two cases different intervals for H and $H_\perp$ are covered,
- H and $H_\perp$ are now defined in terms of central plasma parameters (different choices in the definition could be taken),
- resistivity $\eta(r)$ and viscosity $\nu(r)$ assume (in Specyl) a simplified space-time dependence and are not evolved self-consistently.

To complete this comparison, in figure 5.19 the amplitude and the trends of the radial edge magnetic field are shown, considering both numerical simulations and experimental data in a single figure. The points are obtained by averaging the initial data over equal logarithmic intervals, and associating to the average its uncertainty. In this case also the simulations with absence of stimulation are added to the sample.

This figure provides an interesting scan over a very wide range of the Hartmann number (considering H for the simulations and $H_\perp$ for the experimental measurements) that, using the scaling law (5.4), is converted in the correspondent value of the ratio n/n_G. As in figure 5.18, the mode considered in the simulation is the dominant one evaluated at $r = 0.95a$, due to the reasons mentioned above.
In the region characterized by the lowest values of H (10^2 - 10^3), corresponding to a high value of n/n_G, (which does not allow, at the moment, the comparison with the data) the simulations are characterized by an increasing trend of the magnetic field. This behaviour abruptly changes at $H \approx 10^4$, where the slope of the magnetic field becomes negative, displaying a similar behaviour to the one shown by experimental data, simply shifted to lower Hartmann values. The origins of this shift may be found both in the definitions considered for H and $H_\perp$ and in the initial zero resistivity boundary conditions, that strongly affects the behaviour of edge radial magnetic field.
The region with higher $H_\perp$ (characterized by a low n/n_G ratio) can not be explored using numerical simulations and so there are only experimental data available, that keep the negative trend for the magnetic field.
To conclude, the agreement found between numerical simulations and experimental data is quite satisfying, considering the region of the domain (in H and $H_\perp$) in which they are both available.

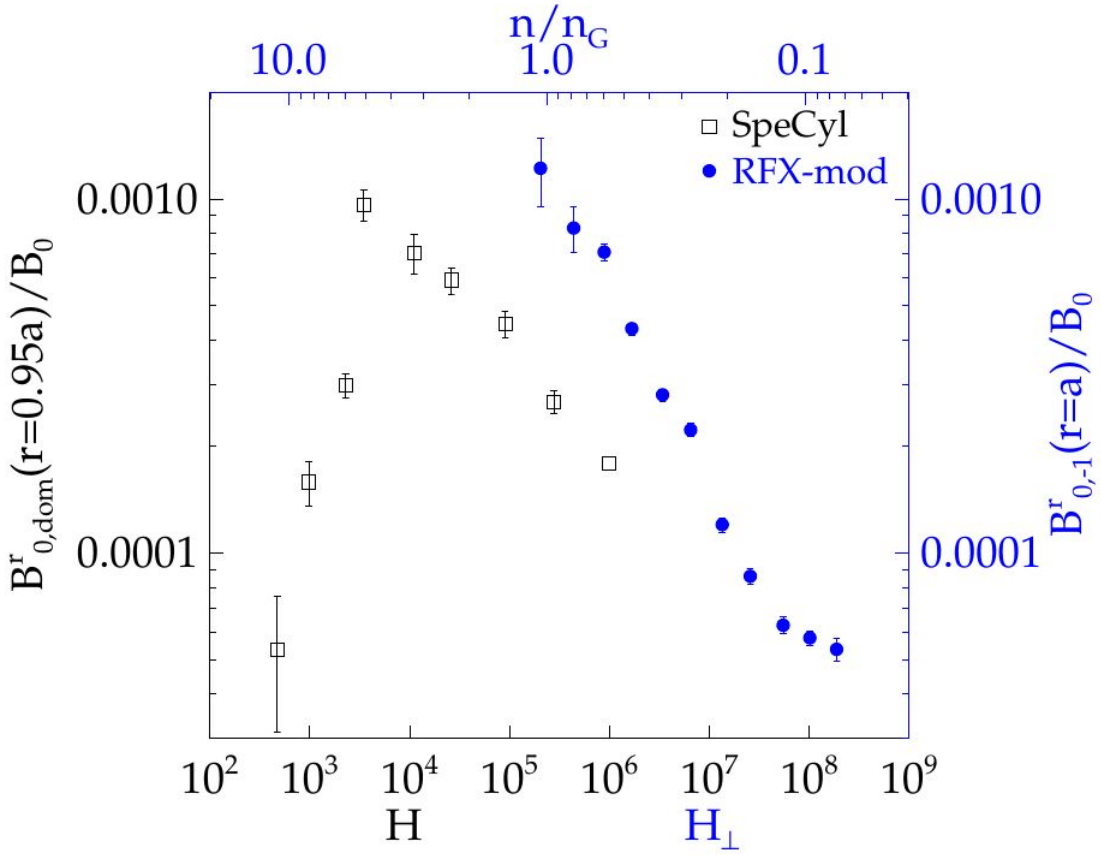

Figure 5.19: Comparison of normalized edge radial magnetic field between numerical simulations and experimental data (blue color). The points are obtained averaging data over equal logarithmic intervals.

Conclusions

In this Thesis the density limit was studied, following a multiple point of view approach, that involves theory of transport, visco-resistive MHD numerical simulations and RFX-mod data analysis. The goal stated at the beginning was to provide a better understanding of the density limit, with particular regard to the role of edge magnetic field instabilities.
Until now, the most accredited interpretation in the study of the density limit, due to Greenwald, is exclusively a phenomenolgical one based on experimental data, without a reference to a precise theoretical context.
The present work, on the other hand, aims at understanding such a phenomenon in the context of visco-resistive magnetohydrodynamics, limited to the RFP configuration, only.
To achieve this goal, following the derivation of Braginskii equations, transport coefficients were presented, introducing their dependence on plasma physical quantities and the visco-resistive model was derived. The fundamental parameter of the latter turns out to be the Hartmann number, obtained using a proper change of coordinates.
A second phase of the study consisted in the analysis of a database composed by 95 simulations performed using the visco-resistive model by means of the SpeCyl code (and spanning a range of Hartmann number values from 10^2 to 10^6), together with a set of five databases that globally consist in 196 RFX-mod shots, whose Hartmann number was evaluated. The most significant results obtained are summarized in the following points:

- In SpeCyl numerical simulations, the Hartmann number H turns out to be a good parameter in the description of magnetic energy and edge magnetic field. In particular, H was confirmed to be an order parameter that rules the transition between different plasma states (MH and SH/QSH), with threshold values for the transition of about 10^3 - 10^4. In particular, at $H > 10^4$ a decreasing trend of magnetic energy and m=0 modes intensity with H was found, to be compared with data from RFX-mod shots.

- Using RFX-mod shots data, a scaling law that links the value of the ratio n/n_G with the parameter $H_\perp$ is found with a satisfactory value for the correlation ($r = -0.82$) that can be further improved if the discharge current is selected.

- The Hartmann number $H_\perp$ is found to be a good parameter in the description of plasma physical quantities (directly evaluated from the experimental measurements) like the plasma current I_p, the toroidal magnetic field on axis B_0 and the electron temperature T_e (averaged over the central region), providing an important confirmation to the use of the visco-resistive model in modeling RFP plasmas.

- From the mode analysis, the role of the $m = 0$ modes and, in particular, of the $m = 0$, $n = -1$ mode clearly emerges from the observation of the edge radial magnetic field. The particular growth of $B^r_{0,-1}(r = a)$ in fact is considered as a precursor of the density limit.

- As final result, a comparison between numerical simulations and experimental data is made, finding a general qualitative agreement analyzing the $m = 0$ edge radial magnetic field. To be more precise, a similar negative trend of the edge radial magnetic field with respect to the Hartmann number and comparable amplitudes are found between the dominant mode (evaluated at $r = 0.95a$) in the simulations and the $n = -1$ (evaluated at $r = a$) for the experimental

measurements.

The results just mentioned suggest future developments for this research, in particular to improve the agreement between simulations and experimental data, overcoming the difficulties expressed at the end of Chapter 5.
One of the most important difficulties that prevent the agreement is related to the ideal boundary conditions implemented in the SpeCyl code, that particularly affect the study of the edge radial magnetic field. This problem could be faced analyzing, first of all, also the other components of the edge magnetic field and trying to directly implement, in the future, a more realistic boundary condition.
Another possibility to reduce the gap could come from experimental campaign of the future upgraded experiment RFX-mod2, in which the removal of the resistive vessel is foreseen, providing a reduction of the boundary resistivity.
Another important improvement could be found introducing (in the SpeCyl code) a self consistent evolution of resistivity and viscosity and a realistic profile for the viscosity. Useful expressions to implement could be those derived by Braginskii for the transport coefficients in the perpendicular direction with respect to the magnetic field (that were shown to model the majority of the physical phenomena analyzed by means of $H_\perp$).
Despite these possible improvements, from the final comparison between numerical simulations and experimental data (Fig. 5.19) some important results can be drawn:

- the QSH branch of SpeCyl simulations (negative slope for H) describes quite well both the MH to QSH transition in experiment, and the associated onset of the density limit for $H_\perp < 10^7$, which corresponds to the well-known threshold value of $n/n_G = 0.35 - 0.4$, [43] - [46].
- Given the above result, at least in the RFP case, when treating the density limit one should abandon the phenomenological n_G parameter in favor of $H_\perp$. Since the growth of the $m = 0$, $n = -1$ island is the element in linking the visco-resistive MHD Hartmann parameter to the density limit, it is worth exploring the possibility that $H_\perp$ could be the order parameter also in the tokamak density limit, where a similar role is played by the $m = 2$, $n = -1$ mode [50]. In this respect, a recent theory of the density limit on the NSTX tokamak (USA) involves a thermal destabilization of edge islands prior to the density limit, similar to what observed in RFX-mod [23], [56]: this would suggest a critical role of $H_\perp$ also in tokamaks.
- The SH branch of SpeCyl simulations (positive slope of H), which was the original which helical state described in the first papers on QSH [12], [20], is still far from the experimental domain. To obtain the pure theoretical Single Helicity one should push density beyond $n/n_G \geq 5$, which appears to be rather difficult from an experimental point of view, and maybe beyond the full radiative collapse of the RFP, [58].

Appendix A

Proofs of theorems

A.1 Woltjer's theorems

First Woltjer's theorem. *If a magneto-fluid has zero resistivity ($\eta = 0$), then helicity $\mathcal{H}$ is conserved in time:*

$$\frac{d\mathcal{H}}{dt} = 0. \tag{A.1}$$

Proof. The proof of this theorem simply consists in the evaluation of the rate of change in time of the helicity:

$$\frac{d\mathcal{H}}{dt} = \int \frac{\partial}{\partial t} (\mathbf{A} \cdot \mathbf{B})\, dV = \int \frac{\partial \mathbf{A}}{\partial t} \cdot \mathbf{B} dV + \int \mathbf{A} \cdot \frac{\partial \mathbf{B}}{\partial t} dV. \tag{A.2}$$

In case of zero resistivity the diffusive term in the induction equation is absent and this determines the time variation of $\mathbf{B}$ and considering that $\mathbf{B} = \nabla \times \mathbf{A}$ also the time variation of the vector potential $\mathbf{A}$ is determined:

$$\frac{\partial \mathbf{B}}{\partial t} = \nabla \times (\mathbf{v} \times \mathbf{B}), \qquad \frac{\partial \mathbf{A}}{\partial t} = \mathbf{v} \times \mathbf{B}. \tag{A.3}$$

Replacing equations (A.3) in equation (A.2), a null term is obtained because $(\mathbf{v} \times \mathbf{B}) \cdot \mathbf{B} = 0$, while the remaining term can be evaluated by means of the following vector identity $\nabla \cdot (\mathbf{V} \times \mathbf{W}) = \mathbf{W} \cdot (\nabla \times \mathbf{V}) - \mathbf{V} \cdot (\nabla \times \mathbf{W})$ (that holds for any couple of vectors), obtaining:

$$\frac{d\mathcal{H}}{dt} = \int \mathbf{A} \cdot \nabla \times (\mathbf{v} \times \mathbf{B})\, dV = \int \nabla \cdot [(\mathbf{v} \times \mathbf{B}) \times \mathbf{A}]\, dV + \int (\mathbf{v} \times \mathbf{B}) \cdot (\nabla \times \mathbf{A})\, dV. \tag{A.4}$$

In equation (A.4) the second term in the sum is zero, while the first can be evaluated using the Gauss theorem:

$$\frac{d\mathcal{H}}{dt} = \oint_{\partial V} [(\mathbf{v} \times \mathbf{B}) \times \mathbf{A}] \cdot d\mathbf{S}, \tag{A.5}$$

Here ∂V represents the surface of the magneto-fluid system and $d\mathbf{S}$ is a vector element perpendicular to the surface differential element dS. Since $\mathbf{v}$ and $\mathbf{B}$ are parallel to the boundary of the magneto-fluid, the whole integrand has zero component perpendicular to the surface and so the total integral contribution is zero, thus proving the theorem. □

Second Woltjer's theorem. *In a system in which the magnetic helicity $\mathcal{H}$ is kept constant, the minimization of the magnetic energy $W = \int B^2/2\mu_0 dV$ is obtained for a force-free field defined by the condition:*

$$\nabla \times \boldsymbol{B} = \mu \boldsymbol{B}, \tag{A.6}$$

with $\mu = constant$.

Proof. To find the minimum of the magnetic energy in presence of constant helicity constraint the Lagrange multipliers method is applied. It consists in solving the following equation:

$$\delta W - \frac{\mu}{2\mu_0}\delta\mathcal{H} = 0, \tag{A.7}$$

where the constant $\mu/2\mu_0$ is chosen as Lagrange multiplier. Replacing the definitions of magnetic and helicity one can get:

$$\delta W - \frac{\mu}{2\mu_0}\delta\mathcal{H} = \int \left(\frac{\mathbf{B}\cdot\delta\mathbf{B}}{\mu_0} - \mu\frac{\delta\mathbf{A}\cdot\mathbf{B}}{2\mu_0} - \mu\frac{\mathbf{A}\cdot\delta\mathbf{B}}{2\mu_0} \right) dV. \tag{A.8}$$

The last term in the sum in (A.8) can be rewritten, remembering that $\delta\mathbf{B} = \nabla\times\delta\mathbf{A}$, and making use of the vector identity $\nabla\cdot(\mathbf{V}\times\mathbf{W}) = \mathbf{W}\cdot(\nabla\times\mathbf{V}) - \mathbf{V}\cdot(\nabla\times\mathbf{W})$ that has already been met:

$$\int \frac{\mathbf{A}\cdot\delta\mathbf{B}}{2\mu_0}dV = \int \frac{\mathbf{A}\cdot(\nabla\times\delta\mathbf{A})}{2\mu_0}dV = \int \left[\frac{\nabla\cdot(\delta\mathbf{A}\times\mathbf{A})}{2\mu_0} + \frac{\delta\mathbf{A}\cdot(\nabla\times\mathbf{A})}{2\mu_0} \right] dV. \tag{A.9}$$

The first term in the sum is evaluated by means of the Gauss theorem as surface integral on the magneto-fluid boundary, where variations are expected to be exactly zero. Therefore, the only surviving term is the second:

$$\int \frac{\mathbf{A}\cdot\delta\mathbf{B}}{2\mu_0}dV = \int \frac{\delta\mathbf{A}\cdot\mathbf{B}}{2\mu_0}dV. \tag{A.10}$$

Replacing the previous result in (A.8) the proof is obtained. In fact:

$$0 = \delta W - \frac{\mu}{2\mu_0}\delta\mathcal{H} = \int \frac{B}{2\mu_0}\left(\delta\mathbf{B} - \mu\delta\mathbf{A}\right) dV \quad \Longleftrightarrow \quad \mathbf{B} = \mu\mathbf{A}. \tag{A.11}$$

After taking the curl on both sides, (A.11) exactly becomes: $\nabla\times\mathbf{B} = \mu\mathbf{B}$, the condition that defines force free fields. □

A.2 MHD visco-resistive equations in Fourier space

The aim of this section is to explain how the differential equations of the magnetohydrodynamics are commuted passing to the Fourier space. The entire section is performed in cylindrical geometry with periodic boundary conditions.

Linearity in the real space. A linear differential equation is transformed, in the Fourier space, in an algebraic equation that involves relationship only between the same Fourier mode.

This can be evident analyzing, as example, the Ampère-Maxwell that in the last form is reduced to:

$$\nabla \times \mathbf{B} = \mathbf{j}. \tag{A.12}$$

In the Fourier space, the fields $\mathbf{B}$ and $\mathbf{j}$ are rewritten as:

$$\mathbf{B}(r,\theta,z,t) = \sum_{m=-N_\theta}^{+N_\theta} \sum_{n=-N_z}^{+N_z} \mathbf{B}_{m,n}(r,t)\, e^{i\left(m\theta + \frac{n}{R_0}z\right)}, \tag{A.13}$$

$$\mathbf{J}(r,\theta,z,t) = \sum_{m'=-N_\theta}^{+N_\theta} \sum_{n'=-N_z}^{+N_z} \mathbf{J}_{m',n'}(r,t)\, e^{i\left(m'\theta + \frac{n'}{R_0}z\right)}. \tag{A.14}$$

Using the well known expression for the curl in cylindrical coordinates and calculating the derivatives an equation about the modes is obtained since the exponential function is not altered by the derivations, unless the addition of multiplicative constants:

$$\mathbf{j}_{m,n}(r,t) = \begin{pmatrix} \frac{im}{r} B^\theta_{m,n}(r,t) - \frac{inz}{R_0} B^z_{m,n}(r,t) \\ \frac{inz}{R_0} B^r_{m,n}(r,t) - \frac{\partial}{\partial r} B^z_{m,n}(r,t) \\ \frac{B^\theta_{m,n}(r,t)}{r} + \frac{\partial B^\theta_{m,n}(r,t)}{\partial r} - \frac{im}{r} B^r_{m,n}(r,t) \end{pmatrix}. \tag{A.15}$$

Non linearity in the real space. A non linear differential equation is transformed, in the Fourier space, in an algebraic equations that involves relationship only between different Fourier modes.

To exemplify this concept it's enough to evaluate a typical term of the MHD equations: $\mathbf{j} \times \mathbf{B}$. Since $\mathbf{j} \times \mathbf{B} = (\nabla \times \mathbf{B}) \times \mathbf{B}$, the calculation can be carried out in cylindrical coordinates:

$$\mathbf{j} \times \mathbf{B} = \begin{pmatrix} B_z j_\theta - B_\theta j_z \\ B_r j_z - j_r B_z \\ B_\theta j_r - B_r j_{\theta.} \end{pmatrix} \tag{A.16}$$

If the previous result for j is replaced, interaction terms between different modes arise as it can be seen calculating, for example, the radial component:

$$\begin{aligned} (\mathbf{j} \times \mathbf{B})_r = &\sum_{m,n} \sum_{m',n'} B^z_{m,n}(r,t) \left(\frac{in'z}{R_0} B^r_{m',n'}(r,t) - \frac{\partial B^z_{m',n'}(r,t)}{\partial r} \right) e^{i\left(m\theta + \frac{n}{R_0}z\right)} e^{i\left(m'\theta + \frac{n'}{R_0}z\right)} + \\ - &\sum_{m,n} \sum_{m',n'} B^\theta_{m,n}(r,t) \left(\frac{B^\theta_{m',n'}(r,t)}{r} + \frac{\partial B^\theta_{m',n'}(r,t)}{\partial r} - \frac{im'}{r} B^r_{m',n'}(r,t) \right) e^{i\left(m\theta + \frac{n}{R_0}z\right)} e^{i\left(m'\theta + \frac{n'}{R_0}z\right)}. \end{aligned} \tag{A.17}$$

Fourier series of the product of two physical quantities in the real space. The Fourier mode of the product of two physical quantities can be written as convolution of different modes in the real space. In formulas:

$$\left[B^i B^j(r,t)\right]_{\tilde{m},\tilde{n}} = \sum_{m,n} B^i_{m,n}(r,t) \left(B^j_{m-\tilde{m},n-\tilde{n}}(r,t) \right)^* e^{i\left(\tilde{m}\theta + \frac{\tilde{n}}{R_0}z\right)}, \tag{A.18}$$

where i, j are two general dimensions in cylindrical coordinates and the magnetic field is chosen, without loss of generality.

Proof. Rewriting the product of magnetic field in Fourier series:

$$B^i B^j = \sum_{m,n} \sum_{m',n'} B^i_{m,n}(r,t) B^j_{m',n'}(r,t) e^{i(m+m')\theta} e^{i\frac{n+n'}{R_0}z}. \tag{A.19}$$

To prove the thesis the following identities about the Kronecker δ are used:

$$e^{i(m+m')\theta} = \sum_{\tilde{m}} e^{i\tilde{m}\theta} \delta_{\tilde{m},m+m'}, \qquad e^{i\frac{n+n'}{R_0}z} = \sum_{\tilde{n}} e^{i\frac{\tilde{n}}{R_0}z} \delta_{\tilde{n},n+n'}, \tag{A.20}$$

that, once replaced in (A.19), gives the following equation obtained using the Kronecker δ properties:

$$B^i B^j = \sum_{\tilde{m},\tilde{n}} \left[\sum_{m,n} B^i_{m,n}(r,t) B^j_{\tilde{m}-m,\tilde{n}-n'}(r,t) e^{i\tilde{m}\theta} e^{i\frac{\tilde{n}}{R_0}z} \right] e^{i\left(\tilde{m}\theta + \frac{\tilde{n}}{R_0}z\right)}. \tag{A.21}$$

Subsequently, using the condition for reality $B_{-m,-n} = B^*_{m,n}$, to match the definition of the Fourier series one can get the thesis:

$$\left[B^i B^j\,(r,t)\right]_{\tilde{m},\tilde{n}} = \sum_{m,n} B^i_{m,n}(r,t) \left(B^j_{m-\tilde{m},n-\tilde{n}}(r,t)\right)^* e^{i\left(\tilde{m}\theta + \frac{\tilde{n}}{R_0}z\right)}. \tag{A.22}$$

□

Bibliography

[1] M. Agostini, R. Cavazzana, P. Scarin, G. Serianni (2006) *Operation of the gas-puff imaging diagnostic in the RFX-mod device*, Rev. Sci. Instrum., 77 (10), 10E513. Papers from the 16th Topical Conference on High Temperature Plasma Diagnostics.

[2] R. Albanese, on behalf of the WPDTT2 Team, and the DTT Project Proposal Contributors (2017), *Dtt: a divertor tokamak test facility for the study of the power exhaust issues in view of demo*, Nuclear Fusion, 57, 016010.

[3] A. Alfier and R. Pasqualotto (2007), *New thomson scattering diagnostic on rfx-mod*, Review of Scientific Instruments, 78, 013505.

[4] R. Balescu (1988), *Transport processes in plasmas*, North Holland, Amsterdam.

[5] I.B. Bernstein, E.A. Frieman, M.D. Kruskal, R.M. Kulsrud, 1958. *An energy principle for hydromagnetic stability problems*, Proceedings of the Royal Society of London. Series A. Mathematical and Physical Sciences, 244 (1236) 17-40.

[6] H.A.B. Bodin (1988), *Evolution of the RFP*, Plasma Physics and Controlled Fusion, Vol. 30, p. 2021.

[7] D. Bonfiglio, L. Chacón, S. Cappello (2010), *Nonlinear three-dimensional verification of the SPECYL and PIXIE3D magnetohydrodynamics codes for fusion plasmas*, 17, 082501.

[8] D. Bonfiglio, M. Veranda, S. Cappello, D. F. Escande, L. Chacón (2013), *Experimental-like Helical Self-Organization in Reversed-Field Pinch Modeling*, Physical Review Letters, 111, 085002.

[9] S.I. Braginskii (1965), *Transport Processes in a Plasma*, Reviews of Plasma Physics, Vol.1 , p.205, New York.

[10] S. Cappello, D. Biskamp (1996), *Reconnection processes and scaling laws in reversed field pinch magnetohydrodynamics*, Nuclear Fusion, Vol. 36, n. 5.

[11] S. Cappello, D. Bonfiglio, D.F. Escande, S.C. Guo, A. Alfier, R. Lorenzini and RFX Team (2008), *The Reversed Field Pinch toward magnetic order: a genuine self-organization*, Varenna-Lausanne Theory of Fusion Plasmas, AIP Conf. Proc. 1069, 27.

[12] S. Cappello, D.F. Escande (2000), *Bifurcation in Viscoresistive MHD: The Hartmann and the Reversed Field Pinch*, Physical Review Letters Vol. 85, p. 3838.

[13] A. Carati, M. Zuin, A. Maiocchi, M. Marino, E. Martines, L. Galgani (2012), *Transition from order to chaos, and density limit, in magnetized plasmas*, Chaos: An Interdisciplinary Journal of Nonlinear Science, 22, 033124.

[14] L. Carraro, P. Innocente, M.E. Puiatti, F. Sattin, P. Scarin, M. Valisa (1995), *Effects of the impurities on the loop voltage in rfx*, in B.E. Keen, P.E. Stott, J.Winter, editors Proc. of the 22$^{\text{nd}}$ EPS Conference on Plasma Physics, volume 19C, p. 161-164, European Physical Society.

[15] Peter J. Catto (2019), *Practical gyrokinetics*, Journal of Plasma Physics, 85, 925850301.

[16] B.E. Chapman, A.F. Almagri, J.K. Anderson, D.L. Brower, K.J. Caspary, D.J. Clayton, D. Craig, D.J. Den Hartog, W.X. Ding, D.A. Ennis, G. Fiksel, S. Gangadhara, S. Kumar, R.M. Magee, R. O'Connell, E. Parke, S.C. Prager, J.A. Reusch, J.S. Sarff, H.D. Stephens, Y. M. Yang (2010), *Generation and confinement of hot ions and electrons in a reversed-field pinch plasma*, Plasma Physics and Controlled Fusion, 52, 124048.

[17] S. Chapmann, T.G. Cowling, *The Mathematical Theory of Non-Uniform Gases*, Cambridge University Press, Cambridge.

[18] A.R. Choudhuri (2012), *The Physics of Fluids and Plasmas*, Cambridge University Press.

[19] R.N. Dexter, D.W. Kerst, T.W. Lovell, S.C. Prager, J.C. Sprott. (1991), *The madison symmetric torus*, Fusion Technology, 19, p. 131-139.

[20] D. F. Escande, S. Cappello, F. D'Angelo, P. Martin, S. Ortolani and R. Paccagnella (2000), *Single helicity: a new paradigm for the reversed field pinch*, Plasma Physics and Controlled Fusion, 42, B243.

[21] R. Fitzpatrick (2014), *Plasma Physics: An Introduction*, CRC press.

[22] J. Freidberg (2007), *Plasma Physics and Fusion Energy*, Cambridge University Press, Cambridge.

[23] D. A. Gates, L. Delgado-Aparicio (2012), *Origin of tokamak density limit scalings*, Phys. Rev. Lett., 108, 165004.

[24] H. Goedbloed, S. Poedts (2004), *Principles of Magnetohydrodynamics*, Cambridge University Press, Cambridge.

[25] R.J. Goldston, P.H. Rutherford (1997), *Introduction to Plasma Physics*, IOP Publishing.

[26] M. Greenwald, J.L. Terry, S.M. Wolfe, S. Ejima, M.G. Bell, S.M. Kaye, G.H. Neilson (1988), *A new look at density limits in tokamaks*, Nuclear Fusion, Vol. 28, p. 2199.

[27] Y.L. Ho, D.D. Schnack, P. Nordlund, S. Mazur, H.-E. Satherblom, J. Scheffel, J. R. Drake (1995), *Effect of aspect ratio on magnetic field fluctuations in the reversed-field pinch*, Physics of Plasmas, 2, p. 3407-3411.

[28] P. Innocente, A. Alfier, A. Canton, R. Pasqualotto (2009), *Plasma performance and scaling laws in the RFX-mod reversed-field pinch experiment*, Nuclear Fusion, 49, 115022.

[29] P. Innocente, S. Martini, A. Canton, and L. Tasinato (1997), *Upgrade of the rfx co2 interferometer using in-vessel optics for extended edge resolution*, Review of Scientific Instruments, 68, p. 694-697.

[30] M. Keilhacker, A. Gibson, C. Gormezano, P.J. Lomas, P.R. Thomas, M.L Watkins, P. Andrew, B. Balet, D. Borba, C.D Challis, I Coffey, G.A Cottrell, H.P.L. De Esch, N. Deliyanakis, A. Fasoli, C.W. Gowers, H.Y. Guo, G.T.A. Huysmans, T.T.C. Jones, W. Kerner, R.W.T. König, M.J. Loughlin, A. Maas, F.B. Marcus, M.F.F. Nave, F.G. Rimini, G.J. Sadler, S.E. Sharapov, G. Sips, P. Smeulders, F.X. Söldner, A. Taroni, B.J.D. Tubbing, M.G. von Hellermann, D.J. Ward, and JET Team (1999), *High fusion performance from deuterium-tritium plasmas in JET*, Nuclear Fusion, 39, p. 209-234.

[31] M.Kikuchi, K.Lachner, M.Q. Tran (2012), *Fusion Physics*, I.A.E.A., Vienna.

[32] L.D. Landau (1937), *The transport equation in the case of Coulomb interaction*, J. Exp. Theor. Phys. USSR, 7, 203.

[33] W. Liu, W. Mao, T. Lan, G. Zhuang, J. Zheng, P. Yuan, H. Li, J. Xie, A. Liu, Z. Wu, Z. Liu, S. Wan, H. Wang, X. Wen, H. Zhou, Z. Wei, W. You, C. Tu, M. Tan, Z. Li, Y. Adil, H. Xu, T. Deng, J. Zhu, C. Chen, S. Zhang, J. Wu, Y. Zu, B. Luo, C. Xiao, W. Ding (2019), *An overview of diagnostic upgrade and experimental progress in the KTX*, Nuclear Fusion, 59, 112013.

[34] R. Lorenzini, M. Agostini, A. Alfier, V. Antoni, L. Apolloni, F. Auriemma, O. Barana, M. Baruzzo, P. Bettini, D. Bonfiglio, T. Bolzonella, F. Bonomo, M. Brombin, A. Buffa, A. Canton, S. Cappello, L. Carraro, R. Cavazzana, G. Chitarin, S. Dal Bello, A. De Lorenzi, G. De Masi, D. F. Escande, A. Fassina, P. Franz, E. Gaio, E. Gazza, L. Giudicotti, F. Gnesotto, M. Gobbin, L. Grando, S. C. Guo, P. Innocente, A. Luchetta, G. Manduchi, G. Marchiori, D. Marcuzzi, L. Marrelli, P. Martin, S. Martini, E. Martines, F. Milani, M. Moresco, L. Novello, S. Ortolani, R. Paccagnella, R. Pasqualotto, S. Peruzzo, R. Piovan, P. Piovesan, L. Piron, A. Pizzimenti, N. Pomaro, I. Predebon, M. E. Puiatti, G. Rostagni, F. Sattin, P. Scarin, G. Serianni, P. Sonato, E. Spada, A. Soppelsa, S. Spagnolo, G. Spizzo, M. Spolaore, C. Taliercio, D. Terranova, V. Toigo, M. Valisa, P. Veltri, N. Vianello, P. Zaccaria, B. Zaniol, L. Zanotto, E. Zilli, and M. Zuin (2009), *Improvement of the magnetic configuration in the reversed field pinch through successive bifurcations*, Physics of Plasmas 16, 056109.

[35] R. Lorenzini, E. Martines, P. Piovesan, D. Terranova, P. Zanca, M. Zuin, A. Alfier, D. Bonfiglio, F. Bonomo, A. Canton, S. Cappello, L. Carraro, R. Cavazzana, D.F. Escande, A. Fassina, P. Franz, M. Gobbin, P. Innocente, L. Marrelli, R. Pasqualotto, M.E. Puiatti, M. Spolaore, M. Valisa, N. Vianello, P. Martin, and RFX-mod team and collaborators (2009), *Self-organized helical equilibria as a new paradigm for ohmically heated fusion plasmas*, Nature Phys, 5, p. 570-574.

[36] L. Marrelli, R. Cavazzana, D. Bonfiglio, M. Gobbin, G. Marchiori, S. Peruzzo, M.E. Puiatti, G. Spizzo, D. Voltolina, P. Zanca, M. Zuin, G. Berton, P. Bettini, T. Bolzonella, A. Canton, S. Cappello, L. Carraro, L. Cordaro, S. Dal Bello, M. Dalla Palma, G. De Masi, A. Fassina, F. Gnesotto, L. Grando, P. Innocente, F. Lunardon, G. Manduchi, D. Marcuzzi, N. Marconato, R. Piovan, N. Pomaro, A. Rigoni, A. Rizzolo, P. Scarin, M. Siragusa, P. Sonato, S. Spagnolo, M. Spolaore, D. Terranova, and the RFX-mod team (2019), *Upgrades of the RFX-mod reversed field pinch and expected scenario improvements*, Nuclear Fusion, 59, 076027.

[37] Naval Research Laboratory (2018), *NRL Plasma Formulary*, U.S. Navy, Washington.

[38] S. Ortolani (1983), *Equilibrium and Stability Properties of Reversed Field Pinch Configurations*, In R. Pozzoli and E. Sindoni, editors, Proceedings of the International School of Plasma Physics, Course on Mirror-based and Field-reversed Approaches to Magnetic Fusion, Varenna, Italy, vol. 2, p. 513, Monotypia Franchi, Città di Castello.

[39] P. Piovesan, D. Bonfiglio, F. Auriemma, F. Bonomo, L. Carraro, R. Cavazzana, G. De Masi, A. Fassina, P. Franz, M. Gobbin, L. Marrelli, P. Martin, E. Martines, B. Momo, L. Piron, M. Valisa, M. Veranda, N. Vianello, B. Zaniol, M. Agostini, M. Baruzzo, T. Bolzonella, A. Canton, S. Cappello, L. Chacón, G. Ciaccio, D.F. Escande, P. Innocente, R. Lorenzini, R. Paccagnella, M.E. Puiatti, P. Scarin, A. Soppelsa, G. Spizzo, M. Spolaore, D. Terranova, P. Zanca, L. Zanotto, M. Zuin (2013), *Rfx-mod: A multi-configuration fusion facility for three-dimensional physics studiesa*, Physics of Plasmas (1994-present), 20, 056112.

[40] D.C. Robinson, R.E. King. (2012), *Factors influencing the period of improved stability in zeta*, Plasma Physics and Controlled Nuclear Fusion Research, vol. 1, p. 263, Vienna, IAEA.

[41] M.E. Puiatti, P. Scarin, G. Spizzo, M. Valisa, R. Paccagnella, I. Predebon, M. Agostini, A. Alfier, A. Canton, S. Cappello, L. Carraro, E. Gazza, P. Innocente, R. Lorenzini, L. Marrelli, D. Terranova (2009), *High density limit in reversed field pinches*, Physics of Plasmas, 16, 012505.

[42] M.E. Puiatti, G. Spizzo, M. Agostini, F. Auriemma, D. Bonfiglio, A. Canton, S. Cappello, L. Carraro, R. Cavazzana, G. Ciaccio (2013), *Interaction between magnetic boundary and first wall recycling in the reversed field pinch*, Plasma Physics and Controlled Fusion, 55, 124013.

[43] P. Scarin, M. Agostini, G. Spizzo, M. Veranda, P. Zanca, RFX-Mod Team (2019), *Helical plasma-wall interaction in the RFX-mod: effects of high-n mode locking*, Nuclear Fusion, 59, 8.

[44] P. Sonato, G. Chitarin, P. Zaccaria, F. Gnesotto, S. Ortolani, A. Buffa, M. Bagatin, W.R. Baker, S. Dal Bello, P. Fiorentin, L. Grando, G. Marchiori, D. Marcuzzi, A. Masiello, S. Peruzzo, N.

Pomaro, G. Serianni (2003), *Machine modification for active MHD control in RFX*, Fusion Engineering and Design, 66-68, 161-168.

[45] G. Spizzo, M. Agostini, P. Scarin, N. Vianello, R.B. White, S. Cappello, M.E. Puiatti, M. Valisa, and the RFX-mod Team (2012), *Edge topology and flows in the reversed-field pinch*, Nuclear Fusion, p. 52, 054015, 2012.

[46] G. Spizzo, G. Pucella, O. Tudisco, M. Zuin, M. Agostini, E. Alessi, F. Auriemma, W. Bin, P. Buratti, L. Carraro, R. Cavazzana, G. Ciaccio, G. De Masi, B. Esposito, C. Galperti, S. Garavaglia, G. Granucci, M. Marinucci, L. Marrelli, E. Martines, C. Mazzotta, D. Minelli, A. Moro, M.E. Puiatti, P. Scarin, C. Sozzi, M. Spolaore, O. Schmitz, N. Vianello, R.B. White (2015), *Density limit studies in the tokamak and the reversed-field pinch*, Nuclear Fusion 55, 043007.

[47] G. Spizzo, P. Scarin, M. Agostini, A. Alfier, F. Auriemma, D. Bonfiglio, S. Cappello, A. Fassina, P. Franz, L. Piron, P. Piovesan, M.E. Puiatti, M. Valisa, N. Vianello (2010), *Investigation on the relation between edge radial electric field asymmetries in RFX-mod and density limit*, Plasma Physics and Controlled Fusion, 52, 095011.

[48] A. Stella, M. Guarnieri, F. Bellina, P.P. Campostrini, G. Chitarin, F. Trevisan, P. Zaccaria (1995), *The RFX magnet system*, Fusion Engineering and Design, 25, p. 373 - 399.

[49] M.R. Stoneking, J.T. Chapman, D.J. Den Hartog, S.C. Prager, and J.S. Sarff (1998), *Experimental scaling of fluctuations and confinement with lundquist number in the reversed-field pinch*, 5, p. 1004-1014.

[50] W. Suttrop, K. Buchl, J.C. Fuchs, M. Kaufmann, K. Lackner, M. Maraschek, V. Mertens, R. Neu, M. Schittenhelm, M. Sokoll, and H. Zohm (1997), *Tearing mode formation and radiative edge cooling prior to density limit disruptions in asdex upgrade*, Nuclear Fusion, 37, 119.

[51] J. B. Taylor (1974), *Relaxation of Toroidal Plasma and Generation of Reverse Magnetic Fields*, Physical Review Letters, Vol. 33, p. 1139.

[52] D. Terranova, T. Bolzonella, S. Cappello, P. Innocente, L. Marrelli, R. Pasqualotto (2000), *Study of the scaling of magnetic fluctuations in the RFX reversed field pinch*, Plasma Physics and Controlled Fusion, 42, p. 843-854.

[53] M. Veranda, D. Bonfiglio, S. Cappello, D. F. Escande, F. Auriemma, D. Borgogno, L. Chacón, A. Fassina, P. Franz, M. Gobbin, D. Grasso, M. E. Puiatti (2017), *Magnetohydrodynamics modelling successfully predicts new helical states in reversed-field pinch fusion plasmas*, Nuclear Fusion, 57, 116029.

[54] J.A. Wesson, R.D. Gill, M. Hugon, F.C. Schüller, J.A. Snipes, D.J. Ward, D.V. Bartlett, D.J. Campbell, P.A. Duperrex, A.W. Edwards, R.S. Granetz, N.A.O. Gottardi, T.C. Hender, E. Lazzaro, P.J. Lomas, N. Lopes Cardozo, K.F. Mast, M.F.F. Nave, N.A. Salmon, P. Smeulders, P.R. Thomas, B.J.D. Tubbing, M.F. Turner, and A. Weller (1989), *Disruptions in jet*, Nuclear Fusion, 29, p. 641-666.

[55] J. Wesson (2011), *Tokamkas*, Oxford University Press, Oxford.

[56] R.B. White, D.A. Gates, and D.P. Brennan (2015), *Thermal island destabilization and the greenwald limit*, Physics of Plasmas (1994-present), 22, 022514.

[57] L. Woltjer (1958), *A theorem on force-free magnetic fields*, Proceedings of the NATIONAL ACADEMY OF SCIENCES, Vol. 44, p. 489, Chicago.

[58] P. Zanca, F. Sattin, D.F. Escande, G. Pucella, O. Tudisco (2017), *A unified model of density limit in fusion plasmas*, Nuclear Fusion, 57, 056010.

[59] P. Zanca, D. Terranova (2004), *Reconstruction of the magnetic perturbation in a toroidal reversed field pinch*, Plasma Physics and Controlled Fusion, 46, 1115.

[60] H. Zohm (2014), *Resistive MHD Stability*, p. 118, Wiley-VCH Verlag GmbH & Co. KGaA.